Collective Behavior at the Interface of Lithium-Ion Batteries under Cyclic Lithiation

By

Hsiao-Mei Wu

B. Sc., National Taiwan University, 2004

M. Sc., University of Illinois at Urbana-Champaign, 2006

M. Sc., Brown University, 2009

Thesis

Submitted in partial fulfillment of the requirements for the Degree of

Doctor of Philosophy in the School of Engineering at Brown University

PROVIDENCE, RHODE ISLAND

MAY 2014

This dissertation by Hsiao-Mei Wu is accepted in its present form

by the School of Engineering as satisfying the

dissertation requirement for the degree of Doctor of Philosophy.

Date _____   _____

Kyung-Suk Kim, Advisor

Recommended to the Graduate Council

Date _____   _____

Pradeep R. Guduru, Reader

Date _____   _____

Brian W. Sheldon, Reader

Approved by the Graduate Council

Date _____   _____

Peter M. Weber, Dean of the Graduate School

Curriculum Vitae

Hsiao-Mei Wu was born on December 27, 1981, at Taipei, Taiwan, Republic of China. She attended National Taiwan University in 2000 and got her B. Sc. degree in Civil Engineering in 2004. Later she completed her M. Sc. in Civil and Environmental Engineering at University of Illinois at Urbana-Champaign in December 2006. She entered the Mechanics of Solids program at Brown University in 2008 and was awarded an M. Sc. in 2009.

Publications

Wu, H.-M., Yi, J. W., Moon, M.-W., & Kim, K.-S. (2011). Nanobearings in Nature. Poster, *Future Directions in Mechanics Research, NSF Workshop and Symposium in honor of Professor L. B. Freund*.

Wu, H.-M., Tokranov, A., Xiao, X., Qi, Y., Verbrugge, M. W., Sheldon, B. W., & Kim, K.-S. (2014). Characterization of Interfacial Sliding Properties at Amorphous Si/Cu Interface due to Li-ion Intercalation by Using Self-Adjusting Liquid Linnik Interferometer. Extended Abstract, *17th U.S. National Congress on Theoretical and Applied Mechanics*.

Acknowledgments

I would like to express the deepest appreciation to my advisor Professor Kyung-Suk Kim, who inspired me the beauty of experiment, taught me the importance of uniqueness, and cultivated me the persistence of chasing principles. Without his guidance and continually help, this research work would not have been possible. I am grateful to Professor Pradeep Guduru and Professor Brain Sheldon for their insightful comments leading to significant improvement in the quality of this work. Thank all other faculty members and staffs at School of Engineering for providing me a robust and warm academic environment.

I would like to thank the research scientists at the General Motors R&D center, especially Dr. Yue Qi, Dr. Xingcheng Xiao, Dr. Mark Verbrugge, and Dr. Qian Lin for giving me the suggestions and materials to complete my studies. I am indebted to the funding support from General Motors through the GM/Brown collaborative research lab.

I also thank my fellow lab mates in Nano and Micromechanics Laboratory, Moon-Hyun Cha, Huck Beng Chew, Mazen Diab, Hyun-Gyu Kim, Sang-Pil Kim, Jahn Torres, Shuman Xia, Jin Woo Yi, Cheng Zhang, Ruike Zhao, and my fellow graduate students, Jay Sheth, Maria Stournara, Anton Tokranov, Ravi Kumar, Xin Yi, Teng Zhang, for their friendships and helpful assistances. Moreover, I thank to my friends in Brown Taiwanese Graduate Student Association who made my life at Brown enjoyable.

Last but not the least, I would like to express my gratitude to my parents, my brother, and my husband Dr. Chien-Kai Wang for always supporting and encouraging me.

Table of Contents

List of Tables

List of Figures

Chapter 1.

INTRODUCTION

This thesis presents experimental measurements and modeling of multi-scale collective behaviors characteristics of hierarchical interfaces in lithium-ion batteries (LIBs) during cycling. Two interfacial mechanisms are introduced: one is in-plane sliding between lithiated electrodes and current collectors; the other is normal contact between the internal interfaces of pouch battery cells. Through bridging *in situ* measurements and numerical models, the multi-scale collective behaviors of LIBs are elaborated. It is hoped that the work carried out in this thesis can contribute to optimal design of new battery cells and maximize cell capacity and life of LIBs. The following sections of this chapter will first review backgrounds of LIBs. Then, briefly introduce the mechanical issues and challenges of current battery technology. Finally, an outline of this thesis will be provided.

1.1   Background of the Li-Ion Battery

In modern society, more and more portable electronic devices are invented, so the demands for lighter and miniature energy sources increase. Since Li is the lightest metal

(the density is 0.53 g·cm^{-3}) with high positive standard reduction potential (-3.04 V relative to a standard hydrogen electrode), using Li metal as an electrode material has drawn first attention in advanced battery technology (Schalkwijk & Scrosati, 2002). The historical development of lithium metal batteries started in 1970s. Whittingham (1976) made the first lithium battery by using TiS$_2$ as the cathode material and Li metal as the anode electrode. It was widely used in military applications and common electronic devices due to its high capacity. However, the uneven dendritic Li growth on the surface of electrodes during charge-discharge (C-D) cycles was the main drawback of lithium batteries. This dendritic problem resulted in electrical shortage of batteries and further induced explosion hazards (Tarascon & Armand, 2001).

In the meanwhile, Steele & Armand (1973) proposed the concept of electrochemical intercalation and suggested insertion compounds as battery electrodes. The major improvement was made by Basu who developed the first lithium intercalated graphite electrode at Bell Labs in 1977. It was found that Li-ion can intercalate into and deintercalate from graphite rapidly and reversibly. Later in 1983, Thackeray *et al.* identified manganese spinel as a positive electrode with low-cost, good structural stability and electric conductivity. These two discoveries led to significant development of Li-ion batteries technology and provided a substitute to the lithium mental battery. Nowadays, LIBs are considered to be safer batteries than Li-metal cells, since Li presents in ionic state instead of metallic state and the dendrite problem no longer occurs. In 1991, Sony Corporation created the first commercial LIB cell by using graphite as the anode electrode and LiCoO$_2$ as the cathode material (Nagaura & Tozawa, 1990). Till now, LiCoO$_2$ is still used as a common cathode material in modern LIBs.

In summary, LIBs with high energy density ($225 - 400$ W·h·L^{-1}), long cycle life, low self-discharge rate, lightweight design (with specific energy $100 - 175$ W·h·kg^{-1}), no memory effect, and no pollution, have been widely used as power supplies for portable electronic devices (Tarascon & Armand, 2001). For several decades, the rapid development of LIB has ensured its dominance of the secondary battery market by replacing traditional lead-acid, nickel cadmium, and nickel-metal hydride batteries (Gomadam *et al.*, 2002). Moreover, in the near future, LIBs have been considered as potential energy sources for electric vehicles (EV) due to environmental pollution and energy shortage problem in the world (Wakihara, 2001). This concern has drawn more and more attentions to study both fundamentals and applications of lithium-ion rechargeable batteries. It can be predicted that LIBs will become the most promising and important chemical energy sources in the 21st century.

The basic components of a LIB cell are composed of a cathode and an anode separated by a separator. Both electrodes are soaked in an electrolyte solution containing dissociated salts, which allows ion transfer between them. Here, anode and cathode materials serve as hosts for lithium. While chemical reactions proceed at both electrodes, the materials are not consumed and ideally do not change their structures as lithium ions and electrons are exchanged. During discharge cycles, useful energy comes from electrons moving to lower electrical potential while maintaining charge neutrality (Tarascon & Armand, 2001). Typical electrode redox reactions in the battery are in the following,

Cathode oxidation (e.g., lithium cobalt oxide): $LiCoO_2 \leftrightarrow Li_{1-x}CoO_2 + xLi^+ + xe^-$

Anode reduction (e.g., graphite): $xLi^+ + xe^- + C_6 \leftrightarrow LiC_6$
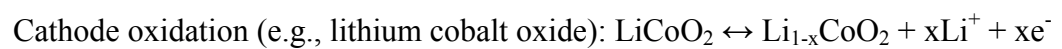
As an ideal cathode material, a lithium intercalation compound should react with lithium in a reversible manner (rapid insertion and removal) and with a high free energy of reaction to provide high capacity as well as high voltage. It also needs to be a good electron conductor and a stable material. In a practical point of view, the compound should be cheaper and will not induce environmental pollution. The common cathode materials are layered lithium cobalt oxide ($LiCoO_2$), layered lithium nickel manganese cobalt oxide ($LiNi_{1/3}Mn_{1/3}Co_{1/3}O_2$), spinel lithium manganese oxide ($LiMn_2O_4$), and olivine lithium iron phosphate ($LiFePO_4$). In general, layered compounds offer the highest energy density, followed by spinels (slightly less than layered) and olivines (approximately half) (Etacheri *et al.*, 2011; Whittingham, 2004).

With the development of LIBs technology, most studies have been focused on graphite, silicon-based, and tin-based materials as anodes. Recently, silicon-carbon composites and other alloys are also considered as potential candidates. Typically, the electrode redox potential of an ideal anode should be as low as possible to provide higher output voltage of a battery. The anode should react with lithium in a reversible manner (rapid insertion and removal) and provide higher capacity density due to more insertion ions. The change of its structure during lithium intercalation and deintercalation needs to be minimal to result in good cycle performance. Besides, the host material must have proper surface configuration for forming a passive layer to protect the electrode. Similar to cathode materials, an ideal anode has to have good conductivity and retain good chemical stability over the entire voltage range (Ji *et al.*, 2011). In a practical point of view, the material should be cheap and environmentally benign.

For more than two decades, most of commercial LIB cells have used graphite as an anode-active material. It serves as a reliable host structure for lithium to be easily intercalated and deintercalated. Recently, due to the development of EVs, more and more attentions have been drawn to improve the efficiency of large format pouch cells. The other rising interest is to enhance the performance of LIBs by using Si as an anode material. It is because Si has high theoretical capacity 4200 $mAg \cdot g^{-1}$ (more than ten times larger than that of graphite) and is the second most abundant element on earth (Kasavajjula et al., 2007). Therefore, the major efforts in this thesis are focused on the collective behaviors of anode materials, particularly emphasizing coated graphite (C) in commercial pouch cells and on nanostructured amorphous silicon (a-Si) anodes in half cells.

1.2   Mechanical Issues of the Li-Ion Battery

Although lithium-ion batteries are regarded as the best potential energy sources for electrical vehicles, there are still some remaining difficulties which need to be resolved. The major design considerations for LIBs involve electrochemistry, thermal management and mechanical integrity. The electrochemistry has been widely studied as it directly determines battery performance (e.g., cell potential, capacity, or energy density) and its life cycle (Etacheri et al., 2011; Lai et al., 2014; Wakihara, 2001). Several efforts have been devoted to predict battery performance as a function of its temperature, since battery efficiency strongly depends on its thermal response (Seong Kim et al., 2011). However, it is not the purpose of this thesis to review the enormous amount of previous research progresses in electrochemistry and thermal management. The main goal of this thesis is

to understand the collective behaviors of anode materials (especially graphite and a-Si electrodes) and further enhance the performance of LIBs via improving mechanical integrity.

For carbonaceous anode materials (graphite, hard carbon, hybrid carbon blends) and alloy anodes (i.e., Si, Sn, Sb, Al, Mg, and Bi) (W.-J. Zhang, 2011), the operation potential of negative electrodes is below the reduction potential of an electrolyte. Therefore, the electrolyte decomposes and reacts with the new surface of an anode to form a thin (several nanometer) film called solid-electrolyte interphase (SEI). The SEI layer is electrically resistive. It allows lithium-ion transports and behaves as a passivating film on the anode surface (Verma *et al.*, 2010). This formation process results in irreversible capacity loss and generates a certain amount of gases as by-products (depending on the compounds of the electrolyte) (Goers *et al.*, 2004; Kim *et al.*, 2011). Although SEI grows mostly during the first cycle, gases buildup on subsequent cycles due to formation of new SEI layers on freshly exposed anode owing to particle fracture. Evolution and migration of these gases could be critical to cell life especially for large format pouch cells used in EV, since they cause the cells tend to swell leading to highly inhomogeneous current distribution. This inhomogeneity can lead to various failure mechanisms such as local overcharging or lithium deposition (Arora *et al.*, 1999; Kostecki *et al.*, 2006). Another main concern for pouch cells is that electrode particles can easily lose contact (particles to particles, particles to current collectors), as there is no strong adhesive between layers of electrode/separator assembly. This electrical disconnection becomes more severe and brings in significant capacity fading and internal resistance increasing (Vetter *et al.*, 2005), while gas bubbles block Li-ion diffusion.

A few research groups have found that a cell under compressive stack pressure limited the porosity of the anode in the prismatic cell and enlarged the internal contact areas resulting in lower resistance and higher capacity (Rubino *et al.*, 2001). However, the influence of gases on porosity evolution in the electrodes leading to disintegration of the cells was not considered in these experiments, since the amount of gases accumulated in these tested cells was negligible unlike large format pouch cells for electrical vehicles.

The other major challenge for graphite and alloy anodes is large volume expansion and contraction during lithium insertion and extraction. This can cause serious capacity degradation of cells. For instance, the swelling and shrinking of anodes can lead to delamination of electrodes from current collectors, failure of binders, and movement of conductive carbon, all of which reduce connectivity of active materials and cause poor battery mechanical integrity finally resulting in loss of capacity (Vetter *et al.*, 2005). These lithiation and delithiation induced volume expansion and contraction are especially severe in Si anode system. Along with its ultrahigh theoretical capacity, 4200 mAh·g^{-1} (Boukamp *et al.*, 1981), Si electrodes expand up to nearly 400% of original volume (Beaulieu *et al.*, 2001) during lithiation. This large strain generates enormous stresses and leads to serious mechanical degradation, such as fracture of electrodes, pulverization of Si particles, and isolation of electrode particles from the adjacent materials (Kasavajjula *et al.*, 2007; Maranchi *et al.*, 2003; Xiao *et al.*, 2011). Many studies have been attempted to alleviate these stresses towards optimal design of Si electrodes through both structural and material optimization. However, the capacity fading due to fracture and delamination are still observed in different Si nanostructures, e.g., thin films (Bourderau *et al.*, 1999; Maranchi *et al.*, 2006), nanowires (Liu *et al.*, 2011; Ryu *et al.*, 2011), nanoparticles (Liu
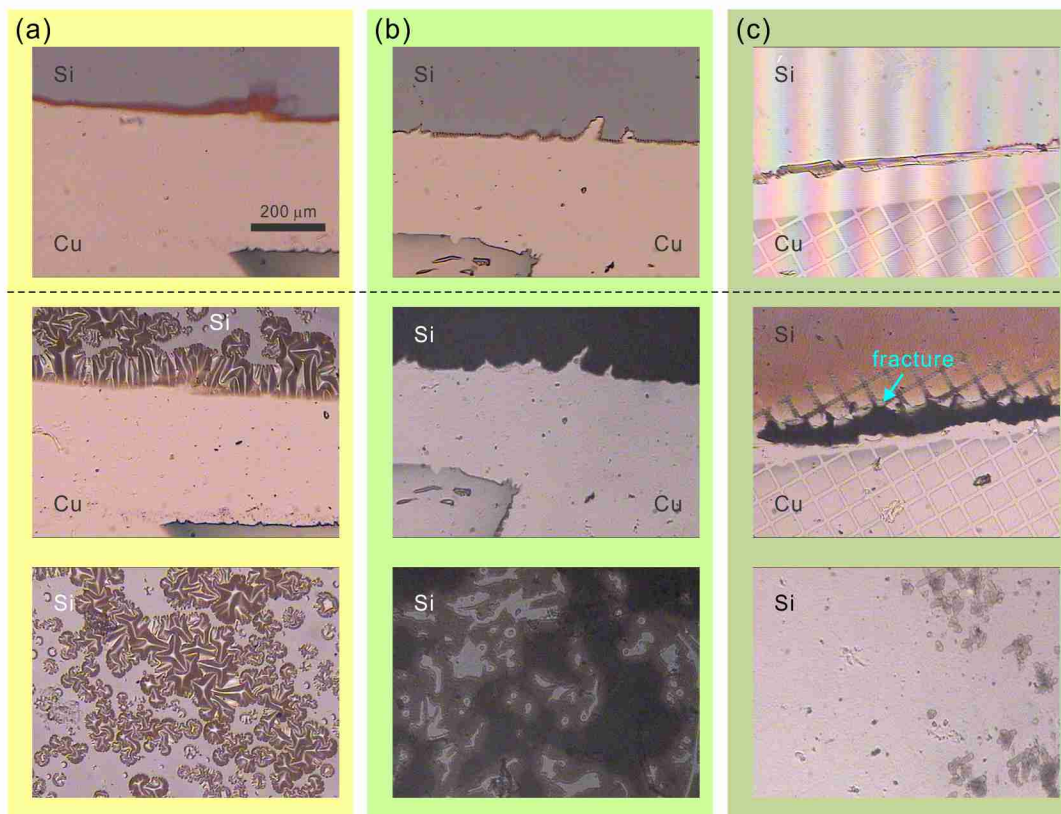
Figure 1.1 Micrographs of Si films on Cu substrate before (first row) and after (2nd and 3rd row) first cycle. The features near and away from the edge of Si films shown in 2nd and 3rd row respectively. (a) Uniaxial and biaxial delamination buckles near and away from the film edge respectively in a 89.1 nm thick Si film. Circular blister buckling shapes are observed at a region distant from the edge after cycling. (b) The notch at the edge became sharper and the film delamination happened at a region away from the edge of a 95.2 nm thick film. (c) Grid fracture patterns along the edge of a 108.7 nm film. Note that the grid patterns could be induced by the photoresist processes while making island markers.

et al., 2012; McDowell *et al.*, 2013), and Si-C composites (Guo *et al.*, 2005; L. Q. Zhang *et al.*, 2011).

Among these studies, an interesting thickness size effect has been reported for the a-Si thin film electrodes. It has been found that 50 nm a-Si thin film anodes on top of 30 μm thick Ni foils gave excellent electrochemical performance (over 3500 mAh·g^{-1}) for
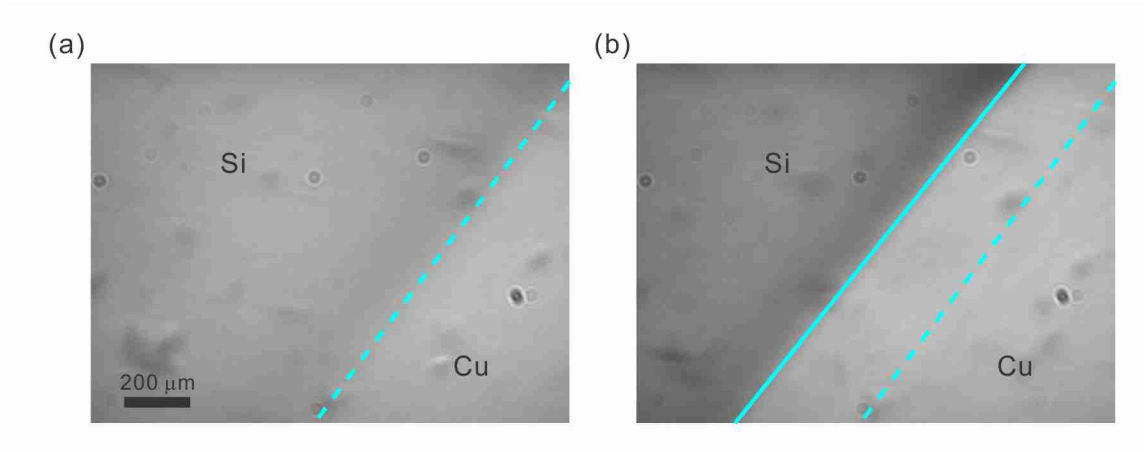
Figure 1.2 Plan-views of a 52.6 nm thin Si film on a Cu substrate (a) before and (b) after the first cycle. Note that the dotted line and solid line represent the edge of the film for initial and final configurations respectively. The figures show large-scale interfacial sliding of the film on the substrate and no fracture features observed after cycling.

200 cycles (Ohara *et al.*, 2004). On the other hand, thicker (300 nm) film had very poor available capacity (Takamura *et al.*, 2004). Moreover, a lot of microcracks have been observed from SEM morphology images of a 100 nm a-Si film on Cu after 12 cycles (Xiao *et al.*, 2011) and a 250 nm a-Si film even after first cycle (Maranchi *et al.*, 2006). Similar results were also observed in our experiments reported in this thesis. The micrographs of a-Si films with different thickness on Cu current collectors were obtained from optical microscope after first cycle. The development of telephone cord instability and circular blister buckling shapes (Argon *et al.*, 1989; Gille & Rau, 1984) were observed on the edge and at the bulk of a 89.1 nm Si film (Figure 1.1(a)). A 95.2 nm thin film delaiminated at the regions far from the edge and the notch at the edge became sharper indicating the film was still under compression (Figure 1.1(b)). For a thicker film (108.7 nm), fracture patterns at the regions far from and near the edge of the Si film were shown in Figure 1.1(c). However, no fracture or buckling features of a 52.6 nm thin film

9

was found after first cycle (Figure 1.2) due to the presence of interfacial sliding between the Si electrode and the Cu current collector.

Recently, the experiments and theoretical studies by Soni *et al.* (2011) and Haftbaradaran & Gao (2012) demonstrated that these large stresses can be mitigated due to interfacial sliding between electrodes and nearby current collectors. Although these results indicate that Si films with appropriate size can effectively prevent formation of microcracks and films delamination, the material properties (i.e., interfacial shear strength, energy release rate) at electrode/current collector interfaces during cyclic intercalation are still waiting to be determined.

1.3   Outline of Present Work

This thesis presents the experimental observations and simulation models of multi-scale collective behaviors of lithium-ion batteries (LIBs) caused by deformation characteristics of hierarchical interfaces during cycling. This work particularly focuses on the sliding mechanism between anodes (a-Si) and copper current collectors (Cu) and the contact mechanism between internal interfaces of large format pouch cells.

As mentioned in the previous section, although the interfacial properties during lithiation and delithiation cycles have been estimated from DFT calculations (Stournara *et al.*, 2013) and a continuum model (Haftbaradaran *et al.*, 2012), direct experimental measurements are still needed to validate the results. Therefore, an experiment for measuring the interfacial properties between a-Si thin film electrodes and Cu current collector is introduced in Chapter 2. Here, a new apparatus, called "self-adjusting liquid Linnik interferometer (SALLI)", is invented. SALLI overcomes existing limitations of

current interference microscopes with a novel optical configuration that naturally self-compensates for any refractive-index change in the liquid medium. Through direct imaging of the specimen, the lateral deformation can be monitored *in situ* with few micrometers resolution. At the same time, SALLI also permits high precision real-time measurements of thickness variation (resolution of 1 nm). This time-dependent full-field deformation measurement provides critical information about the Li distribution in the Si, and the corresponding deformation. In Chapter 3, a mechanical model system named as "plate bending distribution sensor (PBDS)" which incorporates substrate bending and interfacial sliding in its calibration, is developed to further extract the sliding characteristics of the interface between a film and a substrate from the SALLI experimental data. By bridging the deformation estimated from the model and those measured from SALLI experiment, the interfacial properties between the electrode film and current collector can be extracted quantitatively.

In Chapter 4, we perform two sets of *in situ* experimental tests and develop a mechanical model to explain the internal contact mechanism and its relationship with gas evolution. Through these experiments and the model, the performance of large format pouch cells under different prestressed pressures are elaborated. Non-uniform thickness variations across the whole surface area of a traction-free LG battery is first measured *in situ* during charge and discharge (C-D) cycles via employing an electronic speckle pattern interferometry (ESPI). Second, *in situ* confinement-pressure variations across the whole surface area of constrained battery cells are performed using a high resolution amplified pressure distribution sensor (APDS). These measurements are particularly useful for characterizing the cyclic performance of battery cells, understanding of which

must be bridged to that of microstructural behavior to improve structural design of battery packing.

Finally, the conclusions of the thesis and some comments for the future study on the interfacial behaviors of LIBs are included in Chapter 5.

Chapter 2.

IN SITU OPTICAL MEASUREMENT OF DISPLACEMENT FIELDS OF SI THIN FILM ANODE USING SELF-ADJUSTING LIQUID LINNIK INTERFEROMETER (SALLI)

2.1　Introduction

Rechargeable lithium-ion batteries (LIBs) are used as the most promising power supply of portable devices due to their superior energy density. The demand of LIBs is increasing due to the miniaturization of electronic appliances and the desire to enhance stretchability and flexibility of electronic devices (Bruce *et al.*, 2008; Schalkwijk & Scrosati, 2002; Xu *et al.*, 2013). Recently, LIBs are considered to be the energy sources for electrical vehicles. However, there are still some remaining difficulties which need to be resolved, e.g., electrode failure induced by large volume expansion during cycling and capacity degradation caused by SEI formation. Therefore, a large variety of *in situ* techniques have been used for studying electrode deformation and SEI growth ranging from spectroscopy to X-ray diffractometry and nanometer-scale microscopy (Verma *et al.*, 2010). For examples, vibration spectroscopes like Fourier transform infrared spectroscopy (FTIR) (Aurbach *et al.*, 1996) and Raman spectroscopy (Novák *et al.*, 2000) provide valuable surface information regarding the functionality. Synchrotron X-Ray

diffraction (XRD) (Poizot *et al.*, 2000) and synchrotron X-ray absorption spectroscopy (XAS) (Balasubramanian *et al.*, 2001) give crystal structure information and electronic structure charges respectively. Besides, a fundamental understanding of the morphologies of electrode materials observed from *in situ* microscopes, e.g., scanning electron microscopy (SEM) (Orsini *et al.*, 1998), transmission electron microscope (TEM) (Huang *et al.*, 2010), and atomic force microscope (AFM) (Aurbach & Cohen, 1996), is also important to mitigate the mechanical failure during cycling.

In situ SEM and TEM can provide useful information on morphological evolution in nm resolution, e.g. micro-cracking of particles (Chen *et al.*, 2011) and the evolution of the phase boundaries of electrodes (J. W. Wang *et al.*, 2013). But both of them have to be operated in ultra-high vacuum, and specially designed cells need to be implemented, i.e., only ionic liquid or solid electrolytes (Li_2O) can be used as electrolytes. Therefore, complicated sample preparation is required. Moreover, ionic liquid electrolytes (ILE) are highly sensitive to the electron beam (e-beam). It was observed that strong e-beam dose induced degradation of the ILE (Liu & Huang, 2011). This is a challenging issue especially in employing *in situ* TEM measurement that requires longer exposure time. Overall, the fields of view of both microscopes are small when we observe the morphological evolution with nm resolution, and both techniques can only provide local nanometrology information instead of the whole deformation fields.

In situ AFM techniques have also been used to monitor nanometrology in Li-ion battery cells (BalkeN *et al.*, 2010; Becker *et al.*, 2013). Although AFM can provide the whole out-of-plane deformation fields within a 100 μm observing window, this technique still has a few difficulties. Because the probes have to be immersed in liquid electrolytes

14

during scanning, the diffusion to electrode surface may be influenced by the geometry of AFM probes (Burt *et al.*, 2008) and SEI formation on the tip creates significant challenges with the measurements (Sri Devi Kumari *et al.*, 2013). Also, the scanning rate is the other key issue for this technique. At the slow scan rates needed for high resolution, there will be substantial deformation of the material between the first and last line-scans. Increasing the scan rate to capture these changes will limit resolution. Furthermore, soft materials (i.e., SEI) may be scratched by the tip (Domi *et al.*, 2011; Jeong *et al.*, 2001).

To observe the sliding phenomena of a thin film electrode (Figure 1.2), it requires an apparatus that has hundreds of micrometers field of view and nanometer resolution in the out-of-plane direction. Thus nondestructive real-time measurements with optical interference microscopes are ideally suited for *in situ* study of Li-ion battery materials. However, existing optical microscope interferometers have serious limitations for measuring objects in liquid media directly, largely because of mismatch between optical (phase) path length and image path length in the system. In this chapter, we present the development of a new apparatus, named "self-adjusting liquid Linnik interferometer (SALLI)". SALLI overcomes these difficulties with a novel optical configuration that naturally self-compensates for any refractive-index change in the liquid medium and provides real-time whole field deformation measurement which is essential information for better understanding the morphologies of LIBs during cycling.

2.2 Introduction to Interference Microscopes

In nanometrology, an optical interferometry is a main tool for observing minute details of the surface structure. Especially, a scanning white-light interferometer (SWLI), a variation of Michelson interferometer, can perform non-contact measurement of surfaces topography or displacements with nanometer resolution within a fraction of a second. It is a suitable technique for *in situ* measurement of thin film electrode deformation. In this section, the principle of Michelson interferometer is introduced first and three common types of SWLIs are briefly summarized. Finally, the limitations, i.e., the difficulties of measurements in liquid media, with existing SWLIs are elaborated.

2.2.1 *The principle of Michelson interferometer*

Michelson interferometer was invented by Albert A. Michelson in 1887 (Michelson & Morley, 1887). The setup configuration for Michelson interferometer is shown in Figure 2.1(a). The main optical parts consist of two plane mirrors **M1** and **M2** and one beam splitter **BS**. Light from an extended source **S** is divided by **BS** into two beams at right angles. These are reflected at **M1**, **M2**, and return to **BS**, where they are re-combined to enter the observing screen. In this setup, **M1** is mounted on a translation stage which can move it toward or away from **BS**. Once the two light waves are united, interference pattern can be observed.

A general equation for interference between two superimposed waves with the same frequency, but each with arbitrary amplitude and phase gives

$$E_T = E_1\, e^{i\,(\phi_1 - \omega t)} + E_2\, e^{i\,(\phi_2 - \omega t)}. \tag{2.1}$$
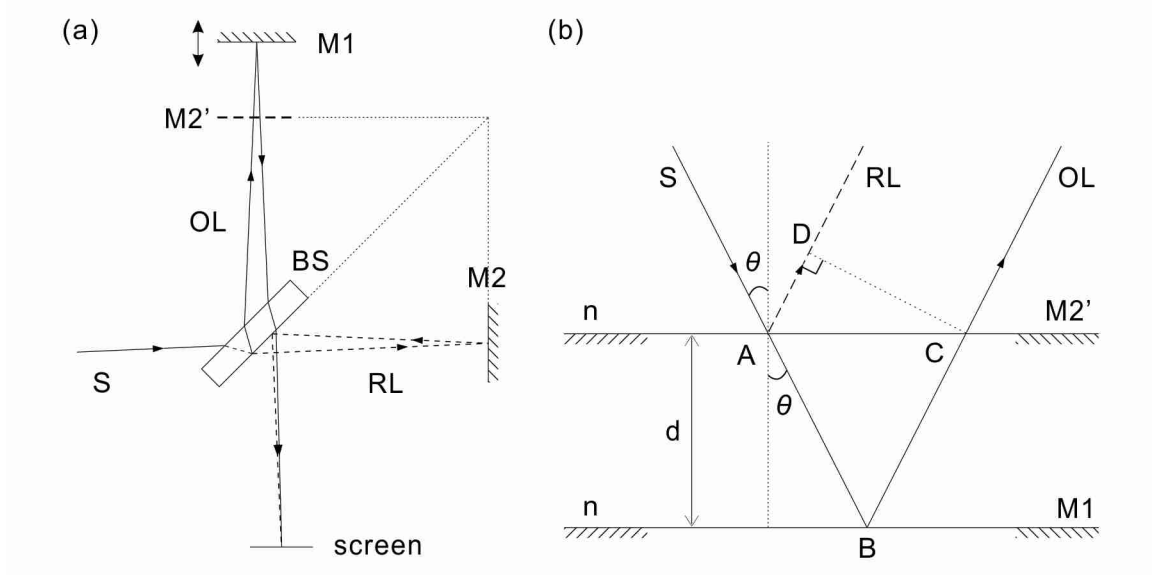
Figure 2.1 (a) A schematic of a basic Michelson interferometer. **M2'** – the image of **M2** in the beam splitter. The interference is considered as superposition of the real reflecting surface **M1** and the virtual reflecting surface **M2'**. (b) Plane parallel mirrors: illustrating the distance between two mirrors, **M1** and **M2'** (**M2**) in Michelson interferometer.

Note that E_1 and E_2 are the magnitudes of their respective fields, ϕ the phase, ω the angular frequency, and t time. The intensity of the superposed wave is

$$
\begin{aligned}
I \propto \left\langle E_T^* E_T \right\rangle &= E_1^2 + E_2^2 + 2E_1 E_2 \cos\left(\phi_1 - \phi_2\right) \\
&= I_1 + I_2 + 2\sqrt{I_1 I_2} \cos\left(\phi_1 - \phi_2\right),
\end{aligned}
\tag{2.2}
$$

where $\langle \cdot \rangle$ indicates time averaging and I_1, I_2 are the intensities of the individual fields. Here, we assume $I_1 = I_2$, as we use a 50:50 beam splitter. Then, the intensity can be derived as

$$
I = 2I_1 \left(1 + \cos\delta\right) = 4I_1 \cos^2 \frac{\delta}{2}.
\tag{2.3}
$$

If $\delta = \phi_1 - \phi_2 = 2m\pi$ where $m = \{0, 1, 2, ...\}$, then the waves are in phase. It is called constructive interference with maximum intensity $I = 4I_1$. Likewise, if $\delta = (2m+1)\pi$, then the two waves are out of phase. The intensity of this destructive interference has minimum intensity ($I = 0$).

In the Michelson interferometer, optical path difference (OPD) between the two superimposed waves, reference light (RL) and the objective light (OL), is illustrated in Figure 2.1(b) and estimated as

$$OPD = n\left(\overline{AB} + \overline{BC}\right) - n\overline{AD} = 2nd\cos\theta, \tag{2.4}$$

where n is refractive index of the medium, d is the distance between **M1** and **M2**, and θ is the angle of incidence which approaches to $0°$ in the setup. The relative phase difference according to this OPD is $\delta' = (2nd) \cdot 2\pi/\lambda$, where λ is the wavelength of the light source. While the two light waves with the same frequency and amplitude are in phase, the constructive fringes are observed. Then, the phase difference $\delta' = 2m\pi$, and it yields

$$d = \frac{m\lambda}{2n}. \tag{2.5}$$

Finally, the distance d between **M1** and **M2** in the medium with refractive index n can be measured by counting m numbers of fringes.

2.2.2 *Summary of scanning white-light interferometers (SWLIs)*

Following three types of SWLIs, i.e., Michelson, Mirau, and Linnik imaging interferometers illustrated in Figure 2.2, are variations of the basic Michelson interferometer in principle. Here, an object **O** replaces the mirror **M1** in Figure 2.1(a).

18
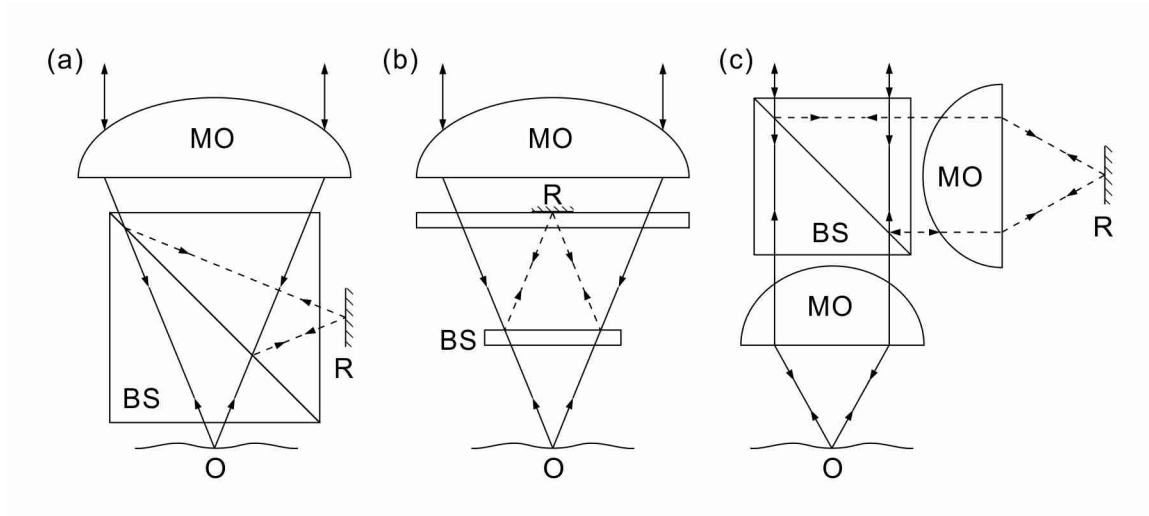
Figure 2.2 Schematics of three different types of SWLIs: (a) Michelson interferometer (b) Mirau interferometer (c) Linnik interferometer. Parts of the interferometers: **MO** – microscopic objective lens, **BS** – beam splitter, **O** – object, **R** – reference mirror.

Then, the measuring quantity d in equation (2.5) represents the relative distance from the detector to the object **O** and the reference mirror **R** (original **M2** in Figure 2.1(a)). In any case, the accuracy of length or wavelength measurement depends on how accurate one can determine the fringe structure and position. Therefore, to obtain a high lateral resolution, microscope objectives are used. Besides, to minimize the optical paths in the interferometer arms, a miniaturized interferometer is generally assembled inside the microscope objective (Malacara, 2007).

The microscopic interferometer with Michelson setup (Figure 2.2(a)) is designed for the measurement of surfaces with large fields of views. The magnification used in this interferometer is rather low, from 1X to 5X. In this setup, a beam splitter **BS** is placed below the microscope objective lens **MO**. The reference mirror **R** is located outside the image path. Note that the working distance is limited by **BS**.

Mirau interferometer (Mirau, 1952), shown in Figure 2.2(b), uses intermediate magnifications 10X-50X and two parallel plane glass plates are placed in front of **MO**. Since this setup is most compact, most SWLIs are equipped with a Mirau objective. However, the disadvantage of Mirau interferometer is the small usable numerical aperture. Besides, the position of **R** may cause central obscuration during measurement (Lehmann, 2010).

Figure 2.2(c) is Linnik interferometer (Linnik, 1933) which is suitable for high magnifications (100X-200X) and gives high lateral resolution. In this setup, no components in front of **MO** are needed. Hence, it provides the longest working distance and highest numerical aperture. In order to achieve equal optical path lengths in both reference and object lights, both **MO**s are required to have identical wave fronts and chromatic aberrations. On the other hand, this type of SWLI is more sensitivity to mechanical noise and thermal vibration due to its longer working distance (Niehues *et al.*, 2012).

These three types of interferometers are performed using white light instead of a laser as the light source due to its short coherence length. Although it is more challenging to match interferometer path lengths, the short coherence length easily eliminates spurious interference fringes caused by any stray reflections from the optical components (Schwider, 1999). Therefore, the accuracy of the interferometers is highly enhanced, up to nanometer range.

2.2.3 *Limitations of existing SWLIs*

Although SWLIs can easily perform non-destructive full-field height measurement with nanometer resolution, present microscopic interferometers still have difficulties to

measure objects in liquid media directly. The major challenge is due to the contradictory phenomena of the optical path length (OPL) and the image path length (IPL) when the light wave goes into a liquid medium. The former becomes n times, but the latter approximately $1/n$ times the geometric path length, if the refractive index of the medium is n.

One scenario is while the microscopic objective (**MO**) focuses on the surface of the object (**O**) in the medium, the optical paths (solid line) and image paths (dashed line) are shown in Figure 2.3(b). The physical lengths of optical and image paths in liquid medium with refractive index n are $n\ell$ and ℓ respectively. In the medium, the wave oscillates with the same frequency but travels at a slower speed. This implies that factor of the wavelength shrinkage is $1/n$. Hence, the OPL for a path of physical length $n\ell$ equals $n^2\ell$ in air (Figure 2.3(c)). In the meanwhile, the identical lens **MO** in RL also focuses on the surface of R (Figure 2.3(a)), and both OPL and IPL are ℓ. In this case, although IPLs in both lines are the same, OPL in OL is n^2 of that in RL. These two waves cannot interfere with each other. On the other hand, while OPLs in both RL and OL are the same (Figure 2.3(d)-(f)), the physical length of optical path is ℓ/n in the liquid medium. The lens **MO** in OL is unable to focus the rays on the surface of **O**. In this instance, although two waves interfere with each other, the interference image is not observable.

Currently, there are two ways to resolve the disentangling phenomena of OPLs and IPLs between the RL and OL. One way is to put a compensating wedge between the lens **MO** and the surface of **R**. It is almost infeasible, since the wedge requires having the same thickness and effective refractive index as those of the medium. The other way is

21
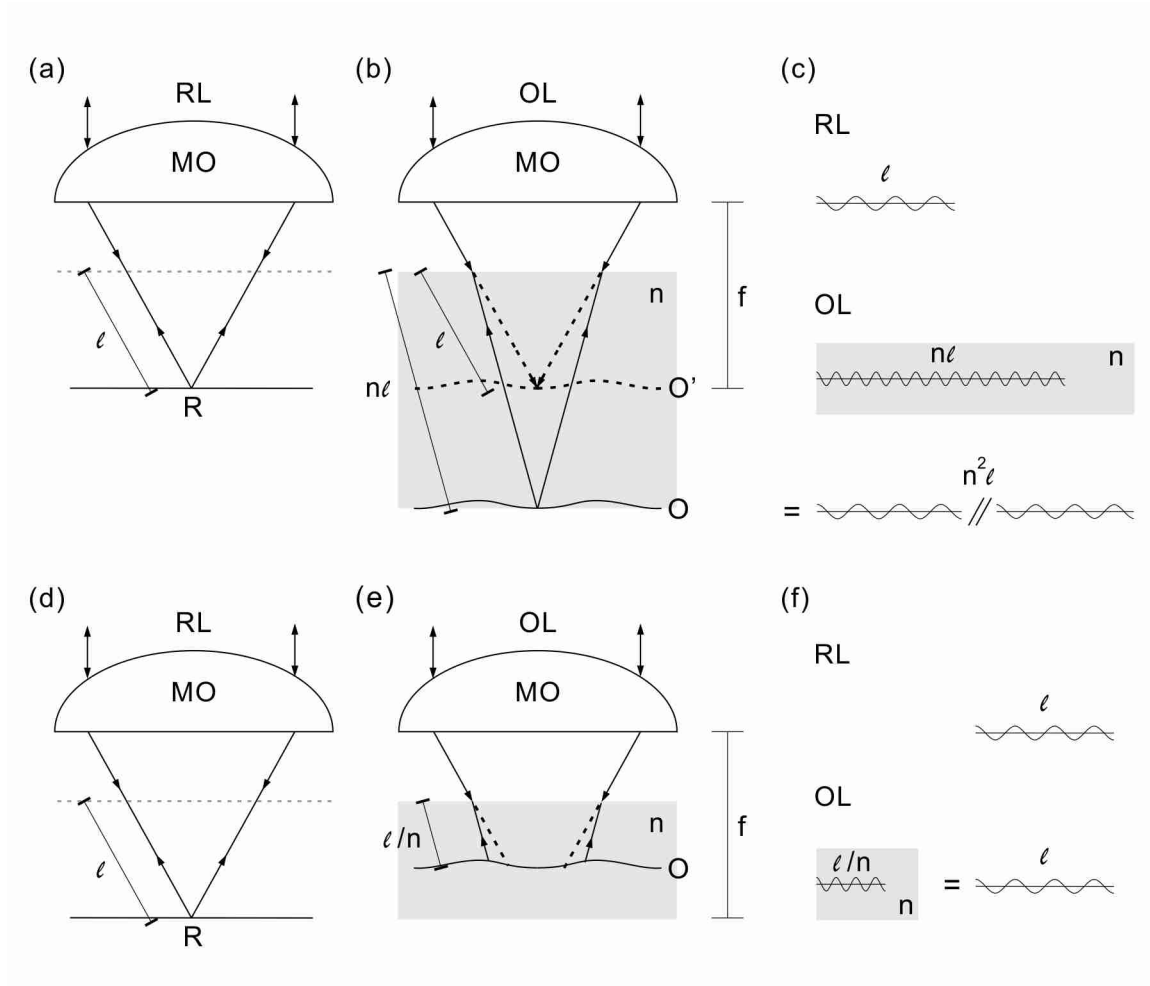
Figure 2.3 The scenario with same image path lengths (IPLs) in both lines: (a) optical and image paths in RL, (b) physical (not phase) optical (solid line) and image paths (dashed line) in OL, (c) the optical path lengths (OPLs) for both RL and OL; analogous figures for the case with same OPLs in both lines: (d)-(f).

immersing both **MO**s into the identical media, i.e., immersion Mirau interferometer (Dubois & Boccara, 2008; Lyulko *et al.*, 2010) or directing both RL and OL to pass through indistinguishable liquid chambers, i.e., liquid cell interferometer (Reed *et al.*, 2008). Although the morphology of **O** in the medium can be measured through the second method, it requires a precise and real-time feedback system to match OPLs and IPLs between RL and OL during measurement by adjusting the position of the lens **MO**

in the reference length RL or that of **R** in the compensated chamber. Otherwise, the interference fringes disappear. Besides, the immersion approach destroys the major advantage of optical experiment – non-contact measurement of the surface profile of **O** without influencing the environment and conditions of the specimen. These two significant drawbacks are the major difficulties to have *in situ* measurement of the morphology of **O** in liquid media via existing technique of SWLIs.

2.3　Principles of SALLI

Self-adjusting liquid Linnik interferometer (SALLI) introduced in this thesis overcomes the above difficulties with a novel optical configuration that naturally self-compensates for any refractive-index change in the liquid medium. Through direct imaging of the specimen, the lateral deformation can be monitored *in situ* with few-micrometers resolution. At the same time, SALLI also permits high precision real-time measurements of changes in the vertical surface position (resolution of 1 nm).

　　The principle of SALLI is shown in Figure 2.4. A cubic beam splitter (**BS**), the key element in the interferometer, has to be rotated 45 degrees. The collimated light beam is then split into two parallel lights (RL and OL). In this particular setup, RL and OL are parallel to each other with a small distance and impinge onto the surface of **R** and **O** through microscopic objectives (**MO1**, **MO2**) simultaneously. Since both **R** and **O** are in the same liquid chamber (**CH**), the OPLs and IPLs of both lights are identical to each other all the time. In this setup, **MO1** and **MO2** do not require immersing into the liquid medium. Accordingly, the environment of the chamber **CH** will not be disturbed. Furthermore, the optical system has self-adjusting function. Even though the amount of
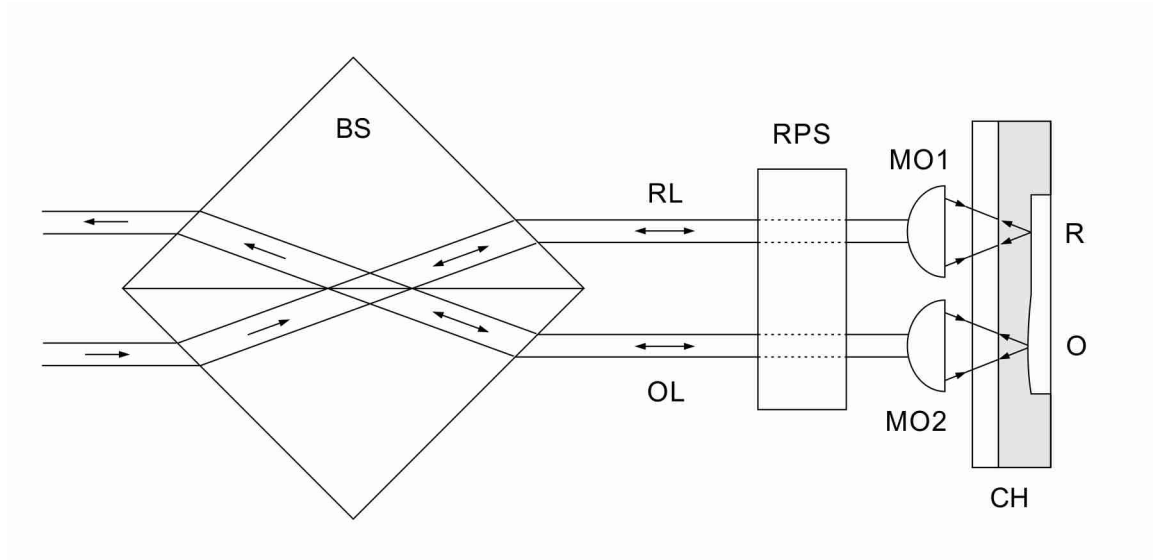
Figure 2.4 The schematic of the principal of self-adjusting liquid Linnik interferometer (SALII). Parts of the interferometer: **BS** – beam splitter, **MO1** & **MO2** – microscopic objective lenses, **RPS** – relative phase shifter, **O** – object, **R** – reference mirror. The optical paths inside **RPS** can be detoured and **RPS** can be placed between **BS** and **MO**s or **MO**s and **CH**.

the liquid may change during measurement, the interference fringe patterns still remain with no need of any feedback system. Therefore, SALLI is suitable for *in situ* measurement of the morphological variation of the live cells, i.e., real-time studying the dynamic motion of electrodes.

In this optical setup, unlike traditional Linnik interferometer, the motions of **R** and **O** are coupled since they are in the same liquid chamber **CH**. Consequently, it is difficult to control the tilts of **R** and **O** independently. In practice word, this implies that the direction and number of the fringes cannot be appropriately adjusted. This is a significant limitation in enhancing the resolution of the measurement. In order to resolve this problem, a novel optical system, the relative phase shifter **RPS**, is introduced in this thesis.

The system **RPS** employs odd number of mirrors in RL and even numbers of mirrors in OL together with a piezoelectric phase controller in one of the optical legs. In this way, the relative tilt between the light wave fronts from **R** and **O** can be controlled by simply tilting the chamber **CH**, while the overall relative phase shift is adjusted by the phase controller. Accordingly, the optical phase difference between **R** and **O** and its gradient can be properly controlled. The optical system **RPS** may be placed between BS and MOs as shown in Figure 2.4 or between **MO**s and **CH**. Although the gradient can be also controlled by tilting a mirror in one of the optical legs, the mirror tilting cause significant displacement of reflection spots on **R** or **O**; therefore, mirror tilting is not a good option of controlling the fringe gradient. The physical experimental setup of SALLI will be further described in section 0.

2.4 Algorithms for SALLI

The algorithms to post-process the optical images are elaborated in this section. First, detect the edge of the sample from the intensity distribution of the images. Convert the interference images to the relative phase maps. Further, unwrap the phase maps to calculate the height profile. In time-sequence measurements, the connection of the fringes may need to be adjusted by shifting the fringe-number jump by an appropriate integer, based on known constraints of the physical phenomena. Finally, an innovative technique and useful schemes are introduced to reduce the noise level of the measurement.

2.4.1 *Detection of the edge of the sample*

To obtain interfacial properties (discussed in next chapter), it is important to record and detect the edge of an electrode during lithiation and delithiation cycles. Here, a scheme is developed to identify the edge of a sample from the intensity distribution of an image.

Figure 2.5(a) is a typical optical image obtained from SALLI. Clearly, the image has been divided into two regions of different intensities. In this case, the reference region **R** has higher reflectivity than **O** as shown in Figure 2.5(b). To properly determine the edge of **O**, we analyze the intensity profiles line by line. Taking AA' row as an example, the black dots in Figure 2.5(c) are the intensity data. Despite the corner effects in the image, a distinct intensity jump can be observed and estimated as

$$I^{(n)}(x_1) = \begin{cases} I_O, & x_1 \leq x_{1O}. \\ \dfrac{1}{x_{1O} - x_{1R}} \left[(I_R - I_O) x_1 + x_{1R} I_R - x_{1O} I_O \right], & x_{1O} < x_1 \leq x_{1R}. \\ I_R, & x_{1R} < x_1. \end{cases} \tag{2.6}$$

I_O and I_R are the average intensities of **O** and **R** respectively. Due to optical diffraction, the intensity increases approximately linearly in the transition zone from x_{1O} to x_{1R} (blue line in Figure 2.5(c)). Minimizing the error functional,

$$E(I_O, I_R, x_{1O}, x_{1R}) = \sum_{x_1} \left| I^{(m)}(x_1) - I^{(n)}(x_1) \right|^2, \tag{2.7}$$

the edge position of the sample **O** (blue circle) is determined by $x_{1edg} = (x_{1O} + x_{1R})/2$, where $I^{(m)}(x_1)$ is the intensity data from SALLI experimental image (black dots).

Apply the scheme to each row and the edge positions are denoted as blue dots in Figure 2.5(d). Finally, distinguish the edge of the sample **O** (cyan line) by a linear fitting.
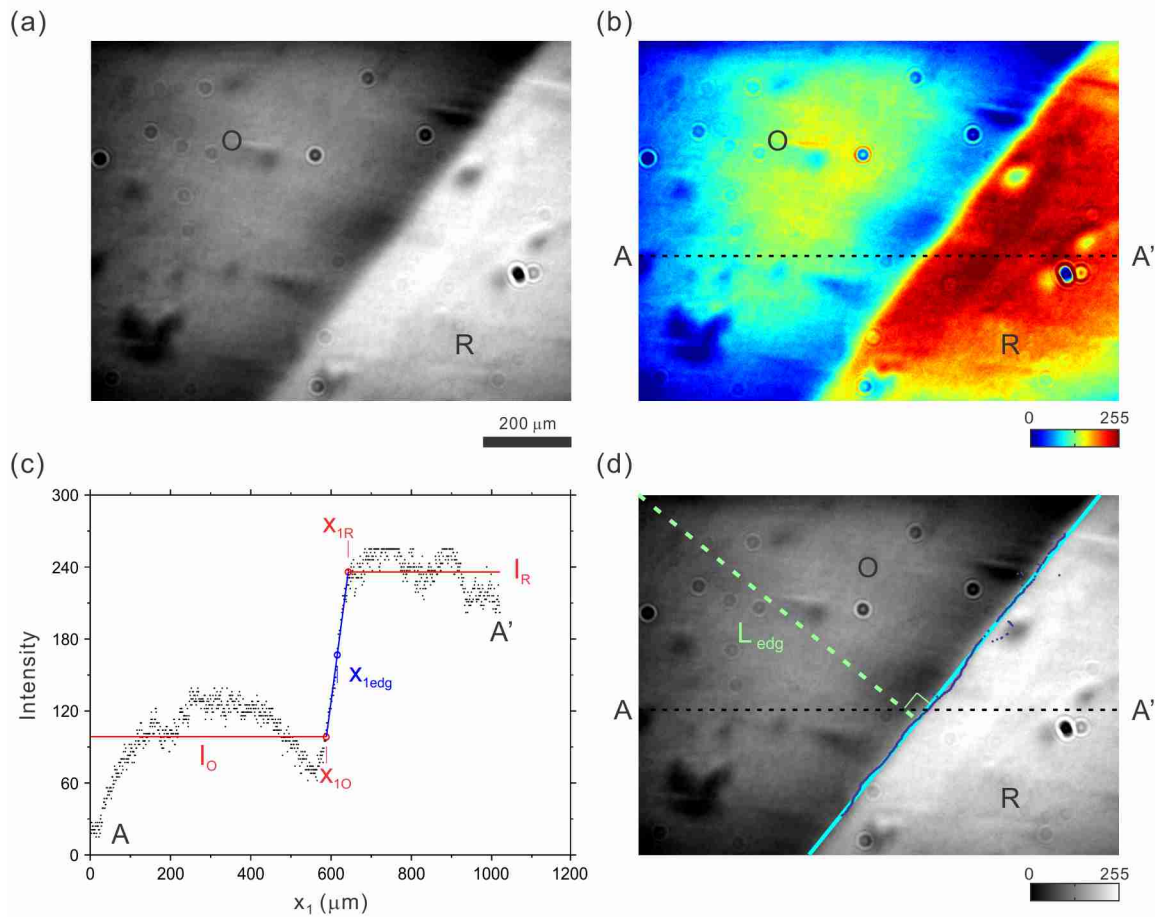
Figure 2.5 (a) An optical image obtained from SALLI. (b) The intensity distribution of the image. (c) The intensity profile of the AA' row. Black dots are experimental data, red and blue lines are the best fitting function. Blue circle represents the position of the edge. (d) The optical image with a cyan line representing the edge of the sample.

Note that L_{edg} is the shortest distance from the left-top corner of the image to the sample edge. This distance is used for *in situ* measurement of the electrode edge motion in cycling experiment.

2.4.2 Computation of phase map

To obtain the relative phase map, the first step is to pre-process the digitally recorded interferograms acquired from SALLI. First remove the background of the image by

27
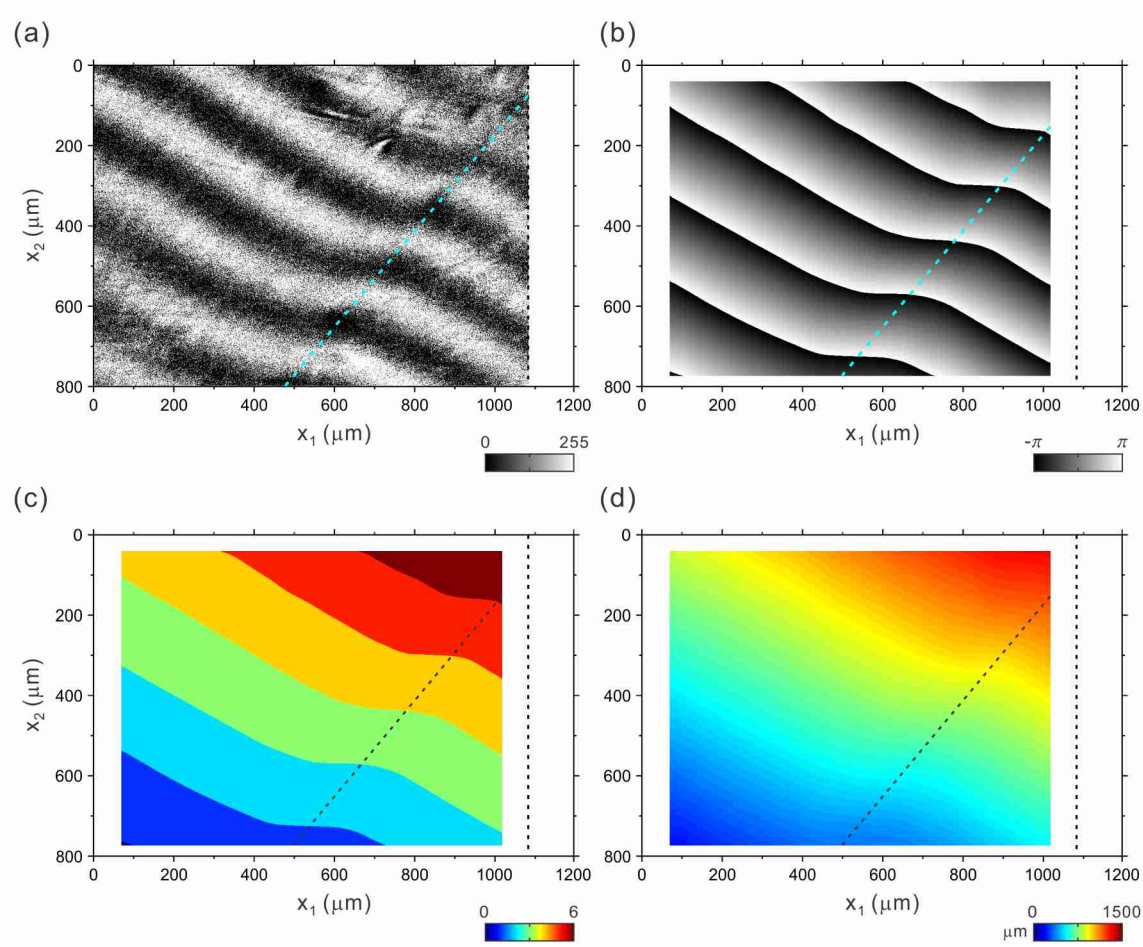
Figure 2.6 (a) A typical interferogram acquired from SALLI after background intensity removal (b) relative phase map (c) distribution of fringe numbers (d) surface profile. Dotted lines in the figures denoted the edge of the sample. The object **O** is in left region and the reference **R** is in right region.

subtracting the image without interference patterns from one with fringe patterns. Then, specify the boundary of the area to be analyzed. Apply a 2D median filtering filter (Matlab `medfilt2` function) to smooth the image. After normalizing the intensity of the image, the clear and distinct interference fringe patterns can be easily distinguished. To better evaluate the local extrema of the intensity distribution, the grayscale image is converted to a binary image. Skeletonize the image by finding the center of the white

28

region, i.e. identification of fringe centres. In this case the phase difference of the interference field at pixels, where an intensity maximum is located, equals an even integer multiple of π. Finally, reconstruct the phase values from $-\pi$ to π via using techniques of linear interpolation. A typical interferogram obtained from SALLI after removing background intensity is shown in Figure 2.6(a), and Figure 2.6(b) is the corresponding post-processed phase map.

Number interference fringes from one of the corners of the skeletonized image to unwrap the relative phase map. To properly select the starting fringe, the physical geometry of the sample is required. Since the object **O** (i.e., left region in the image domain) in this experiment is physically thicker than the reference **R**, the first fringe begins from the left-bottom corner as illustrated in Figure 2.6(c). Once the unwrapped phase map is obtained, the surface profile (Figure 2.6(d)) is calculated from the relationship derived in equation (2.5), where d is the thickness, n the refractive index of the liquid medium, λ the wavelength of the light source, and m the fringe fractional number from the unwrapped phase map.

Some interference images, e.g. Figure 2.7(a), have at least two possibilities to link the fringes: one is A-A1 and the other is A-A2. These two different judgments result in one phase difference, i.e., $\Delta h = \lambda / 2n$ in height distribution, between **O** and **R**. In static measurements, the ambiguity can be avoided by adjusting the fringe width to have a more distinct and separate fringe patterns. However, it is not feasible in *in-situ* experiments. Although the initial fringe pattern is tuned to be clear, it may become vaguer and vaguer while the thickness of the sample increases and decreases during measurement. Moreover, if the thickness change is relatively large, the fringe may need to be connected to next

29
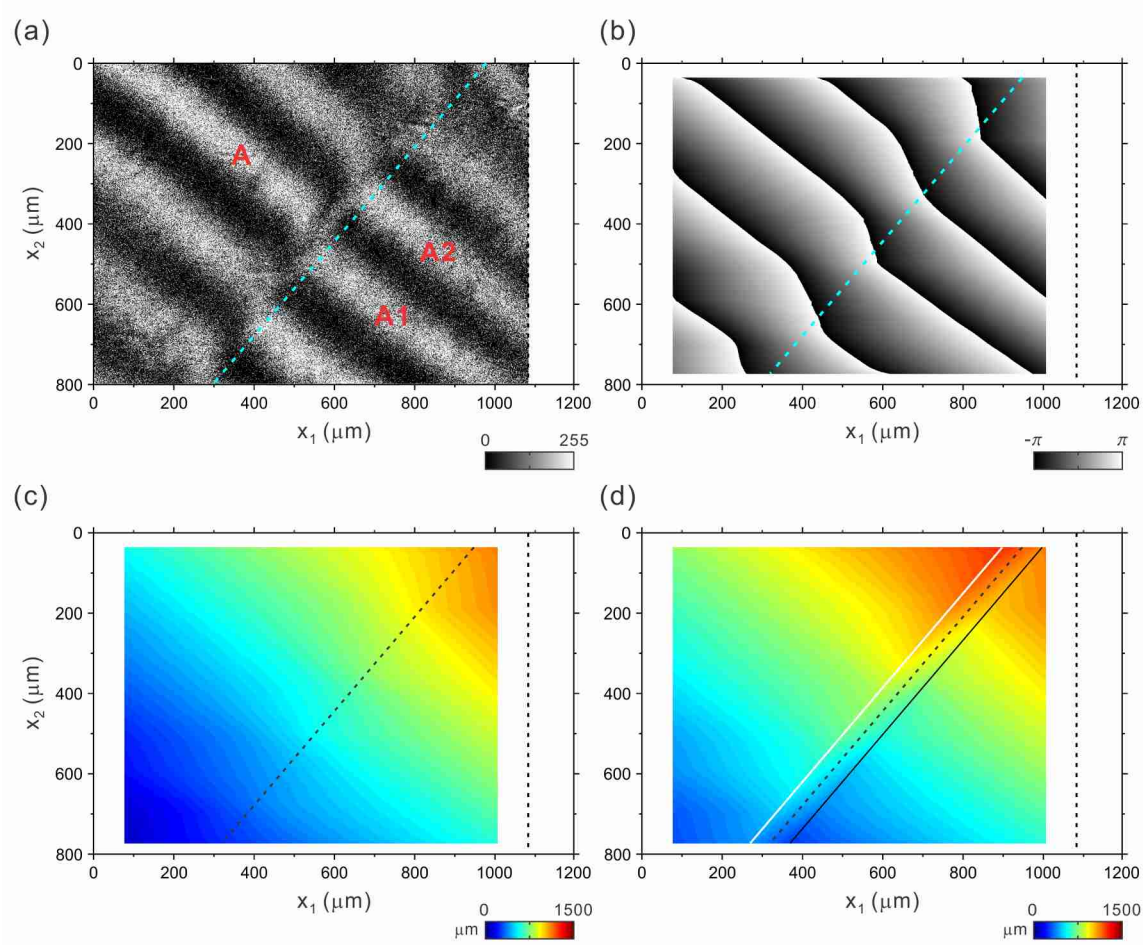
Figure 2.7 (a) An interferogram obtained from SALLI after background removal (b) relative phase map (c) surface profile before adjustment (d) surface profile after adjustment. Dotted lines in the figures denoted the edge of the sample. The transition region for adjusting fringe connections is enclosed by two solid lines (white and black).

closer one instead. Therefore, it is essential to determine the fringe connection properly, especially in time-dependent measurements.

In this experiment, we always connect the fringe to the nearest one and count the fringe number from the left-bottom corner of the image. Once the height profile in **O** region becomes smaller than that in **R** region (Figure 2.7(c)), the result disagrees with the physical phenomena. Then, the fringe connection should be adjusted and the thickness

30

distribution in **O** should be added by Δh (Figure 2.7(d)). Note that the transition zone for adjusting fringe connection is defined as ± 50 μm away from the edge of the sample.

2.4.3 Noise reduction technique

Although SALLI has the same advantages, e.g., high lateral resolution with a long working distance, as Linnik interferometer has, it also inherits disadvantages. The major drawback is its sensitivity to mechanical and thermal disturbance in its alignment with a long optical path. To reduce the noise and rigid-body drifting movement during the measurement, an innovative technique is introduced here.

In the SALLI system, the reference **R** and the object **O** are required to be on the same wafer and sealed in the same chamber **CH**. Here, **O** is only deposited on the quarter of the wafer which is illustrated as a light gray region in Figure 2.8(a). The rest of the wafer is the region of **R**. The two light beams (RL and OL) impinge on the surface of the sample as shown in upper and lower dark gray circles respectively. The former circle is considered as a reference spot and the latter one is the measuring area. The interference fringe patterns (Figure 2.8(b)) are obtained while RL and OL interfere with each other. Here, the edge of the sample (cyan line) is detected by the scheme elaborated in sub-section 2.4.1. The left region (denoted as **O**) of the interferogram is contributed from O-R interference and the right portion (**R**) represents **R-R** interference. Post-process the fringe patterns to determine the surface profile by using algorisms described in sub-section 2.4.2. Since **R-R** interference region does not have any thickness change during the measurement, any deformation information acquired from this region is all caused by environmental disturbance. Therefore, by flattening the height variation of the **R** region
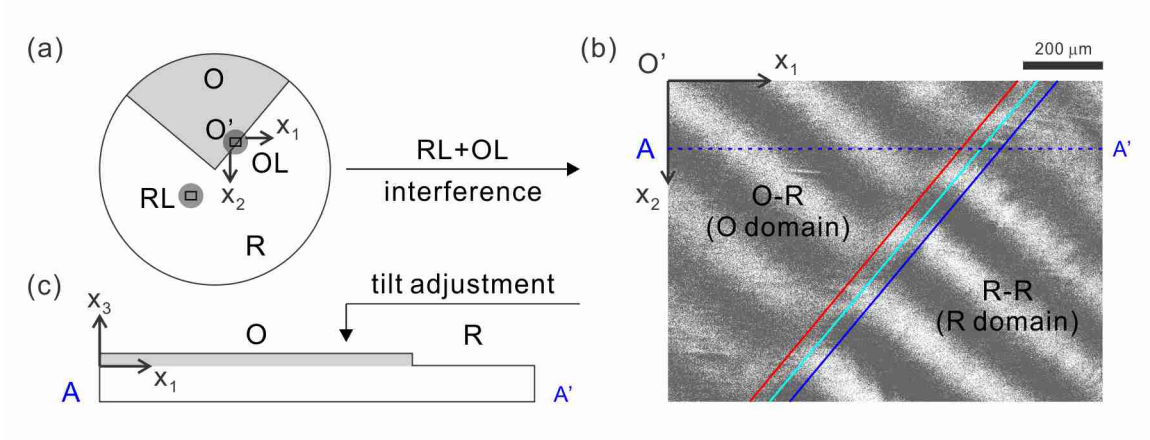
Figure 2.8 (a) A schematic of the sample design. (b) The corresponding interferogram, a real experimental image acquired from SALLI with 50% transparency. (c) A schematic of the flattened surface profile along A-A' line.

with an adjustment algorithm of a rigid body motion, the noise-free thickness distribution in the object **O** region is obtained with respect to the reference **R** region.

The tilt adjustment scheme is introduced as following. Choose the left-top corner as origin O' and the coordinate as $\mathbf{x} = x_1\mathbf{e_1} + x_2\mathbf{e_2}$ (Figure 2.8(b)). Define the tilt plane equation as $h_0(\mathbf{x}) = ax_1 + bx_2 + c$, where a, b, and c are to be determined by minimizing the error functional,

$$E(a,b,c) = \int_{S_O} \left| h_O^*(\mathbf{x}) - h_0(\mathbf{x}) \right|^2 dS + \int_{S_R} \left| h_R^m(\mathbf{x}) - h_0(\mathbf{x}) \right|^2 dS. \tag{2.8}$$

Here,

$$h_O^*(\mathbf{x}) = h_O^m(\mathbf{x}) - \left(\overline{h}_O - \overline{h}_R \right) + \left\{ a\left(x_{1O}^C - x_{2O}^C \right) + b\left(x_{1R}^C - x_{2R}^C \right) \right\} \tag{2.9}$$

with $\left(\overline{h}_O, \overline{h}_R \right)$ the area average of the thickness, $\left(h_R^m(\mathbf{x}), h_O^m(\mathbf{x}) \right)$ the thickness data measured from SALLI in the respective region of **O** and **R**, and $\left(\mathbf{x}_O^C, \mathbf{x}_R^C \right)$ the centroid positions of domain **O** and **R**. Note that the domain **O** (the left side of the red line in

32

Figure 2.8(b)) and **R** (the right side of the blue line) are the region ± 50 μm away from the edge of the sample. Finally, the height function after tilt adjustment is determined by

$$h^{tadj}\left(\mathbf{x}\right)=h^{m}\left(\mathbf{x}\right)-h_{0}\left(\mathbf{x}\right).$$

(2.10)

Through this technique, the noise and the rigid body motion have been removed. Furthermore, since the thickness in **R** region is zero after tilt adjustment (Figure 2.8(c)), it is considered to be the global reference plane in the time-dependent experiment.

2.5   Experimental Procedures

As mentioned in the previous section, SALLI can monitor the edge deformation with a micron-scale resolution, and permit high precision measurements of changes in the vertical surface position with 1 nm resolution. Thus, this *in situ* capability makes it possible to fully monitor the silicon electrode shape as it evolves during lithiation and delithiation cycles. This time-dependent measurement provides critical information about the Li distribution in the Si thin-film electrode and the corresponding deformation. The detailed experimental procedures, the optical setup of SALLI and the design of the half-cell battery are described in this section.

2.5.1   *Optical setup of SALLI*

The physical arrangement of the apparatus, SALLI, is illustrated in Figure 2.9. The quartz halogen light source (**WLS**) was first collimated after going through a mirror **M1** and a lens **L1**. The diameter and the intensity of the beam were further controlled by an aperture A and a circular neutral density filter. The light beam was split into two beams, the reference beam RL and the object light OL, by a cubic beam splitter **BS**. To enlarge
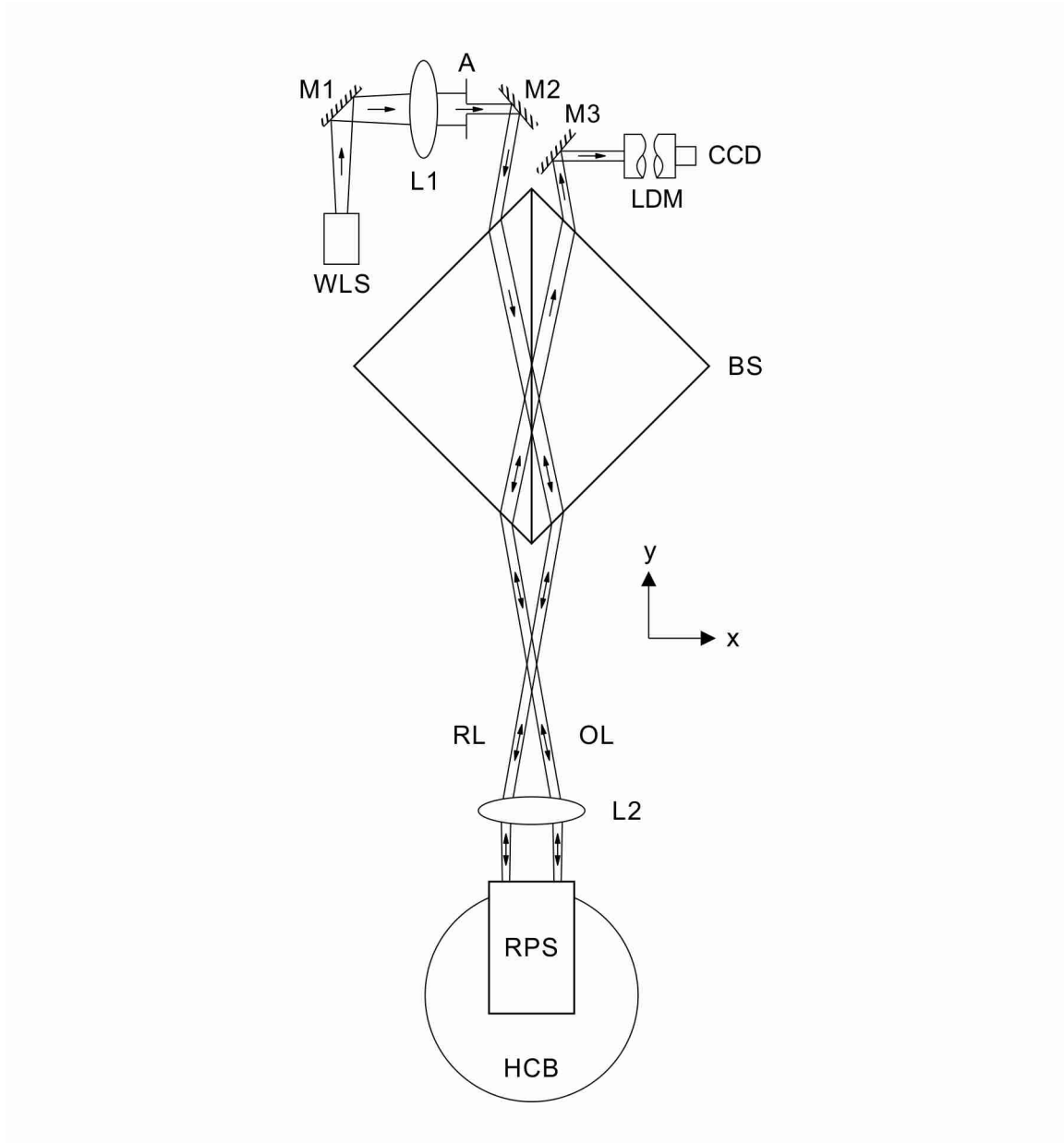
Figure 2.9 The optical setup of the self-adjusting liquid Linnik interferometer (SALLI).

the magnification of the view, a lens **L2** was used. The lights had been set up to cross

each other before **L2**. The position of the cross point could be adjusted by the mirror **M2**

before the light beam reached BS. Since the distance from the cross point to the lens was

designed to be the focal length of **L2**, two beams became parallel and impinged onto the
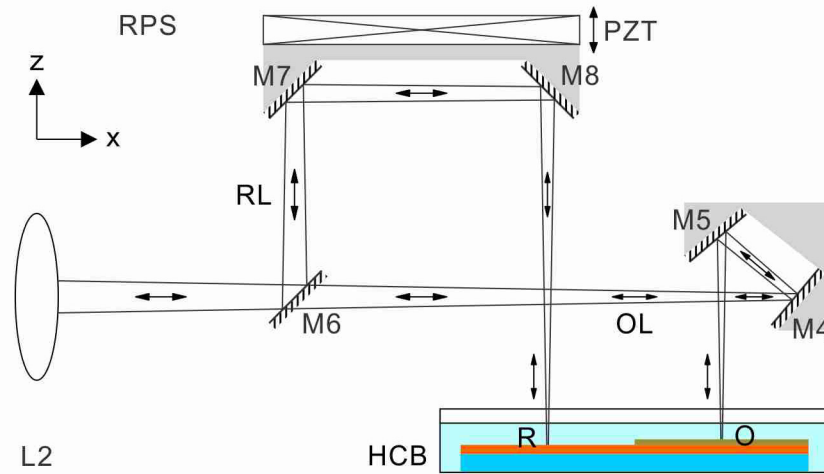
Figure 2.10 Expanded side view of the key elements, relative phase shift (**RPS**), of the SALLI. Only illumination light is shown in the figure; reflected light is too complicated to draw in the same figure. Note that the angles of **M4** and **M5** were fixed and they were mounted on one stage.

surfaces of **R** and **O** in the half-cell battery (**HCB**) trough **RPS**. Finally, the light beams reflected from these two surfaces interfered after they intersected inside **BS**. Therefore, the fringes were observed from the long distance microscope **LDM** and recorded by a CCD camera.

To enhance the resolution of the measurement, the optical system, a relative phase shift (**RPS**) shown in Figure 2.10, was added after **L2**. Two light beams, RL and OL, were parallel to each other after going through **L2**. OL was reflected by two front-surface mirrors **M4** and **M5**. Then, it had been redirected to the surface of the object **O**. On the other hand, RL was reflected by three front-surface mirrors: **M6**, **M7**, and **M8**. Finally, it impinged on the reference spot, **R**. The setup of **M7** and **M8** was used as a 180° retro-reflector which reflected the incidence light through 180° at a separate distance. Two mirrors were mounted on one linear translation stage controlled by piezoelectric actuators

PZT with a resolution of 0.06 μm. By adjusting the position of **M7** and **M8**, the optical phase difference (OPD) between RL and OL could be modified. When the OPD was within the coherence length of the white light (< 3 μm), the interference fringes appeared. With this design, the movements of **R** and **O** could be separately controlled, and the widths and directions of the fringes could be adjusted by tilting the chamber **HCB**. Note that the details of **HCB** design will be discussed in the next section.

Functionality of SALLI including **RPS** was verified by comparing the white light interference fringes with those of a commercial (air) Linnik-interferometer microscope, the Reflected Light Interference Microscope made by Leitz Wetzlar Inc., as shown in Figure 2.11. The light-reflecting object of the test was a thin titanium film deposited on a silicon substrate. Figure 2.11(a) shows the fringes made by the Leitz microscope, interfering the light from the object and that from its internal reference mirror. The light source of the microscope was a tungsten filament lamp. Figure 2.11(b) displays the fringes produced by SALLI without a liquid medium, i.e. in the air, interfering the lights from the surfaces of titanium object and the silicon reference. The light source for SALLI was a halogen bulb. Figure 2.11(c) exhibits the SALLI fringes formed through the water medium, when the silicon wafer half of which was coated by the thin titanium film was sitting in the **HCB** chamber filled with water. Indeed the white light interference fringes generated by SALLI in air and water were as clear as those of Leitz microscope regardless of the medium surrounding the object. The fringe patterns in Figure 2.11(d) −(f) demonstrate controllability of fringe directions (and spacing) with **RPS** by simply adjusting the tilt angle of the stage carrying **HCB**.
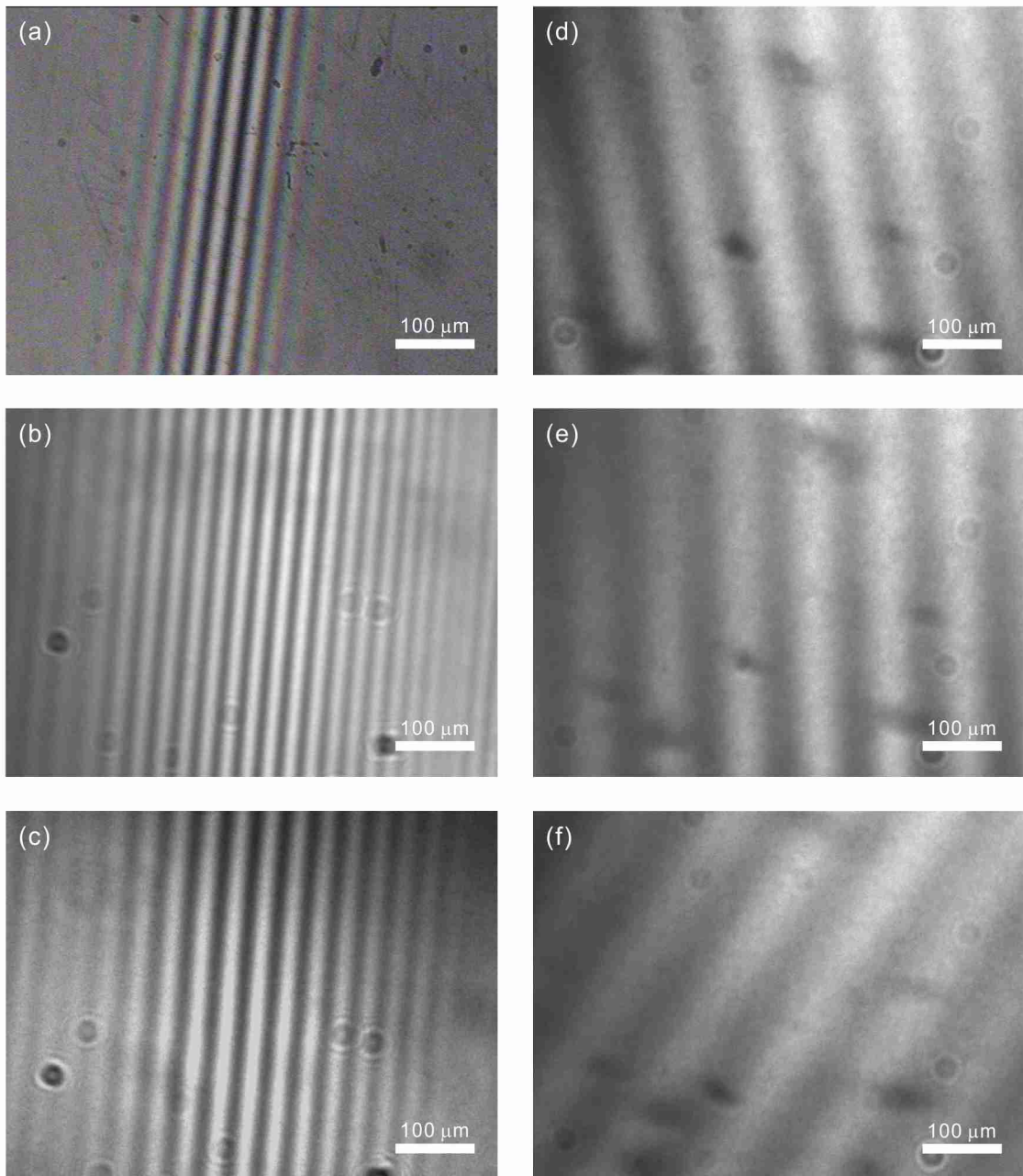
Figure 2.11 Optical interference fringes for validation of SALLI((a)-(c)) and for testing the function of **RPS** ((d)-(f)). The same object was measured by a commercial (air) Linnik-interferometer microscope, (air) SALLI, and (water) SALLI shown in (a)-(c) respectively.

A halogen bulb with the maximum transmittance at 600 nm wavelength was used as the white light source in the SALLI system. The coherence length of the bulb was estimated approximately 3 μm from the number of visible fringes in Figure 2.11(c). To reduce any spurious fringes made by reflections from optical components, all of the components had anti-reflective (reflectivity at $400 - 700$ nm wavelength) coatings on the surfaces. By using the halogen bulb, SALLI could measure the surface profile in 1 nm resolution.

The in-plane resolution was estimated by imaging the marker of a copper film on a silicon substrate in the half-cell battery, which was sealed in the water without applying any electrical voltage on the battery. The images were recorded in every 3 seconds for five hours. Eighty frames were selected to estimate the amplitude of the intrinsic vibration in this setup. From the correlation analysis, the amplitude was estimated to be 8 μm in both x and y directions. Also, 200 frames (equal to 10-minute duration) were selected to investigate the vibration frequency by using FFT. The major frequencies of the vibration along x and y directions are 0.05, 0.083 Hz (period: 20, 12.05 sec) respectively. The periods of the intrinsic vibration are much shorter than those of the charge and discharge cycles in the SALLI experiments.

2.5.2 *Electrochemical half cell preparation and test*

The design of the half cell battery[1] is shown in Figure 2.12. A 200 nm thick Cu current collector and a 10 nm thin Ti adhesion layer were first deposited on high purity double side polished SiO_2 substrates (25.4 mm in diameter and 250 μm thick). These were

---

[1] Courtesy to Anton Tokranov and Brain Sheldon, for designing the chamber and making all the cells measured by SALLI.
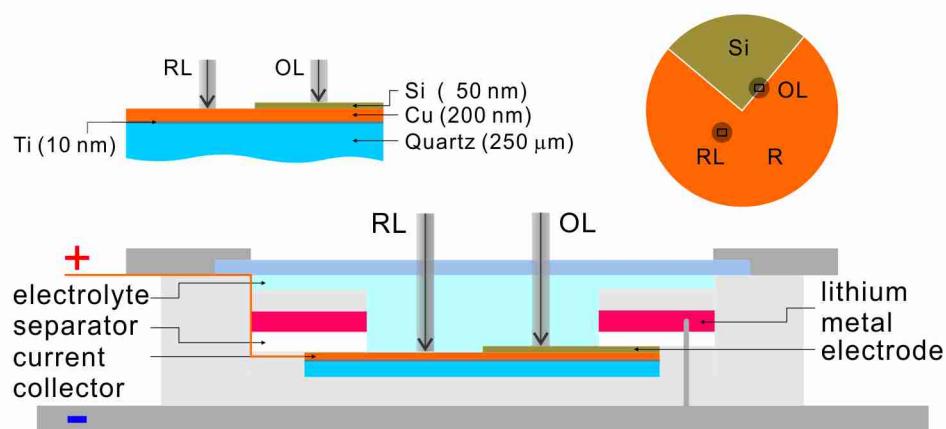
Figure 2.12 Schematic illustration of the half cell battery (**HCB**). Insets are the detailed dimensions of the Si electrode and top view of the sample.

cleaned in acetone, methanol, isopropanol and deionized water, and then mounted in LeskerLab-18 thin film deposition system. Ti, and Cu were deposited at a fixed deposition rate of 0.1 nm·sec^{-1}, using e-beam deposition. Sample was then removed from the chamber and $3/4$ of the Cu was masked by kapton tape. 50 nm of amorphous Si was then deposited at a fixed deposition rate of 0.1 nm·sec^{-1} for 500 seconds, during which the base pressure of the chamber was $< 2 \times 10^{-6}$ Torr and the deposition rate was monitored with an Inficon QCM (Quartz Crystal Mircrobalance).

The wafer with Si electrode was then assembled into a home-made electrochemical cell with a MgF_2 coated glass window (diameter = 40 mm, thickness = 3 mm). During assembly, the Si sample was placed at the bottom of the cell, followed by the Celgard separator and pure lithium metal which was used as a counter electrode. To provide optical access to the surface of the Si films, both separator and lithium metal had 13 mm diameter holes cut in the middle. The cell was then filled with the liquid electrolyte, an 1:1 mixture of ethylene carbonate (EC) and dimethylecarbonate (DMC)

containing 1 M $LiPF_6$ salt. The entire assembly was constructed in a glove box filled with ultra-pure argon and the seal in the cell were maintained using Kalrez o-ring.

The cell was subjected to galvanostatic cycles (at constant currents) against metallic Li between 2.2 V and 0.05 V vs. Li/Li$^+$, using the electrochemical cycling rates $C/7$ (-30 μA) and $C/2$ (10 μA) for the first cycle. They were set to be -25 μA and 10 μA respectively for following cycles. The lower limit of 0.05 V vs. Li/Li$^+$ was chosen to avoid crystalline phase ($Li_{15}Si_4$) formation below this critical voltage (Obrovac & Christensen, 2004). The cell required higher currents due to large amount of electrolytes in the cell.

Through this setup, RL impinged on the Cu surface and OL focused on the surface of the Si film (Figure 2.12). Therefore, the relative thickness change between the Si electrode and the Cu current collector was measured during lithiation and delithiation cycles. During cycling, the CCD camera automatically record 8-bits monochrome frames (1024×768 pixel resolution) every 6 seconds with 39 μs shutter time.

2.6   Results and Discussions

The electrochemical behavior of an amorphous Si thin film electrode was *in situ* measured and recorded during galvanostatic discharge and charge cycles. The interference fringe patterns from SALLI for the first two cycles are displayed in the first column of Figure 2.13 to Figure 2.15. In this measurement, one fringe represented 196 nm thickness differences. During the first lithiation cycle, the micro bubbles were forming and flowing to all directions, e.g. two micro bubbles were discovered in the
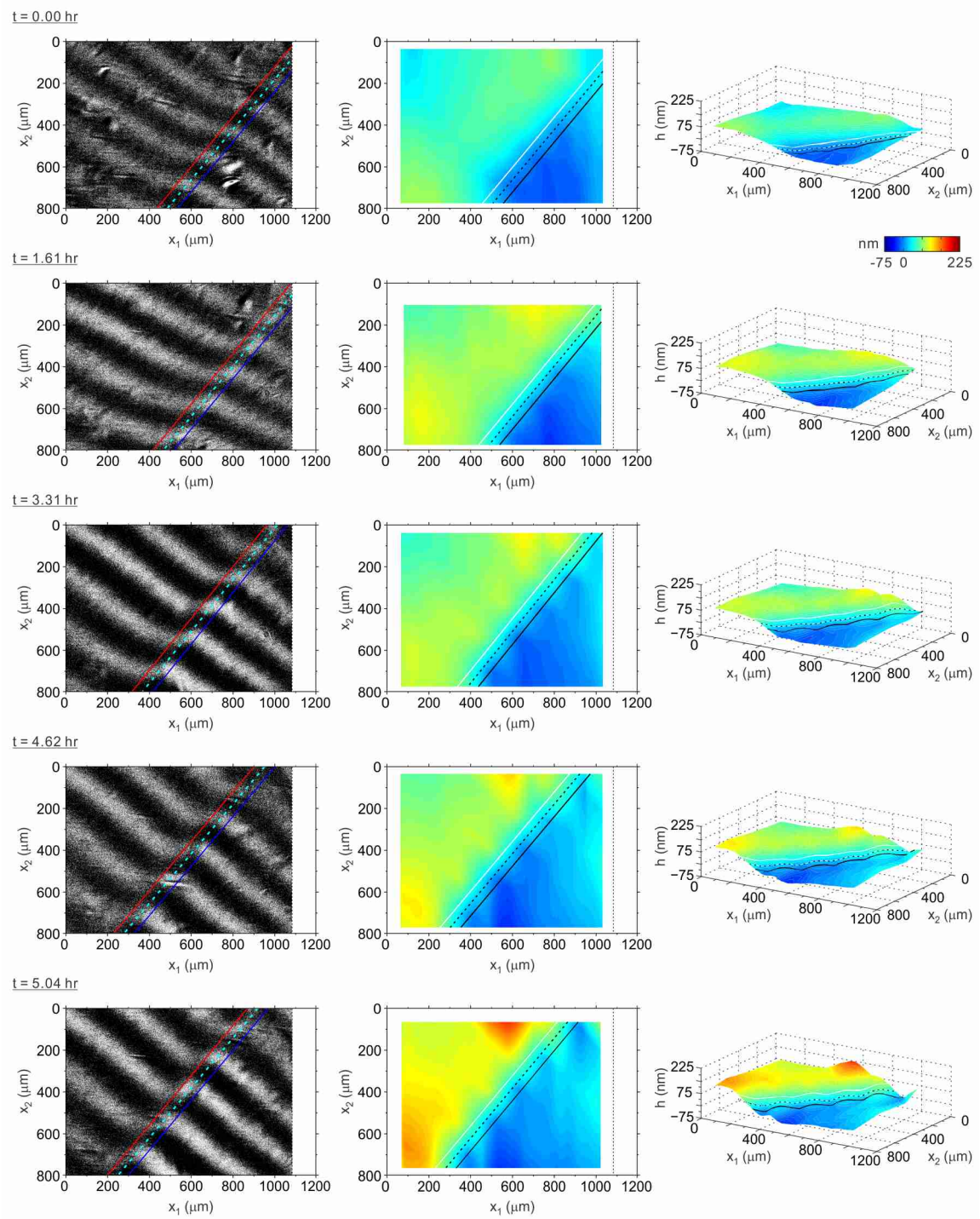
Figure 2.13 The time-dependent *in situ* SALLI results on a 50 nm Si film during the first cycle. The edge of the film is denoted as dotted line. Note that in the image domain a-Si is on the left and Cu on the right side. Distinct movement of the electrode edge, up to 200 μm, was observed from the fringe images (first column). 2D and 3D contours illustrate the out-of-plane deformation field. The color bar is shared for all 2D and 3D contours.
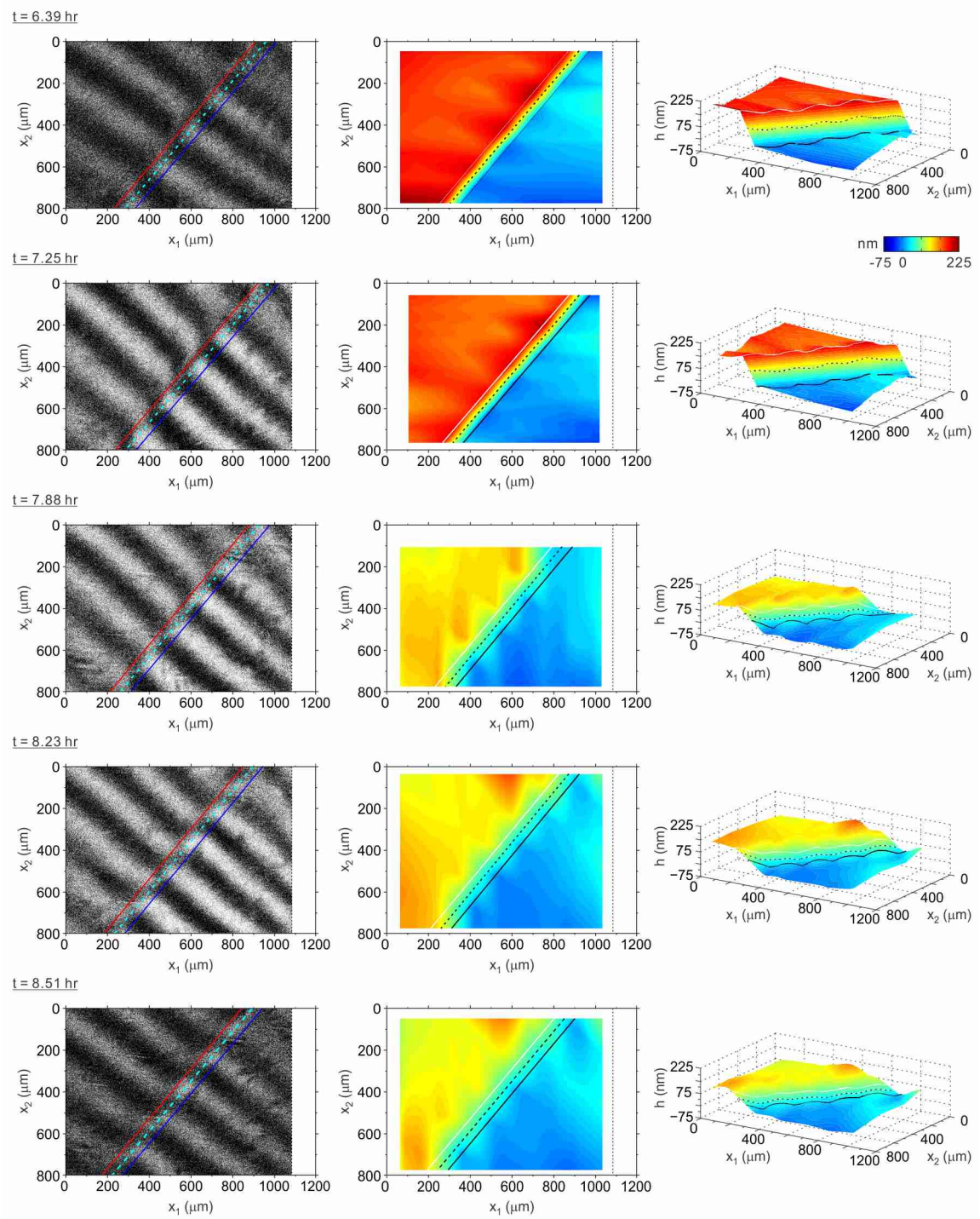
Figure 2.14 The time-dependent *in situ* SALLI results on a 50 nm Si film during 6.39 − 8.51 hour of the first cycle. Continue from the previous figure. The movement of the electrode edge was approximately 50 µm. The thickness variation is inhomogeneous especially during delithiation cycle.
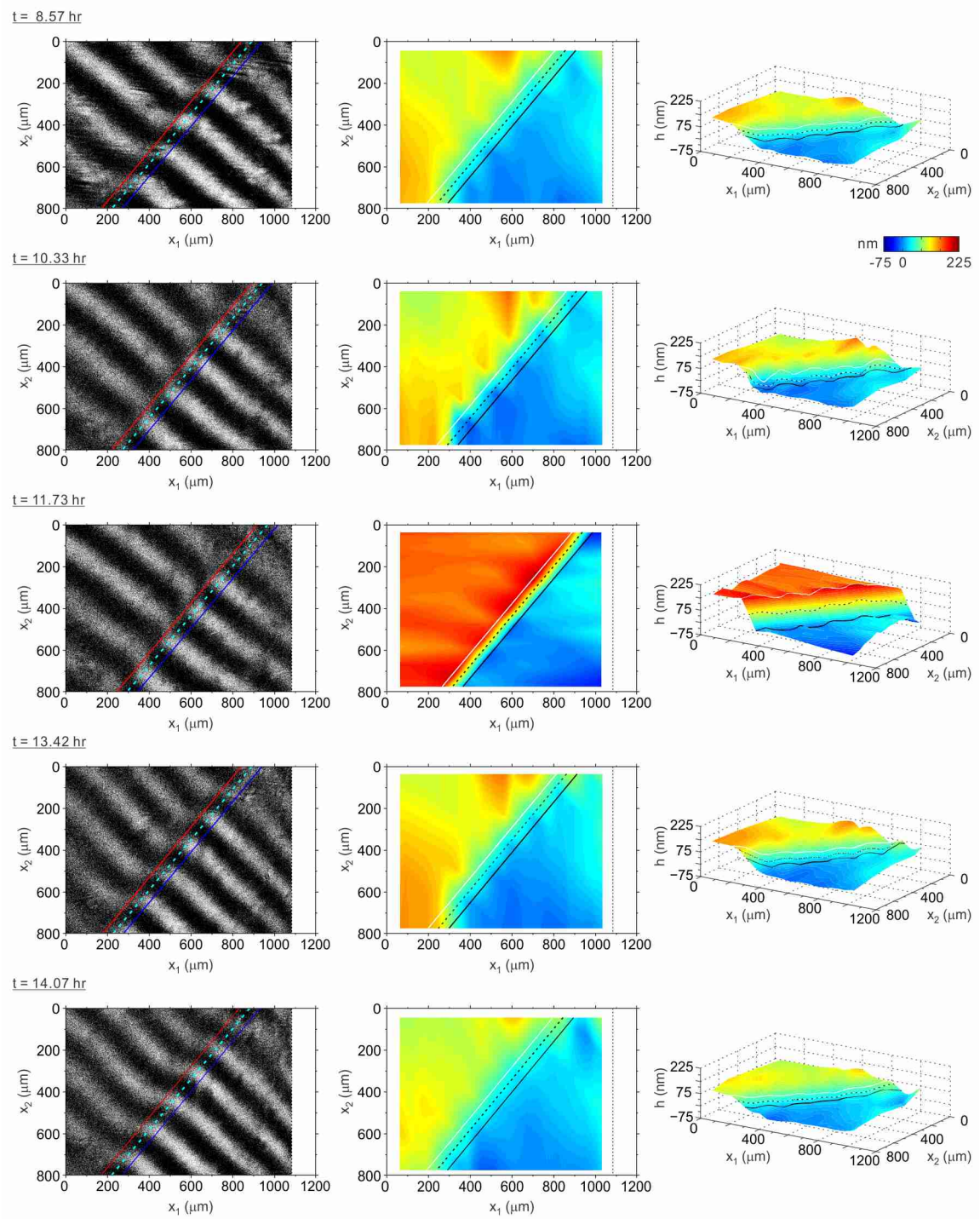
Figure 2.15 The time-dependent *in situ* SALLI results on a 50 nm Si film during the second cycle. The movement of the electrode edge was within 50 μm. It expanded during lithiation (8.5 − 11.73 hour) and shrank back to the bulk during delithiation (11.73 − 14.07 hour). The thickness distribution is non-uniform.
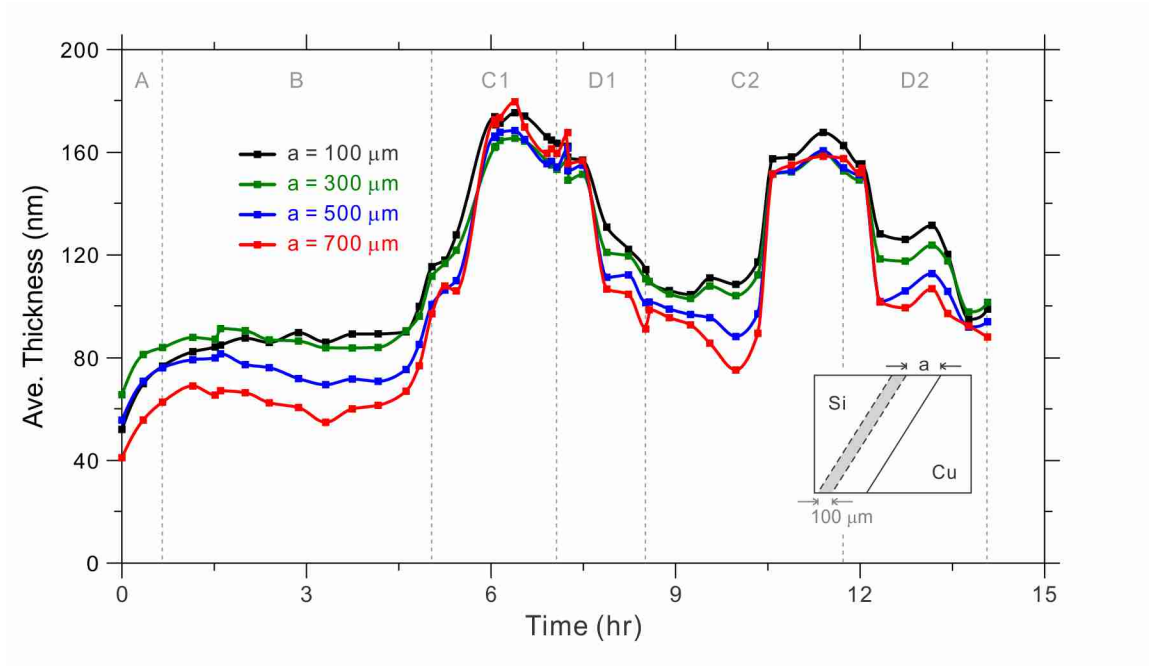
Figure 2.16 The area-average thickness from different average domains during the first two cycles.

fringe pattern recorded at 1.61 hour (Figure 2.13). 2D and 3D contours (the 2nd and 3rd columns in Figure 2.13 to Figure 2.15) show the surface topography of the a-Si film during cycling. Lithiation started at the edge of the Si film and diffused into the bulk (left top corner) region. On the other hand, delithiation began at the bulk region. Overall, the film expands during lithiation cycle and shrinks during delithiation process. At the end of the first two cycles, partial electrode deformation is irreversible and it could be caused by SEI formation. This time-dependent information provides critical information about the Li distribution in the Si, and the corresponding deformation.

The history of area-average thickness is plotted in Figure 2.16. The color of the lines indicates the domain, with 100 μm width and a μm away from the edge, for estimating average. While silicon was fully charged, the thickness expansion was 213.9%,
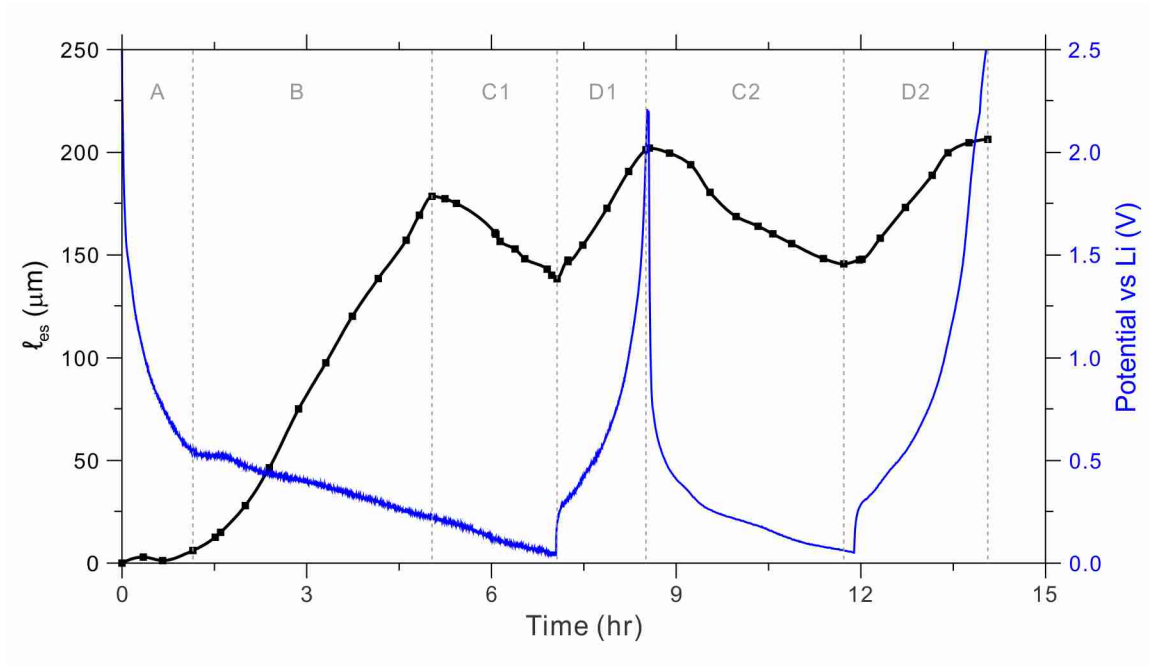
Figure 2.17 The sliding distances *in situ* measured by SALLI along with the potential history. ℓ_{es} in positive represents the film shrinks in in-plane direction; otherwise, the film expands.

133.7%, 176.9%, 288.0% for a = 100, 300, 500, 700 μm respectively. Note that the thicknesses contributed from the substrate bending are included in Figure 2.13 to Figure 2.16.

The history of the area-average thickness of the a-Si electrode has periodic behaviors. It expanded up to 172.77 nm (165.73 nm in 2nd cycle) during lithiation and shrank back to 106.51 nm at the end of the first cycle (94.42 nm in 2nd cycle). Besides, the initial height increased before significant Li insertion into the Si film (before 1.52 hour in Figure 2.16), and is thus due to initial SEI formation on top of the copper current collector. It is well established that SEI significantly impacts safety, capacity fade and battery life (Aurbach, 2000; Dedryvère *et al.*, 2005). Thus, the further information of SEI

formation and evolution extracted from the SALLI experiment will be discussed in the next chapter.

The lateral expansion of the Si edge was also monitored *in situ* via SALLI. As illustrated in the first column of Figure 2.13, the Si edge shrank into the bulk region for approximately 200 μm at the beginning of the first cycle (0 – 5.04 hour). During this massive sliding period, the thickness of the Si electrode grew slightly (Figure 2.16) and uniformly (Figure 2.13), especially before 4.62 hour. Then, the Si edge slightly expanded and shrank in the following cycles. The movement of the electrode edge here was within 50 μm.

To better understand the sliding mechanism of the electrode, the sliding distance ℓ_{es} of the Si edge (Figure 2.17) is compute from $L^0_{edg} - L^i_{edg}$. Referring to sub-section 2.4.1, L^i_{edg} is the distance from the left-top corner of the image to the sample edge and L^0_{edg} represents that distance in the reference configuration (before cycling). Initially the sliding distance suddenly jumps from zero to 6.1 μm in stage A. Then, there is unexpected shrinkage (stage B) of the film, that appears to be driven by the relaxation of residual tensile stress generated during lithiation. This observation is consistent with the low friction due to Li segregation at the a-Si/Cu interface which was calculated by Stournara *et al.* (2013). Then, the film expands due to massive volume increase caused by Li insertion (stage C1 and C2 for the 1st and 2nd cycles respectively). This is followed by contraction of the film during delithiation (stage D1 and D2). The latter two motions (stage C and D) are reversible during the first two cycles.

2.7 Concluding Remarks

The new apparatus SALLI has been invented in this thesis to perform *in situ* whole field deformation measurement during lithiation and delithiation cycles. Its novel optical configuration not only resolves the disentangling phenomena of optical path length (OPLs) and image path length (IPLs), but also has ability to naturally self-compensate for any refractive-index change in the liquid medium. Through direct optical images obtained from SALLI, the lateral expansion of the electrode edge was recorded (with 8 μm resolution). At the same time, SALLI with the help of the noise reduction technique permitted high precision measurements of changes in the out-of-plane direction (resolution of 1 nm).

This time-dependent information provides critical information about the Li distribution in the Si, and the corresponding deformation. Such experimental results also indicate the occurrence of the low friction due to Li segregation at the a-Si/Cu interface. Both in-plane sliding distances and out-of-plane deformations are important information for extracting the sliding properties at a-Si/Cu interface (shown in the next chapter).

Chapter 3.

SHEAR CHARACTERISTICS OF A-SILI$_X$//CU INTERFACE UNDER ELECTROCHEMICALLY ACTIVE SEGREGATION OF LITHIUM

3.1   Introduction

Silicon (Si) with ultrahigh theoretical capacity (4200 mAh/g in the form of Li$_{22}$Si$_5$; Boukamp *et al.*, 1981) has been widely investigated as one of potentially the best negative electrodes in high power density lithium-ion batteries (Chan *et al.*, 2008). However, up to nearly 400% volume expansion (Beaulieu *et al.*, 2001) during Li insertion induces large stresses and leads to serious mechanical degradation, such as fracture of electrodes, pulverization of Si particles, and delamination of the film from the adjacent materials (Maranchi *et al.*, 2003; Xiao *et al.*, 2011). This failure resulting in early capacity loss and shortening battery lifetime has been shown in different Si nanostructures, e.g., thin films (Bourderau *et al.*, 1999; Maranchi *et al.*, 2006), nanowires (Liu *et al.*, 2011; Ryu *et al.*, 2011), nanoparticles (Liu *et al.*, 2012; McDowell *et al.*, 2013), and Si-C composites (Guo *et al.*, 2005; L. Q. Zhang *et al.*, 2011).

Several techniques were proposed to accommodate this lithiation-induced large strain (Graetz *et al.*, 2003; Yao *et al.*, 2011). One approach is using porous Si-C nanocomposites as anodes. Recent development by Magasinski *et al.* (2010) showed that

the porosity of the composites can effectively accommodate the large volume change due to lithium insertion. In this way, the electrode can have both high capacity provided by Si and better electrical conductivity from C. Besides, in this structure the optimized interfaces between these two materials can shorten lithium insertion pathways and maintain better electronic contacts. Similar fast Li transport through a-Si/C interfaces has been observed in a-Si coated carbon nanofibers (J. W. Wang *et al.*, 2012) and Si-beaded carbon nanotude strings (Sun *et al.*, 2013).

The other approach is to alleviated these large stresses by interfacial sliding between thin film electrodes and adjacent materials. According to density functional theory (DFT) calculations (Stournara *et al.*, 2013), Li segregates the interface during lithiation cycles. It softens the interfacial strength and changes the bonding of the interfaces. This interfacial instability induces interfacial sliding which results in accommodating large volume change and then further enhances the life cycle of LIBs. The experiments and theoretical studies by Soni *et al.* (2011) and Haftbaradaran & Gao (2012) also demonstrated that the lithiation-induced large stresses can be mitigated due to the presence of interfacial sliding between electrodes and nearby current collectors. These results indicate that Si films with an appropriate island size can effectively prevent formation of microcracks and films delamination. Similar critical thickness effect was observed in our experiments reported in this thesis. Buckling features and fracture patterns of thicker a-Si film (95.2 and 108.7 nm respectively) were detected from optical microscope after first cycle (Figure 1.1). On the contrary, no fracture or buckling features of a 52.6 nm thin film was found (Figure 1.2) due to the presence of interfacial sliding between the Si electrode and the Cu current collector. Thus, to improve half-cell

performance especially for previous two approaches, carefully designed interfaces between Si electrodes with nearby materials are next challenge issues. As the results, it is essential to study the properties of a-Si/Cu or a-Si/C interfaces during cyclic intercalation.

Although the interfacial properties during lithiation and delithiation cycles have been estimated from DFT calculations (Stournara *et al.*, 2013) and a continuum model (Haftbaradaran *et al.*, 2012), direct experimental measurements are still needed to validate the results. Therefore, an experiment for measuring the interfacial properties between the a-Si thin film electrode and the Cu current collector has been performed. As shown in previous chapter, the interfacial sliding distance along with high precision thickness variation has been *in situ* measured via SALLI experiment. In this chapter, a mechanical model system named plate bending distribution sensor (PBDS) which incorporates substrate bending and interfacial sliding in its calibration, is developed to further extract the sliding characteristics of the interface between a film and a substrate from the SALII experimental data.

3.2   Formulation of Plate Bending Distribution Sensor (PBDS)

In this section, the plate bending distribution sensor (PBDS) is developed to further understand the sliding mechanism from the SALLI experimental data. Although the thin film stress of an electrode can be *in situ* measured by multi-beam optical stress sensor (MOSS), PBDS not only can detect the thin film stress but also provide the interfacial properties between a film and a substrate. During lithiation and delithiation cycles, a Si thin film is subjected to stress accumulation caused by huge volume expansion (Sethuraman *et al.*, 2010b) and also interfacial sliding (Soni *et al.*, 2011). The bending

50

moment induced by this thin film stress then leads to out-of-plane deflection of the substrate. By bridging the deformation calculated from PBDS and those obtained from SALLI experiments, the interfacial properties of a-SiLi$_x$//Cu interface during electro-chemical loads can be extracted quantitatively.

3.2.1 Substrate bending in the presence of interfacial sliding

Consider that the initial film residual stress is uniform σ_0 in the initial configuration within the observational window. Then, the interfacial shear stress can be approximately written as

$$\boldsymbol{\tau}(s_1, s_2) = \sigma_0 h_f \left\{ \delta(s_1)\mathbf{e}_1 + \delta(s_2)\mathbf{e}_2 \right\} = f_0 \left\{ \delta(s_1)\mathbf{e}_1 + \delta(s_2)\mathbf{e}_2 \right\}, \qquad (3.1)$$

where f_0 is the concentrated stress at the edge of the interface in the initial configuration and h_f is the thickness of a film. Note that according to Freund's calculation (2003), f_0 is applied within 1 μm^2 area at the edge of the a-SiLi$_x$//Cu interface.

As the electrode film is subjected to electro-chemical loads (Figure 3.1), the interfacial shear stress τ_s and thin film force $\sigma_f \cdot h_f$ in the presence of one slip zone are

$$\tau(\mathbf{s}) = \tau_s \left(H(\mathbf{s} - \ell_{es}) - H(\mathbf{s} - \ell_{es} - \ell_{is}) \right) + (\tau_s + f_s)\delta(\mathbf{s} - \ell_{es} - \ell_{is})$$
$$\sigma_f(\mathbf{s})h_f = \tau_s(\mathbf{s} - \ell_{es})\left(H(\mathbf{s} - \ell_{es}) - H(\mathbf{s} - \ell_{es} - \ell_{is}) \right) + (\tau_s \ell_{is} + f_s)H(\mathbf{s} - \ell_{es} - \ell_{is}). \qquad (3.2)$$

Here, $\delta(\cdot)$ and $H(\cdot)$ denote Dirac delta function and Heaviside step function respectively. The matrix $\mathbf{s}$ represent two basis vectors s_1 and s_2. ℓ_{es} is the edge sliding distance, ℓ_{is} the zone size of interfacial sliding, and f_s concentrated stress. If the concentrated stress f_s is greater than the critical value f_{scr}, then the slip front propagates (i.e., ℓ_{is} increases progressively). Otherwise, the slip front stops advancing. In this model,
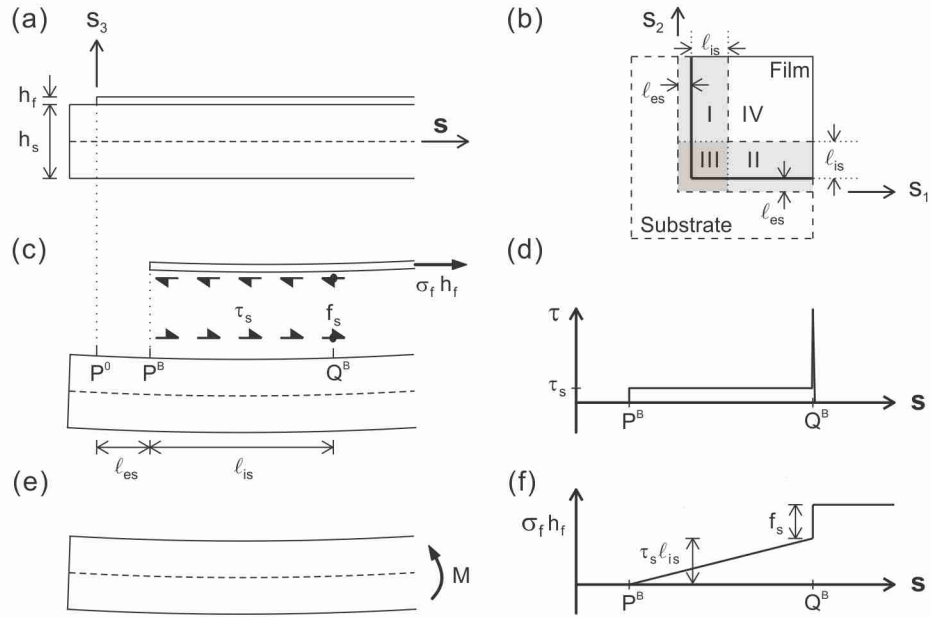
Figure 3.1 (a) Initial configuration of a thin film on substrate. (b) The configurations of the initial (dashed line) and current (solid line) Si film configurations in the top view. (c) The free body diagram of half of the sliding film. (d) Corresponding shear diagram. (e) The free body diagram of bending moment and thin film force diagram (f).

the substrate bending moment is only caused by lithiation and delithiation-induced thin film stress. Therefore, the thin film thickness, $h_f = \Delta h_{Si} + h_{Si}^0$, is contributed from the thickness of a Si film only without considering that of a SEI layer (h_{SEI}), where Δh_{Si} and h_{Si}^0 are the thickness variation and the initial thickness of a Si film respectively.

Then, the variation of the interfacial shear stress induced by electro-chemical loads relative to the initial configuration is expressed as

$$\Delta \boldsymbol{\tau}\left(s_{1}, s_{2}\right)=\Delta \tau_{1}\left(s_{1}\right)+\Delta \tau_{2}\left(s_{2}\right)$$

$$=\begin{cases}\left[\tau_{s}\left(H\left(s_{1}-\ell_{es}\right)-H\left(s_{1}-\ell_{es}-\ell_{is}\right)\right)+\left(\tau_{s}+f_{s}\right)\delta\left(s_{1}-\ell_{es}-\ell_{is}\right)-f_{0}\delta\left(s_{1}\right)\right]\mathbf{e}_{1} \\ \left[\tau_{s}\left(H\left(s_{2}-\ell_{es}\right)-H\left(s_{2}-\ell_{es}-\ell_{is}\right)\right)+\left(\tau_{s}+f_{s}\right)\delta\left(s_{2}-\ell_{es}-\ell_{is}\right)-f_{0}\delta\left(s_{2}\right)\right]\mathbf{e}_{2} \\ \Delta\tau^{I}\left(s_{1}\right)\mathbf{e}_{1}+\Delta\tau^{II}\left(s_{2}\right)\mathbf{e}_{2} \\ 0 \end{cases}$$ (3.3)

$$=\begin{cases}\Delta\tau^{I}\left(s_{1}\right)\mathbf{e}_{1}, & \text{for I,} \\ \Delta\tau^{II}\left(s_{2}\right)\mathbf{e}_{2}, & \text{for II,} \\ \Delta\tau^{I}\left(s_{1}\right)\mathbf{e}_{1}+\Delta\tau^{II}\left(s_{2}\right)\mathbf{e}_{2}, & \text{for III,} \\ 0, & \text{for IV,} \end{cases}$$

where four regions (Figure 3.1(b)) are defined as

I: $\left(s_{1}, s_{2}\right)\in\ 0\leq s_{1}\leq\ell_{es}+\ell_{is}\ $ and $\ \ell_{es}+\ell_{is}\leq s_{2}.$

II: $\left(s_{1}, s_{2}\right)\in\ \ell_{es}+\ell_{is}\leq s_{1}\ $ and $\ 0\leq s_{2}\leq\ell_{es}+\ell_{is}.$

III: $\left(s_{1}, s_{2}\right)\in\ 0\leq s_{1}\leq\ell_{es}+\ell_{is}\ $ and $\ 0\leq s_{2}\leq\ell_{es}+\ell_{is}.$

IV: $\left(s_{1}, s_{2}\right)\in\ \ell_{es}+\ell_{is}\leq s_{1}\ $ and $\ \ell_{es}+\ell_{is}\leq s_{2}.$

Next, the variation of thin film force is

$$\Delta\boldsymbol{\sigma}\left(s_{1}, s_{2}\right)h_{f}=\Delta f_{1}\left(s_{1}\right)\mathbf{e}_{1}+\Delta f_{2}\left(s_{2}\right)\mathbf{e}_{2}$$

$$=\begin{cases}\left[\tau_{s}\left(s_{1}-\ell_{es}\right)\left(H\left(s_{1}-\ell_{es}\right)-H\left(s_{1}-\ell_{es}-\ell_{is}\right)\right)+\left(\tau_{s}\ell_{is}+f_{s}\right)H\left(s_{1}-\ell_{es}-\ell_{is}\right)-f_{0}\right]\mathbf{e}_{1} \\ \left[\tau_{s}\left(s_{2}-\ell_{es}\right)\left(H\left(s_{2}-\ell_{es}\right)-H\left(s_{2}-\ell_{es}-\ell_{is}\right)\right)+\left(\tau_{s}\ell_{is}+f_{s}\right)H\left(s_{2}-\ell_{es}-\ell_{is}\right)-f_{0}\right]\mathbf{e}_{2} \\ \Delta f^{I}\left(s_{1}\right)\mathbf{e}_{1}+\Delta f^{II}\left(s_{2}\right)\mathbf{e}_{2} \\ \left[\tau_{s}\ell_{is}+f_{s}-f_{0}\right]\mathbf{e}_{1}+\left[\tau_{s}\ell_{is}+f_{s}-f_{0}\right]\mathbf{e}_{2} \end{cases}$$ (3.4)

$$=\begin{cases}\Delta f^{I}\left(s_{1}\right)\mathbf{e}_{1}, & \text{for I.} \\ \Delta f^{II}\left(s_{2}\right)\mathbf{e}_{2}, & \text{for II.} \\ \Delta f^{I}\left(s_{1}\right)\mathbf{e}_{1}+\Delta f^{II}\left(s_{2}\right)\mathbf{e}_{2}, & \text{for III.} \\ \left[\tau_{s}\ell_{is}+f_{s}-f_{0}\right]\mathbf{e}_{1}+\left[\tau_{s}\ell_{is}+f_{s}-f_{0}\right]\mathbf{e}_{2}, & \text{for IV.} \end{cases}$$

Therefore, the bending moment can be derived in the following form

$$\Delta\mathbf{M}\left(s_{1}, s_{2}\right)=\Delta M_{1}\left(s_{2}\right)\mathbf{e}_{1}+\Delta M_{2}\left(s_{1}\right)\mathbf{e}_{2}$$
$$=\Delta f_{2}\left(s_{2}\right)\left(h_{f}/2+h_{s}/2\right)\mathbf{e}_{1}-\Delta f_{1}\left(s_{1}\right)\left(h_{f}/2+h_{s}/2\right)\mathbf{e}_{2},$$ (3.5)

where h_s is the thickness of a substrate. Finally, the out-of-plane deflection $u_3(\mathbf{s})$ of the substrate induced by this bending moment is estimated by finite element analysis (section 3.3).

3.2.2 PBDS for experimental data

To further extract sliding properties, we apply PBDS to the SALLI experimental data. From the evolution of the sliding distance ℓ_{es} in Figure 2.17, the interfacial debonding caused by lithium segregation (Stournara *et al.*, 2013) occurred at the early stage of the first cycle. This edge intercalation induced the sliding distance suddenly jumping from zero to 6.1 μm in stage A and indicates that one slip front unstably jumpped from zero to ℓ_{is}^{A*}. The free body diagram and the diagram of this slip-zone shear force are shown in Figure 3.2(b). The concentrated shear stress f_s^A is smaller than the critical value f_{scr}. Therefore, the slip zone does not propagate in this stage. Then, the steady state growth of this slip front (ℓ_{is}^B in Figure 3.2(c)) from ℓ_{is}^{A*} to ℓ_{is}^{B*} is due to successive edge intercalations. This leads to unexpected contraction (up to 200 μm) of a 50 nm thick Si film in stage B, that appears to be driven by the residual tensile stress generated during the manufacturing process of the film. Note that the slip front prorogates progressively implying that the concentrated shear stress of the slip always reaches f_{scr}.

In stage C1 (Figure 3.2(d)), the film expands because of the massive volume increase in Si during lithiation. Since the sliding direction changes, a new slip zone ℓ_{is}^{C1} with reversed shear stress occurs. Again, the slip front with size ℓ_{is}^{B*} stops advancing owing to its concentrated stress f_s^B smaller than f_{scr}. Finally, at the end of the first cycle,
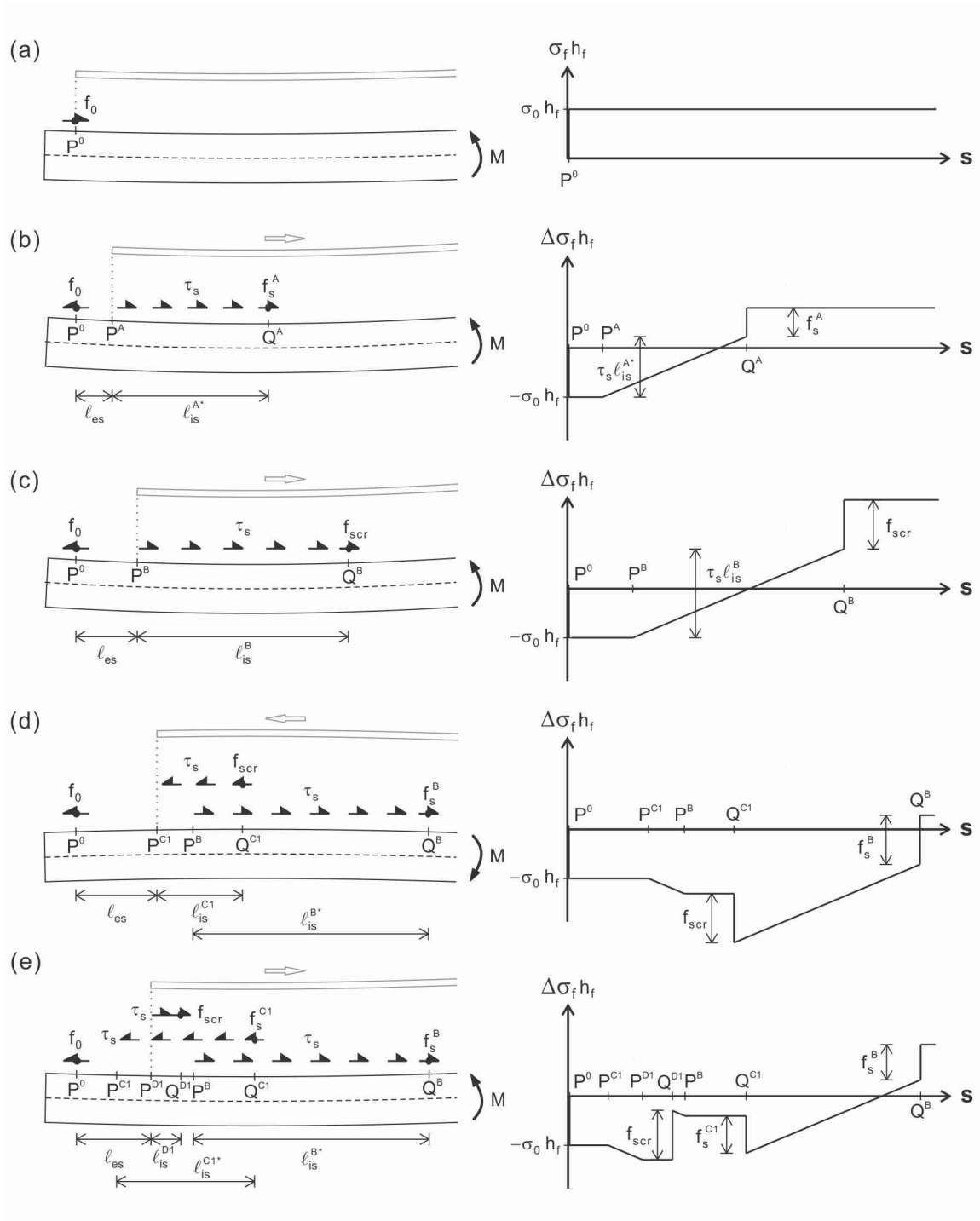
Figure 3.2 Free body diagrams (first column) and the diagrams of the corresponding shear force (second column) for each stage: (a) initial configuration, (b) stage A, (c) stage B, (d) stage C1, and (e) stage D1. A thin film is plotted in gray solid line and its direction of motion is shown by a gray arrow. Notation P and Q represent the position of the film edge and that of the slip front. The character in the superscript denotes the parameter formed in which stage, and ℓ_{is}^* indicates the final size of the slip zone.

55

a new slip zone ℓ_{is}^{D1} opens and drives the film to shrink during delithiation (stage D1; Figure 3.2(e)).

According to Figure 2.17, the latter two motions, i.e., expansion and shrinkage in stage C and D respectively, are repeatable in the first two cycles. Analogy to the mechanisms in stage C1 and D1, two more slide zones should be added when analyzing the second cycle. Generally speaking, while the direction of the film edge motion changes, one new slide zone occurs with the concentrated shear stress reaching the critical value f_{scr}. In the meanwhile, the previous slip front stops propagating and its concentrated shear stress should be smaller than f_{scr}.

Similarly to equation (3.5), the variation of the substrate bending moment induced by the change of the thin film force in different stages can be derived – multiplying the shear forces by $\left(h_f/2 + h_s/2\right)$. Finally, the deflection $u_3(\mathbf{s})$ due to this bending moment can be calculated via finite element analysis.

3.3   Algorithms and Finite Element Model for PBDS

To simplify the analysis, the out-of-plane displacement field due to the presence of one slide zone is first introduced. Then, calculate the total deflection by superposition of slide zones, e.g. superposition of slip B, C1 and D1 to estimate the displacement field at the time during stage D1; or superposition of slip B, C1, D1, and C2 to assess the deflection at the time during stage C2 in the second cycle.

Consider the displacement field $\bar{u}_3(s_1, s_2, \xi)$ of the substrate induced by a set of torques $\bar{\mathbf{M}} = 1 \cdot (-\mathbf{e}_1) + 1 \cdot \mathbf{e}_2$ applied at a distance ξ from both edges of Si film, which has
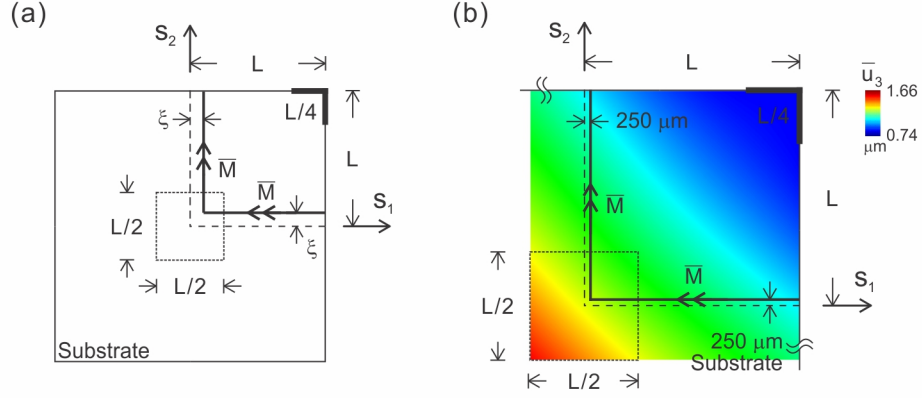
Figure 3.3 (a) Schematic figure of the finite element analysis model. (b) Out-of-plane deformation field from ABAQUS analysis while the sliding distance $\xi = 250 \; \mu m$.

unit magnitudes per unit length along the basis directions. The displacement field was analyzed from finite element method. In the model (Figure 3.3), the substrate with length $L = 8980 \; \mu m$ and thickness $h_{sub} = 250.2 \; \mu m$ (a 200 nm Cu film on a 250 μm quartz wafer; Figure 2.12) was simulated exclusively by 8-node thick shell elements via ABAQUS software. The effective Young's modulus and Poisson ratio of the substrate were taken as 72.02 GPa and 0.17 respectively. To minimize the effect from the boundary conditions, only the right top corner with length $L/4$ was fixed and the displacement field within the center $\pm L/4$ region (totally 8100 elements while $\xi = 0$) were taken for further calculation.

For an analysis of linear elastic materials, the displacement distribution (in the role of a Green's function) of the substrate induced by the varying bending moment distribution $\Delta \mathbf{M}(s_1, s_2)$ in equation (3.5) is given as

$$
\begin{aligned}
u_{bend}^n (s_1, s_2) &= \int_{\ell_{es}}^{\ell_{es}+\ell_{is}} \bar{u}_3(s_1, s_2, \xi) \cdot T_s \cdot \left(h_f/2 + h_s/2 \right) / \ell_{is} \; d\xi + \\
&\quad \bar{u}_3(s_1, s_2, \ell_{es} + \ell_{is}) \cdot f_s \cdot \left(h_f/2 + h_s/2 \right) - \bar{u}_3(s_1, s_2, 0) \cdot f_0 \cdot \left(h_f/2 + h_s/2 \right) \quad (3.6) \\
&= u_3^{(1)}(s_1, s_2) + u_3^{(2)}(s_1, s_2) - u_3^{(0)}(s_1, s_2).
\end{aligned}
$$

57
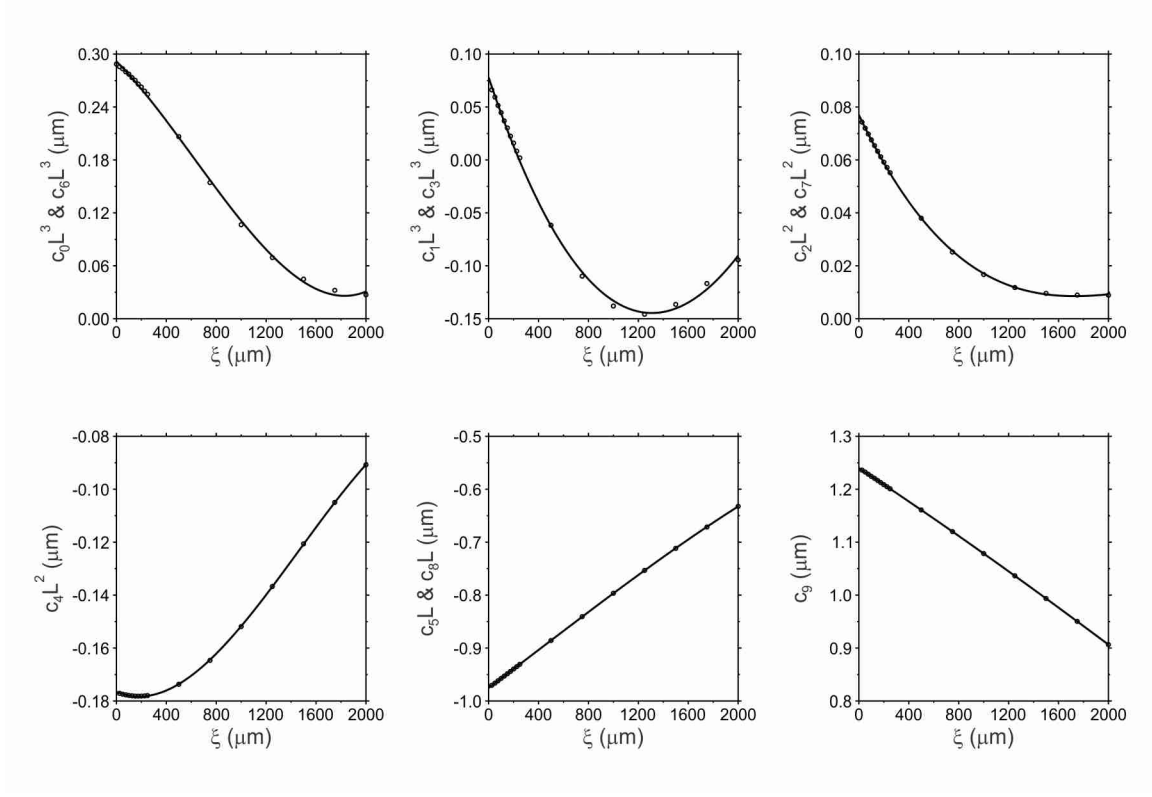
Figure 3.4 The polynomial coefficients $c_i(\xi)$ for expressing displacement field $\bar{u}_3(s_1, s_2, \xi)$ obtained from finite element analysis.

where $T_s = \tau_s \ell_{is}$ is the interfacial shear force. The $\bar{u}_3(s_1, s_2, \xi)$ field is expressed as a polynomial of degree 10 as

$$\begin{aligned}
\bar{u}_3(s_1, s_2, \xi) &= c_0(\xi)s_1^3 + c_1(\xi)s_1^2 s_2 + c_2(\xi)s_1^2 + c_3(\xi)s_1 s_2^2 + c_4(\xi)s_1 s_2 + \\
&\quad c_5(\xi)s_1 + c_6(\xi)s_2^3 + c_7(\xi)s_2^2 + c_8(\xi)s_2 + c_9(\xi) \\
&= \sum_{i=0}^{9} c_i(\xi)s_1^{p(i)} s_2^{q(i)},
\end{aligned} \tag{3.7}$$

and these coefficients can also be written as series solutions,

$$c_i(\xi) = \sum_{j=0}^{3} d_{ij}\xi^j = d_{i0} + d_{i1}\xi + d_{i2}\xi^2 + d_{i3}\xi^3. \tag{3.8}$$

The coefficients $c_i(\xi)$ are displayed as functions of ξ in Figure 3.4. Then, the displacement distribution $u_3^{(0)}(s_1,s_2)$, $u_3^{(1)}(s_1,s_2)$ and $u_3^{(2)}(s_1,s_2)$ can be further reduced as follows

$$
\begin{aligned}
u_3^{(0)}(s_1,s_2) &= \bar{u}_3(s_1,s_2,0)\cdot f_0 \cdot \left(h_f/2+h_s/2\right) = \left(h_f/2+h_s/2\right)\sum_{i=0}^{9} f_0 d_{i0} s_1^{\,p(i)} s_2^{\,q(i)} \\
&= \left(h_f/2+h_s/2\right)\sum_{i=0}^{9} \alpha_i^{(0)} s_1^{\,p(i)} s_2^{\,q(i)}.
\end{aligned}
\tag{3.9}
$$

Here, h_f is the initial thickness of a silicon film, h_{Si}^0, and $\alpha_i^{(0)} = f_0 d_{i0}$;

$$
\begin{aligned}
u_3^{(1)}(s_1,s_2) &= \int_{\ell_{es}}^{\ell_{es}+\ell_{is}} \bar{u}_3(s_1,s_2,\xi)\cdot T_s \cdot \left(h_f/2+h_s/2\right)/\ell_{is}\ d\xi \\
&= \left(h_f/2+h_s/2\right)\int_{\ell_{es}}^{\ell_{es}+\ell_{is}} \sum_{i=0}^{9}\sum_{j=0}^{3} T_s d_{ij}\xi^j\, s_1^{\,p(i)} s_2^{\,q(i)}/\ell_{is}\ d\xi \\
&= \left(h_f/2+h_s/2\right)\sum_{i=0}^{9}\left(\sum_{j=0}^{3} T_s d_{ij}/\ell_{is}\right) s_1^{\,p(i)} s_2^{\,q(i)}\int_{\ell_{es}}^{\ell_{es}+\ell_{is}} \xi^j\ d\xi \\
&= \left(h_f/2+h_s/2\right)\sum_{i=0}^{9}\left(\sum_{j=0}^{3} T_s d_{ij}/\ell_{is}\right)\left[\frac{\left(\ell_{es}+\ell_{is}\right)^{j+1}-\ell_{es}^{\,j+1}}{j+1}\right] s_1^{\,p(i)} s_2^{\,q(i)} \\
&= \left(h_f/2+h_s/2\right)\sum_{i=0}^{9} \alpha_i^{(1)} s_1^{\,p(i)} s_2^{\,q(i)},
\end{aligned}
\tag{3.10}
$$

where $\displaystyle \alpha_i^{(1)} = \sum_{j=0}^{3}\frac{T_s d_{ij}}{\ell_{is}}\left[\frac{\left(\ell_{es}+\ell_{is}\right)^{j+1}-\ell_{es}^{\,j+1}}{j+1}\right]$;

$$
\begin{aligned}
u_3^{(2)}(s_1,s_2) &= \bar{u}_3(s_1,s_2,\ell_{es}+\ell_{is})\cdot f_s \cdot \left(h_f/2+h_s/2\right) \\
&= \left(h_f/2+h_s/2\right)\sum_{i=0}^{9}\sum_{j=0}^{3} f_s d_{ij}\left(\ell_{es}+\ell_{is}\right)^j s_1^{\,p(i)} s_2^{\,q(i)} \\
&= \left(h_f/2+h_s/2\right)\sum_{i=0}^{9} \alpha_i^{(2)} s_1^{\,p(i)} s_2^{\,q(i)},
\end{aligned}
\tag{3.11}
$$

in which $\displaystyle \alpha_i^{(2)} = \sum_{j=0}^{3} f_s d_{ij}\left(\ell_{es}+\ell_{is}\right)^j$.

Finally, for different stages shown in Figure 3.2, the substrate displacement induced by the change of thin film force can be calculated by the superposition of substrate displacements in sequence.

3.4 Optimization Scheme

Based on the above scenarios, an optimization scheme is developed to estimate the materials and mechanical properties of the Si electrode film on Cu current collector from the SALLI experimental data through minimizing the error functional

$$
\begin{aligned}
E\left(\Delta h_{Si}, h_{SEI}, a, b, c, \mathbf{v}; \mathbf{x}\right) \\
= \int_{S_{Si}} \left| u_{3Si}^{m}\left(\mathbf{x}\right) - u_{3Si}^{n}\left(\mathbf{v}; \mathbf{x}\right) \right|^{2} dS + \int_{S_{Cu}} \left| u_{3Cu}^{m}\left(\mathbf{x}\right) - u_{3Cu}^{n}\left(\mathbf{v}; \mathbf{x}\right) \right|^{2} dS.
\end{aligned}
\tag{3.12}
$$

Here, the superscript m and n denote the displacement field obtained from experimental measurement and numerical calculation respectively. Also,

$$
\begin{cases}
u_{3Si}^{n}\left(\mathbf{v}; x_1, x_2\right) = ax_1 + bx_2 + c + h_{Si} + h_{SEI} + u_{bend}^{n}\left(\mathbf{v}; x_1, x_2\right) \\
u_{3Cu}^{n}\left(\mathbf{v}; x_1, x_2\right) = ax_1 + bx_2 + c + u_{bend}^{n}\left(\mathbf{v}; x_1, x_2\right)
\end{cases},
\tag{3.13}
$$

where $ax_1 + bx_2 + c$ depicts a tilt plane used in noise removal technique (section 2.4.3). The input variables to determine $u_{bend}^{n}\left(\mathbf{v}; x_1, x_2\right)$ are the sliding displacements ℓ_{es} measured from the SALLI experiment. The floating variables of the error functional (equation (3.12)) are Δh_{Si}, h_{SEI}, a, b, c, and an array of floating parameters, $\mathbf{v} = f_0, T_s, f_{scr}, f_s^{A}, f_s^{B}, f_s^{C1}, f_s^{D1}, f_s^{C2}, \ell_{is}^{B}, \ell_{is}^{C1}, \ell_{is}^{D1}, \ell_{is}^{C2}, \ell_{is}^{D2}$. The latter is related to the sliding zones at different stages (Figure 3.2). Note that the global parameter f_0 is evaluated from minimizing the total error norm of the whole two cycles. Other local variables are estimated by optimizing the functional $E\left(\Delta h_{Si}, h_{SEI}, a, b, c, \mathbf{v}; \mathbf{x}\right)$ for each
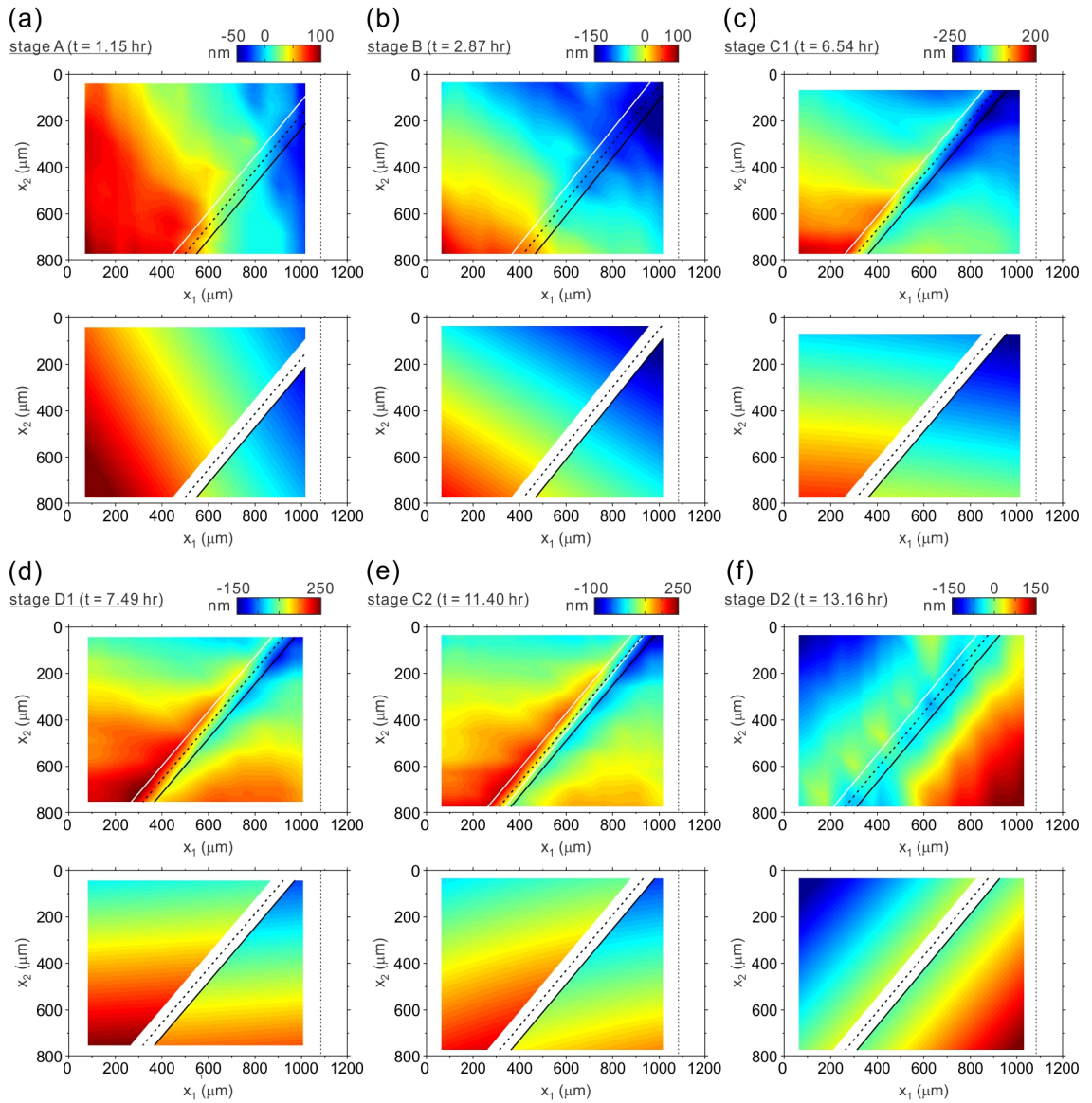
Figure 3.5 Contour plots in the 1st and 3rd rows are the thickness variation obtained from experiment and those in the 2nd and 4th rows are calculated from simulation. Selected figures are from (a) stage A, (b) stage B, (c) stage C1, (d) stage D1, (e) stage C2, and (f) stage D2.

time step. While the slip zone reaches the final length, i.e., at the end of each stage, the

local variable ℓ_{is}^{A*}, ℓ_{is}^{B*}, ℓ_{is}^{C1*}, ℓ_{is}^{D1*}, ℓ_{is}^{C2*}, and ℓ_{is}^{D2*} can be assessed.

To bridge the deflection obtained from the experimental measurement and numerical calculation, consider the coordinate transformation between the coordinate used in the observation window (x_1, x_2) (Figure 2.8) and that adopted in the simulation model (s_1, s_2) (Figure 3.1(b)) via following equations,

$$s_i = s_i^0 + A_{ij}x_j,\qquad(3.14)$$

where $i, j = 1$ or 2 and $\begin{bmatrix} A_{ij} \end{bmatrix} = \begin{bmatrix} \cos\theta & \sin\theta \\ -\sin\theta & \cos\theta \end{bmatrix}$. Here, s_i^0 and θ are estimated from measurements. The optimization results after applying the scheme to the SALLI experiment are shown in the contour plots (Figure 3.5) for all stages during the first two cycles. From the figure, the thickness variations determined from simulation (2nd and 4th rows) properly capture those measured from experiment (1st and 3rd rows).

3.5   Results and Discussions

Interpreting the SALLI experimental data with a mechanics-based model (PBDS) allows us to estimate interfacial properties (i.e., shear strength and critical energy release rate for debonding). These quantitative results are summarized in this section. Note that the sizes of the slide zones are assumed to increase progressively since the measured sliding distances ℓ_{es} (Figure 2.17) expanded and shrank gradually. In addition, the constraint adopted for the thickness of the Si film is $0 \le \Delta h_{Si} \le 400$ nm $\approx 8h_{si}^0$. Since the SEI layers are formed during the potential plateau region (Chan *et al.*, 2009; Zheng *et al.*, 2006), 2.01 hour in the first cycle (Figure 2.17), the constraint for h_{SEI} during this growing

62
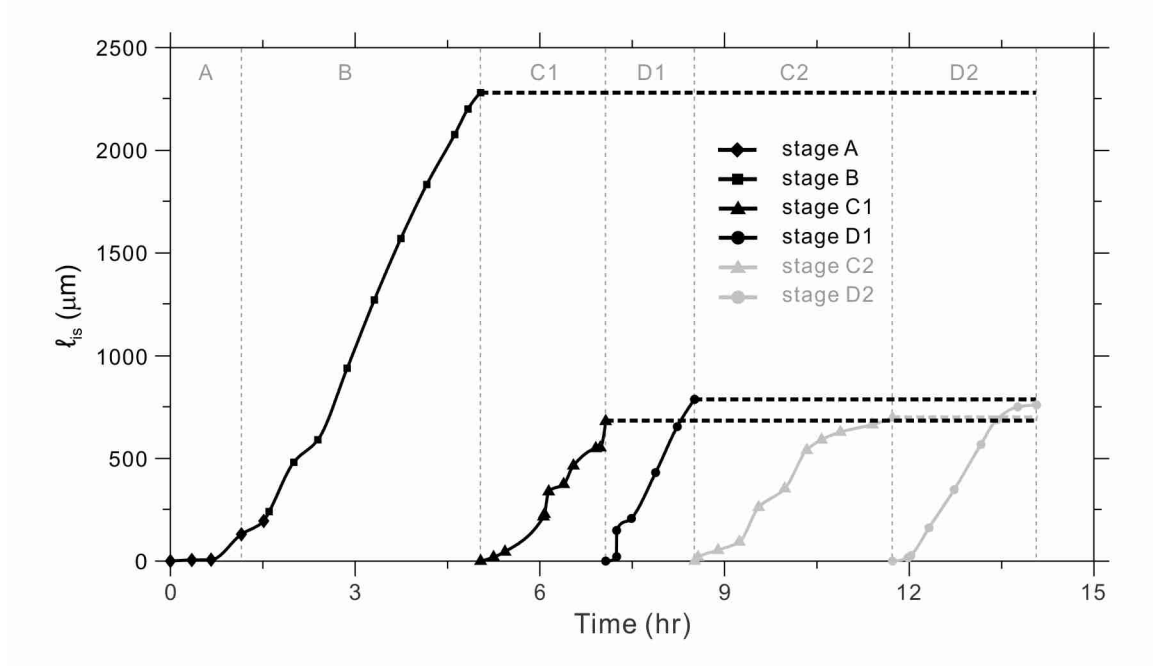
Figure 3.6 The evolution of the zone sizes for interfacial sliding between a 50 nm thin a-Si film and a 200 nm Cu current collector for the first two cycles.

period is $0 \leq h_{SEI}$ in the first two hours. After that, it is constrained as $0 \leq h_{SEI} \leq 35$ nm

(175% of h_{SEI} obtained at the end of the first two hours) for the rest of cycles.

Evolution of the slip zone size is illustrated in Figure 3.6. As mentioned previously, the first slip jumps from 0 to $\ell_{is}^{A*} = 130.41$ μm suddenly and the slip front (ℓ_{is}^{B}) further propagates after 1.52 hour (stage B). In this stage, the slip front advances tremendously and reaches the maximum value $\ell_{is}^{B*} = 2280.42$ μm due to relaxation of the residual tensile stress. Then, another slide zone caused by massive bulk lithiation forms gradually ($\ell_{is}^{C1} = 0 - 681.01$ μm) during stage C1. At the end of the first cycle, the film shrinks again because of Li removal. Therefore, the slip front with size ℓ_{is}^{D1} occurs and attains $\ell_{is}^{D1*} = 787.15$ μm. Here, the final zone size of slip front D1 (ℓ_{is}^{D1*}) surpasses that

63

of slip front C1 (ℓ_{is}^{C1*}). It implies that the film not only recovers to the site before expansion caused in stage C1, but also contracts more. In other words, the location of the film edge shrinks even further comparing to that at the end of the stage B. This result is consistent with the sliding distance measured from SALLI experiment (Figure 2.17). As expected, the cycling effect of slip fronts C1 and D1 can be observed in the second cycle. The slip fronts C1 and C2 have similar final size (ℓ_{is}^{C1*} = 681.01 μm and ℓ_{is}^{C2*} = 697.62 μm); also, D1 (ℓ_{is}^{D1*} = 787.15 μm) and D2 (ℓ_{is}^{D2*} = 759.97 μm).

The thickness variations of the a-Si film Δh_{Si} and the SEI layer Δh_{SEI} are depicted in Figure 3.7, where Δh_{Si} is estimated by area-average of the whole Si domain inside observation window and $\Delta h_{SEI} = h_{SEI}$ since the initial thickness of the layer is zero. From the figure, the Si film increases slightly till 13.31 nm at the end of the stage A (1.61 hour) and then Δh_{Si} decreases to 3.97 nm during stage B. This shrinkage is due to the formation of SEI on the Cu current collector. The SEI formation on Cu at this potential range (0.47 − 0.25 V) was also measured by the *in situ* AFM experiment (Tokranov *et al.*, 2014). At the end of stage B and during stage C1, Δh_{Si} expands rapidly because of massive bulk lithiation. Similar phenomena observes during stage C2. An interesting discovery is that Δh_{Si} contracts (at 6.54 to 7.07 hour) before the end of lithiation. This is because the volume expansion due to Si insertion almost saturates within this time period, but in the meanwhile the sliding distance (Figure 2.17) still increases progressively (almost linearly). Therefore, all the volume expansion is contributed by in-plane dilation rather than out-of-plane extension. Finally, Δh_{Si} tries to recover its original thickness during delithiation (stage D1 and D2), but 19.26 nm residual thickness remains at the end of the
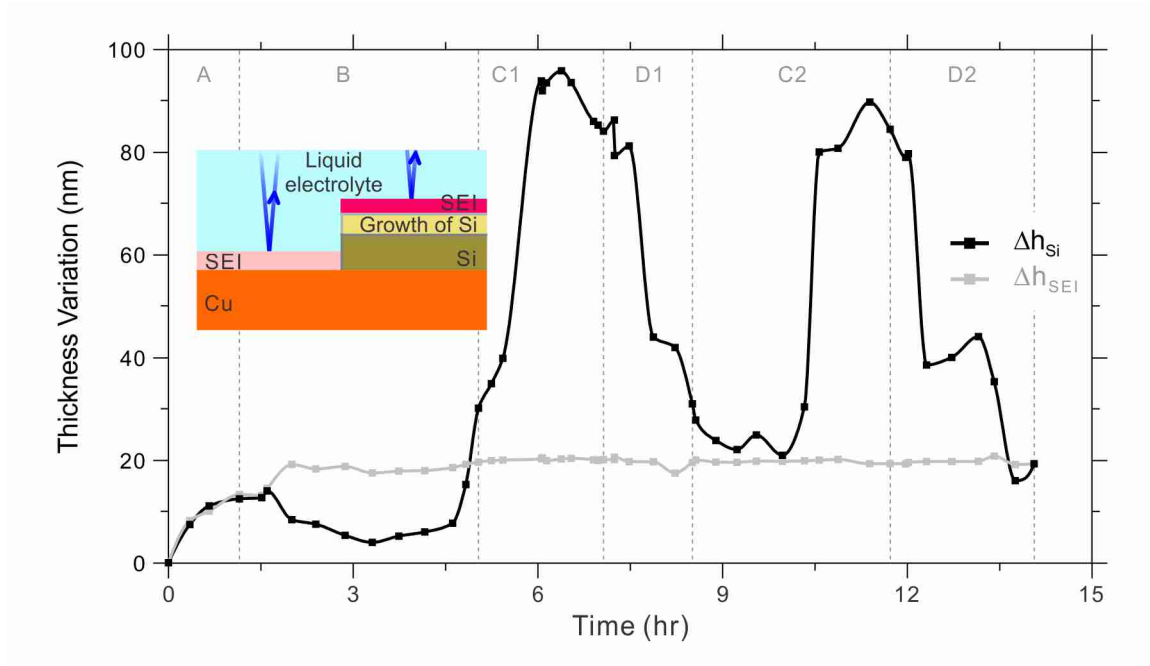
Figure 3.7 The relative thickness variations of the a-Si film and the SEI layer on top of Cu. Inset: A schematic shows the measuring spots and indicates that the thickness measured from SALLI is the relative thickness on top of the Cu film.

second cycle. This indicates that partial Si electrode cannot participate further lithiation anymore. This irreversible thickness is consistent with that measured in the *in situ* AFM study (Tokranov *et al.*, 2014).

Through the PBDS model system, the thickness variation measured by SALLI can be decomposed into the deformation of the Si film and the growth of SEI layer. The SEI layer forms before 2.01 hour, the beginning of stage B, and then reaches steady state with 19.16 nm thick on top of the copper current collector (Figure 3.7). The corresponding potential is 0.47 V which is close to the potential plateau 0.51 V as shown in Figure 3.8. The SEI thickness was also measured as 20 nm on Si-edge island film by *in situ* AFM (Tokranov *et al.*, 2014) and 20 nm on TiN electrodes using spectroscopic ellipsometry (McArthur *et al.*, 2012). It is well established that battery properties, such as coulombic

efficiency, energy efficiency, rate performance, capacity retention, and durability are highly dependent on SEI chemical, mechanical, and transport properties (Shi *et al.*, 2012; Verma *et al.*, 2010; Vetter *et al.*, 2005). However, the SEI typically is only a few nano meters thick, consisting of both dense inorganic and amorphous organic materials, and it is very difficult to characterize the properties. Thus our ability to monitor SEI formation with SALLI and PBDS is critically important. A detailed study of bubble-gas generation cause by SEI formation will be investigated in the next chapter.

In addition to the thickness variation results, these SALLI experimental measurements can also estimate the thin film stress $\sigma_f(\mathbf{s})$ via PBDS to determine curvature *in situ*. As derived in equation (3.4), the stress distribution obtained from this technique has spatial resolution. To correlate the results with those acquired from MOSS (Sethuraman *et al.*, 2010a; Sethuraman *et al.*, 2010b; Soni *et al.*, 2011), only thin film stress in the bulk region is plotted in Figure 3.8.

As expected, large stress variations (1.09 − -0.23 GPa) are observed during lithiation and delithiation cycles because of the huge volume changes of the a-Si film. While the insertion of lithium into the a-Si thin film causes volume expansion, the film is under compression (from 0.74 to -0.20 GPa in stage C1; from 0.45 to -0.23 GPa in stage C2) due to the constraint from the Cu substrate. On the other hand, this compressive stress is relaxed as the Si contracts and leads to a tensile regime relatively quickly (0.63 GPa at the end of stage D1; 0.73 GPa for stage D2) during Li removal. If the stress eventually becomes large enough to induce tensile flow, it may damage the bond network in the film, lower the strength of Si, and then cause the formation of microcracks (Xiao *et al.*, 2011).
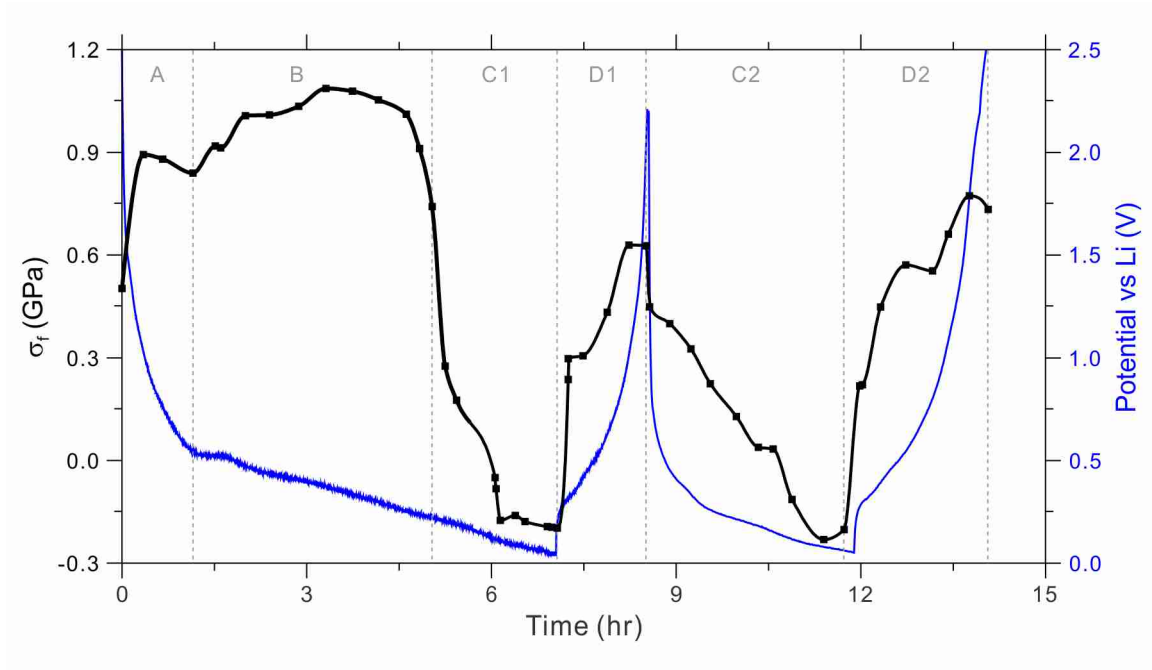
Figure 3.8 The *in situ* stress data of a 50 nm Si thin film along with potential history for the first two cycles.

The stresses measured in this experiment has similar range of that reported from previous investigations with continuous thin films by Sethuraman *et al.* (2010a) and Soni *et al.* (2011). Moreover, the tensile stresses in stage B gradually increase rather than decreasing to compression during the lithiation cycle. It is because of the shrinkage of the Δh_{Si} due to the SEI formation on the Cu region (Figure 3.7). The interfacial sliding which occurs in other stages accommodates stress generation and reduces the maximum compressive and tensile stresses significantly. Especially, the stress distribution in stage C2 has similar evolution (partially elastic response) as that of a 17 μm patterned Si film for the 2nd cycle (Soni *et al.*, 2011). Here, the initial thin film stress $\sigma_0 = 0.502$ GPa is calculated from the global parameter f_0 (equation (3.1)) obtained from the optimization of the total error functional (equation (3.12)).
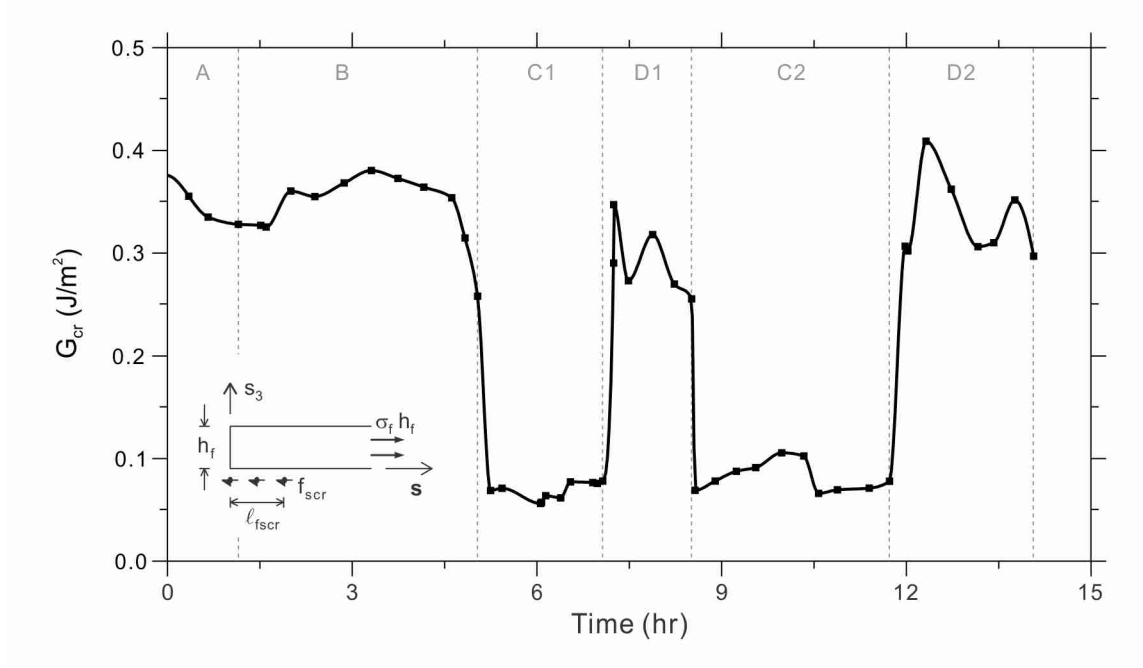
Figure 3.9 The critical energy release rate for debonding between a-SiLi$_x$//Cu interface. Inset: a free body diagram of a thin film with the concentrated stress at the edge area.

These SALLI measurements also provide estimates of the critical energy release rate, as shown in Figure 3.9. The energy dissipated during the interfacial sliding per unit of newly created slip zone area can be calculated by

$$G_{cr} = \frac{\left(1-v_f^2\right)\left(\sigma_{fcr}h_f\right)^2}{2h_fE_f} = \frac{\left(1-v_f^2\right)\left(f_{scr}\times\ell_{fscr}\right)^2}{2h_fE_f},$$ (3.15)

where the thickness of the film $h_f = h_{Si}^0 + \Delta h_{Si}$ as described in section 3.2.1, the Poisson ration of the Si film $v_f = 0.22$, and σ_{fcr} is the critical thin film stress (Freund & Suresh, 2003; Yu *et al.*, 2001). Note that Young's modulus of the Si film are expressed as $E_f = 80\ \text{GPa}\times F_{lithation}$, where 80 GPa is the modulus of a-Si film (Freund & Suresh, 2003) and $F_{lithation}$ is the linear interpolation factor due to stage of charge, e.g. $F_{lithation} = 0.5$

68

(Shenoy *et al.*, 2010) for fully-lithiated Si and $F_{lithiation} = 1$ for fresh Si. The critical concentrated stress f_{scr} is applied on the cross-section area with unit length $\ell_{fscr} = 1$ μm as depicted in the inset of Figure 3.9. The strength of the material changes due to lithiation and delithiation cycles. These measurements show that the concentrated shear strength is 59.9 – 64.0 MPa during lithiation cycles, and 29.9 – 30.5 MPa during delithiation processes. The critical energy release rate during interfacial sliding is estimated as 0.075 J/m^2 for a receding shear crack front and 0.34 J/m^2 for a growing shear crack front at the edge of the sliding zone. Here, G_{cr} depends on the phase of the loading (i.e. growth by compression or tension and the Si stage of charge) and governs the growth of the interfacial cracks. The present study provides an essential understanding of the role of lithiation at the a-SiLi$_x$//Cu interface on sliding and crack growth, which can be used to develop optimal designs for nanostructured Si electrodes.

In PBDS model system, the interfacial shear stress τ_s can be obtained from the interfacial shear forces. While minimizing the error functional of out-of-plane displacement induced by substrate bending moments (equation (3.12)), shear forces T_s composed of the product of τ_s times ℓ_{is} (equation (3.2)) are determined. Then, the interfacial shear stress $\tau_s = T_s / \ell_{is}$ is estimated and shown in Figure 3.10. From the experimental results, τ_s is significantly larger at the beginning of each slip zone occurs, especially for the zone initiated in stage A. This means that the strength of the material is stronger and the crack (sliding zone) is hard to advance at the early stage of each zone. As Li segregates the interface during lithiation cycles, the strengths of the interface
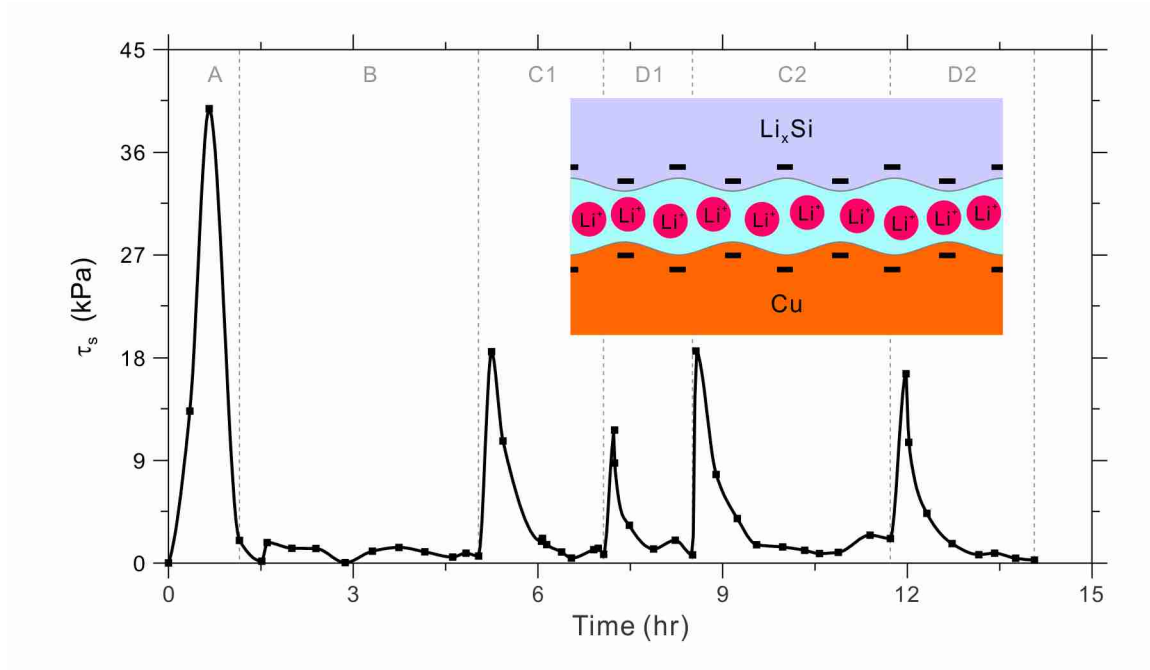
Figure 3.10 The interfacial shear strength at a-SiLi$_x$//Cu during the first two cycles. Inset: a schematic of the interface segregated by electro-chemically active lithium-ion liquid.

become weaker. Hence, the maximum interfacial shear stress deceases from 39.82 kPa in stage A to 18.53 kPa in stage C1, then finally to 11.65 kPa in stage D1.

A remarkable discovery is that the sliding resistance of the actively segregating lithium between a-SiLi$_x$//Cu interface is measured only 1.15 kPa. It is ten thousand times smaller than the flow stress of an inactive Li segregation layer estimated by DFT calculation (Stournara *et al.*, 2013). This is believed to be due to electro-chemically active lithium-ion segregation process (inset in Figure 3.10) that allows slip processes of hopping through a series of meta-stable atomic configurations. Similar lubrication phenomena with flow stresses of the same order have been observed in charged polymers (Raviv *et al.*, 2003) and an ionic-liquid layered confined between mica surfaces (Perkin *et al.*, 2010). This discovery shows that the 52.6 nm Si thin film electrode can easily slide

and has low friction between the interface. It substantially relaxes the thin film stress and prevents fracture.

It is believed that the LIBs made by the continuous Si thin film with this low interfacial shear strength (ISS) can maximize the Li capacity and cycle life. The present study provides an essential understanding of the role of lithiation at the a-SiLi$_x$//Cu interface on sliding and crack growth, which can be used to develop optimal designs for nanostructured Si electrodes.

Chapter 4.

IN SITU OBSERVATION AND MODELING OF THE LI-ION BATTERY CELL DEFORMATION

4.1   Introduction

Lithium-ion batteries (LIBs) are the technology of choice for future plug-in hybrid electric vehicles (PHEV) due to its high energy density, lightweight design, low self-discharge rate, no pollution, and long cell life (Tarascon & Armand, 2001). Improving LIB efficiency and extending cell life are current essential needs for the development of hybrid and electric vehicles. There are a range of phenomena limiting battery life, e.g., electrode degradation, failure of the binder, corrosion in current collectors, metallic Li plating, and solid electrolyte interphase (SEI) layers build-up on active electrode surfaces (Vetter *et al.*, 2005). It is well known that most of SEI layers, as a result of electrolytes decomposition, form on negative electrodes in the initial cycle. This formation process generates a certain amount of gases as by-products (depending on the compounds of the electrolyte; Goers *et al.*, 2004; Verma *et al.*, 2010). Gases buildup on subsequent cycles due to formation of new SEI layers on freshly exposed anode owing to particle fracture is considered to be minimal (Kim *et al.*, 2011), but still exists and can be problematic. Especially for large format pouch cells used in PHEV, a critical life-limiting factor is

accumulation and evolution of these gases. Since the cells tend to swell due to gas generation, large format pouch cells can have highly inhomogeneous current distribution. This inhomogeneity can cause various failure mechanisms such as overcharging or lithium deposition (Arora *et al.*, 1999; Kostecki *et al.*, 2006). Besides, the pressure of the cells increases while the cells are stored at high temperature and high state of charge (Broussely *et al.*, 2005). This continuously increasing pressure may cause safety issues and lead to cell degradation. Another main concern for pouch cells is that electrode particles can easily lose contact (particles to particles, particles to current collectors), since there is no strong adhesive between layers of electrode/separator assembly. This electrical disconnection becomes more severe and results in significant capacity fading and internal resistance increasing (Vetter *et al.*, 2005), while gas bubbles block Li-ion diffusion due to gases evolution and migration during cycling.

A few groups have studied the impact of compressing pressure on both material structures and battery performances. It has found that cell stack pressure limited the porosity of the anode in the prismatic cell and improved the contact issue resulting in lower resistance and increasing capacity. If the cell was under lower stack pressure, the anode exhibited more swelling during cycling and resulted in higher porosity of the electrode. The increase porosity reduced the integrity of the electrical conduction network causing many graphite particles to become isolated or less accessible (Rubino *et al.*, 2001). Ponnappan & Ravigururajan (2004) also reported that 'contact thermal resistance' was highly dependent on stack pressure applied on Li-ion battery components. However, these experiments did not consider the evolution of gases which may increase porosity of

the electrodes, since the amount of gases accumulated in these tested cells was negligible unlike large format pouch cells for PHEV.

Recently, although a few research group applied mechanical loadings on the pouch PHEV cells (i.e., indentation, bulking, and four-point bending tests), their studies only focused on evaluating mechanical integrity of the cells in different abuse conditions (Ali *et al.*, 2013; Lai *et al.*, 2014; Sahraei *et al.*, 2012). Therefore, to understand the degradation mechanisms of the large format pouch cells, we perform two sets of *in situ* experimental tests and develop a mechanical model to explain the internal contact mechanism and its relationship with interface bubble-gas evolution. In this chapter, non-uniform thickness variations across the whole surface area of a traction-free LG battery is first measured *in situ* during charge and discharge (C-D) cycles via employing an electronic speckle pattern interferometry (ESPI). Second, *in situ* confinement-pressure variations across the whole surface area of constrained battery cells are performed using a high resolution amplified pressure distribution sensor (APDS). These measurements are particularly useful for characterizing the cyclic performance of battery cells, understanding of which must be bridged to that of micro-structural behavior to improve structural design of battery packing.

4.2 In Situ Observation of the Non-homogeneous Deformation in a Free Li-Ion Battery Cell through Electronic Speckle Pattern Interferometer (ESPI)

Li-ion batteries change their volumes due to lithium intercalation and deintercalation. For smaller cells, the cell thickness was measured and modeled as an average value during

cycling (Lee *et al.*, 2003). However, this is not sufficient for large format prismatic pouch cells used in transportation industry, e.g. PHEV cells. Here, the local thickness variations across the whole surface area of large format pouch cells were accurately measured *in situ* via interferometry technique. It shows that the deformation of the cells is highly non-uniform. This inhomogeneous deformation may induce local fracture and failure resulting in early degradation of the cells.

In this section, the experimental procedures are introduced first. Then, the observation results and concluding remarks are described. The detail information (e.g., dimensions, material compounds, and charge−discharge protocols) of the test cells, LG pouch Li-ion battery cells, are illustrated in Appendix A.

4.2.1 *Experimental setup*

The localized cell thickness change across the whole surface area of a LG battery was evaluated *in situ* during cycling via ESPI technique. The ESPI system is designed for non-contact full-field deformation measurement of a scattering object. To calculate the deformation distributions within a range of a few sub-micrometers quantitatively, a four-step phase shifting approach was utilized.

The principle of phase-shifting ESPI system is briefly summarized as follows. Speckles occur when the surface of a rough object is illuminated by coherent light. Since the roughness of the surface is given by statistically distributed peaks and valleys, the intensity and the phase of the resulting wave in different points will be distributed randomly. These intensity fluctuations are speckle and can be described by

$$I^{(k)}(\mathbf{x}) = I_1(\mathbf{x}) + I_2(\mathbf{x}) + 2\sqrt{I_1(\mathbf{x})I_2(\mathbf{x})} \cos(\phi(\mathbf{x}) + \alpha_k), \qquad (4.1)$$

while two coherent light beams with intensity $I_1(\mathbf{x})$ and $I_2(\mathbf{x})$ illuminate on a rough surface. Note that $\phi(\mathbf{x})$ is the relative speckle phase, and $\alpha_k = \{0,\ \pi/2,\ \pi,\ 3\pi/2\}$ is the phase shift at each of the four steps. Then, the phase field $\phi(\mathbf{x})$ can be calculated from the following equation

$$\phi(\mathbf{x}) = \tan^{-1}\left(\frac{I^{(4)}(\mathbf{x}) - I^{(2)}(\mathbf{x})}{I^{(1)}(\mathbf{x}) - I^{(3)}(\mathbf{x})}\right). \tag{4.2}$$

Due to the randomness of the speckles, the relative speckle phase cannot show useful information directly. Only the change of the relative phase, $\Delta\phi(\mathbf{x})$, provides deformation information, i.e., the small displacement field of the rough surface $\mathbf{u}(\mathbf{x})$, as shown in the formula

$$\Delta\phi(\mathbf{x}) = \phi^*(\mathbf{x}) - \phi(\mathbf{x}) = (\mathbf{k}_2 - \mathbf{k}_1) \cdot \mathbf{u}(\mathbf{x}), \tag{4.3}$$

in which $\phi(\mathbf{x})$ and $\phi^*(\mathbf{x})$ are the relative speckle phase maps of undeformed and deformed configuration respectively, and $\mathbf{k}_1$ and $\mathbf{k}_2$ are the propagation wave factors of the two illuminating beams. The in-plane $u_\alpha(\mathbf{x})$ and out-of-plane $u_3(\mathbf{x})$ displacement fields, can be obtained from the unwrapped $\Delta\phi(\mathbf{x})$ by

$$u_\alpha(\mathbf{x}) = \frac{\lambda}{4\pi\sin\theta_\alpha}\Delta\phi(\mathbf{x}),\ \text{for } \alpha = 1,\ 2,$$
$$u_3(\mathbf{x}) = \frac{\lambda}{2\pi(1+\cos\theta_3)}\Delta\phi(\mathbf{x}), \tag{4.4}$$

where θ_α is the angle of incidence of the illuminating beams in in-plane ESPI system. θ_3 is the angle between the direction of object normal and the CCD camera viewing angle in the out-of-plane ESPI system.

76
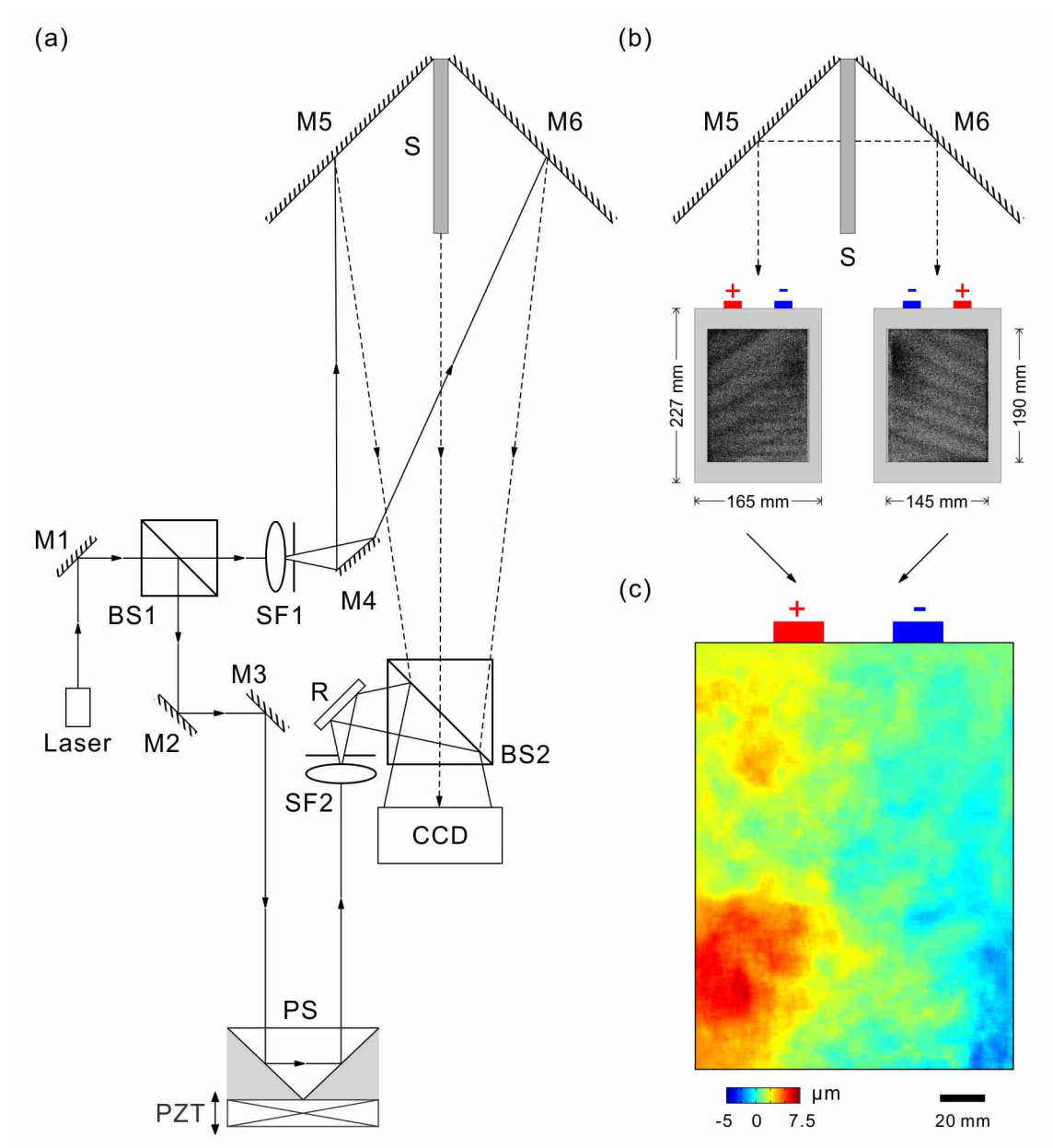
Figure 4.1 (a) The optical setup of ESPI system for out-of-plane displacement field measurement. (b) The experimental setup for *in situ* deformation measurement of a free Li-ion battery cell and the typical interferograms acquired from ESPI. (c) The out-of-plane displacement field post-processed from the interferometer figures.

The optical setup of an ESPI system for out-of-plane displacement field measurement is shown in Figure 4.1(a). The coherent laser light was split into object and reference beams by a beam splitter **BS1**. The object beam was directed onto the object surface via a mirror **M4** and the reference beam was guided onto the reference plate **R** via mirrors and a prism **PS**. The light diffusely reflected from the object surface and was reunited with the reference beam at the second beam splitter **BS2**. Both beams interfered with each other and formed an interference image which was recorded by a CCD camera. The four optical phase shifts α_k to the reference beam were introduced by means of the **PS** mounted on a translational stage with a piezo-electric transducer (**PZT**). The object sample **S**, a LG pouch battery cell, was mounted in the middle of two 45-degree mirrors **M5** and **M6** as illustrated in Figure 4.1(b). Therefore, the interference images of both sides of the cell were recorded simultaneously. Through summation of the two displacement fields acquired from both sides of the cell, any noise and rigid body motion can be cancelled. Figure 4.1(c) is the typical deformation field in this measurement. Note that although Figure 4.1 only shows the setup for the out-of-plane deformation measurement, both in-plane and out-of-plane displacement fields were recorded in this experiment.

4.2.2 *Thickness variation during charge and discharge cycles*

The full-field deformation of a traction-free LG Li-ion battery cell has been measured with a laser ESPI. The deformation fields can be estimated from the following set of equations,

$$\Delta h(\mathbf{x}) = u_3^R(\mathbf{x}) + u_3^L(\mathbf{x}),$$

$$\Delta u_\alpha(\mathbf{x}) = \frac{1}{2}\left(u_\alpha^R(\mathbf{x}) + u_\alpha^L(\mathbf{x})\right), \text{ for } \alpha = 1, \ 2,$$

(4.5)

in which $\mathbf{u}^R$ and $\mathbf{u}^L$ represent the deformation acquired from the right and left side of the cell respectively. The area variation is evaluated by integrating along the outer-surface of the cell Γ

$$\Delta A = \int_\Gamma u_\alpha(\mathbf{x}) n_\alpha(\mathbf{x}) d\Gamma, \text{ for } \alpha = 1, \ 2,$$

(4.6)

where n_α is the normal vector of the integration surface. Hence, the volume variation of the cell can be computed by

$$\Delta \bar{V} = h_0 \Delta \bar{A} + A_0 \Delta \bar{h} .$$

(4.7)

Note the superscript bar means the area-average of the quantities. Finally, the ratio of the volume expansion of the cell is estimated via

$$\frac{\Delta \bar{V}}{V_0} = \frac{\Delta \bar{A}}{A_0} + \frac{\Delta \bar{h}}{h_0},$$

(4.8)

where V_0, A_0, and h_0 are the volume, area, and thickness of the cell in the undeformed configuration respectively.

The normalized variations of the thickness, area, and volume of the cell during the first cycle are illustrated in Figure 4.2. It shows that the volume expansion and shrinkage of the battery cell is mostly dominated by the thickness variation. As a result, the following discussion in this thesis mainly focuses on the out-of-plane deformation.

The contours of the accumulative thickness variation in a free standing cell during the C-D cycles are illustrated in Figure 4.3 and Figure 4.4. The tabs of the cell are in the top position and the positive tab is at the top left. Overall, the reddish colors in the
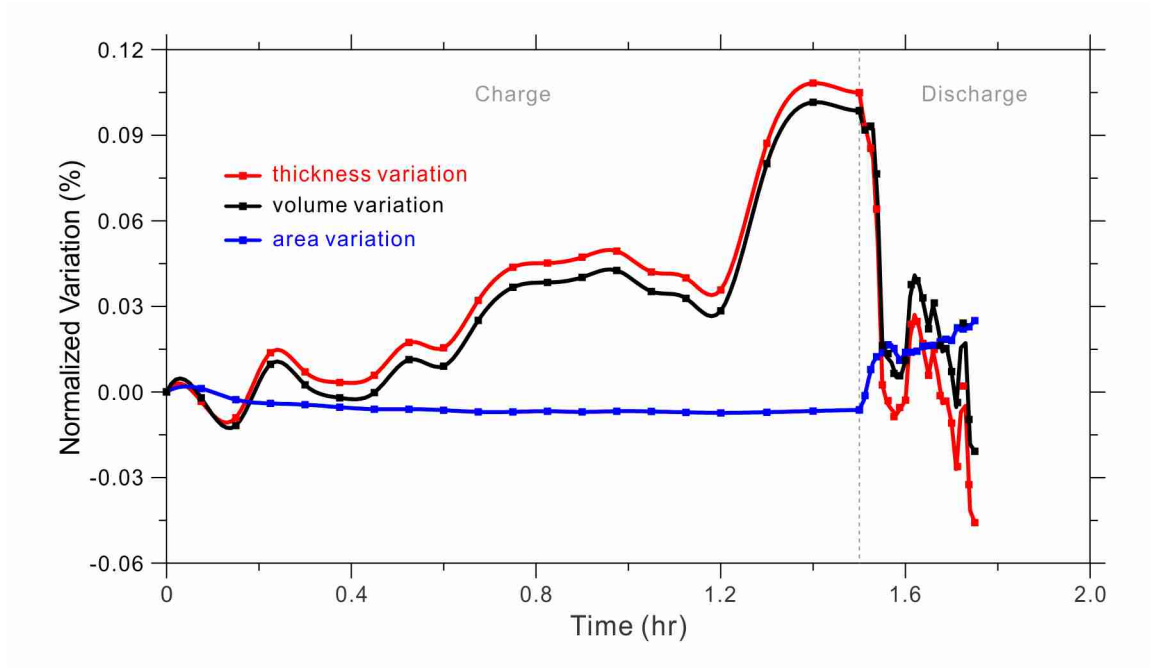
Figure 4.2 The normalized variation of the thickness, area, and volume of the cell during the first cycle (charged in 1C rate and discharge in 2C rate).

contour mean the cell is expanded and the bluish ones represent it is under shrinkage. As shown in the contours, the cell first expands from the bottom right and then gradually swells to the left of the cell in the 3rd cycle. In the meanwhile, the right bottom of the cell starts to shrink during the discharge period of the 3rd cycle. The thickness variation bi-partitions with swell-shrink polarization, and it depolarizes during cycle six. In this cycle, the cell intends to recover its original thickness, especially in the bottom left region (the maximum expansion at the 3rd cycle). However, through this process the cell shrinks more in the bottom portion. It seems that the expansion-shrinkage region of the battery has the diagonal trend at the end of the 6th cycle. At the final cycle (12th cycle), the maximum expansion occurs at the right bottom corner which is far away from the tabs.
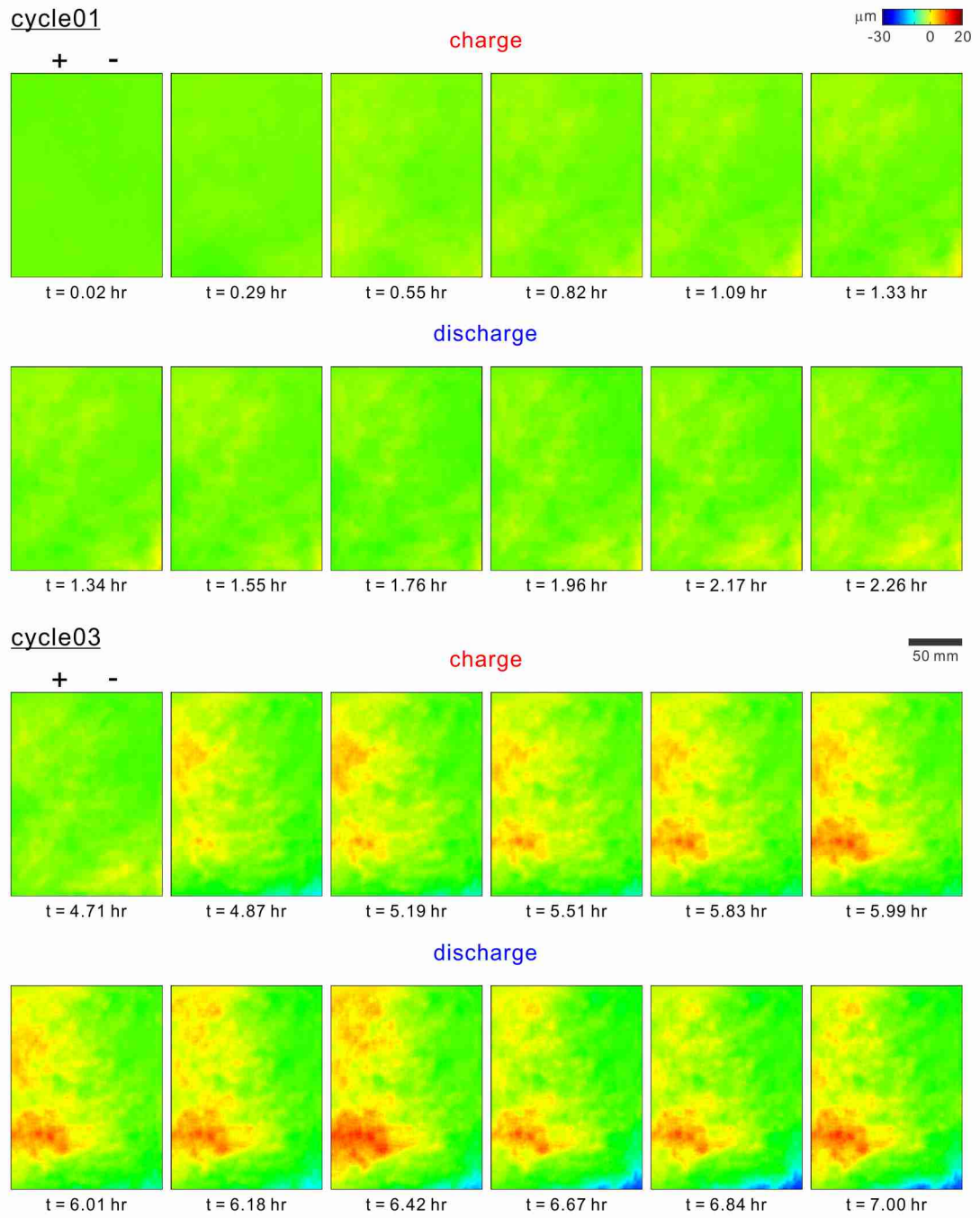
Figure 4.3 The contours of the accumulative thickness variation reference to a fresh, free standing cell at the 1st and 3rd charge-discharge cycles.
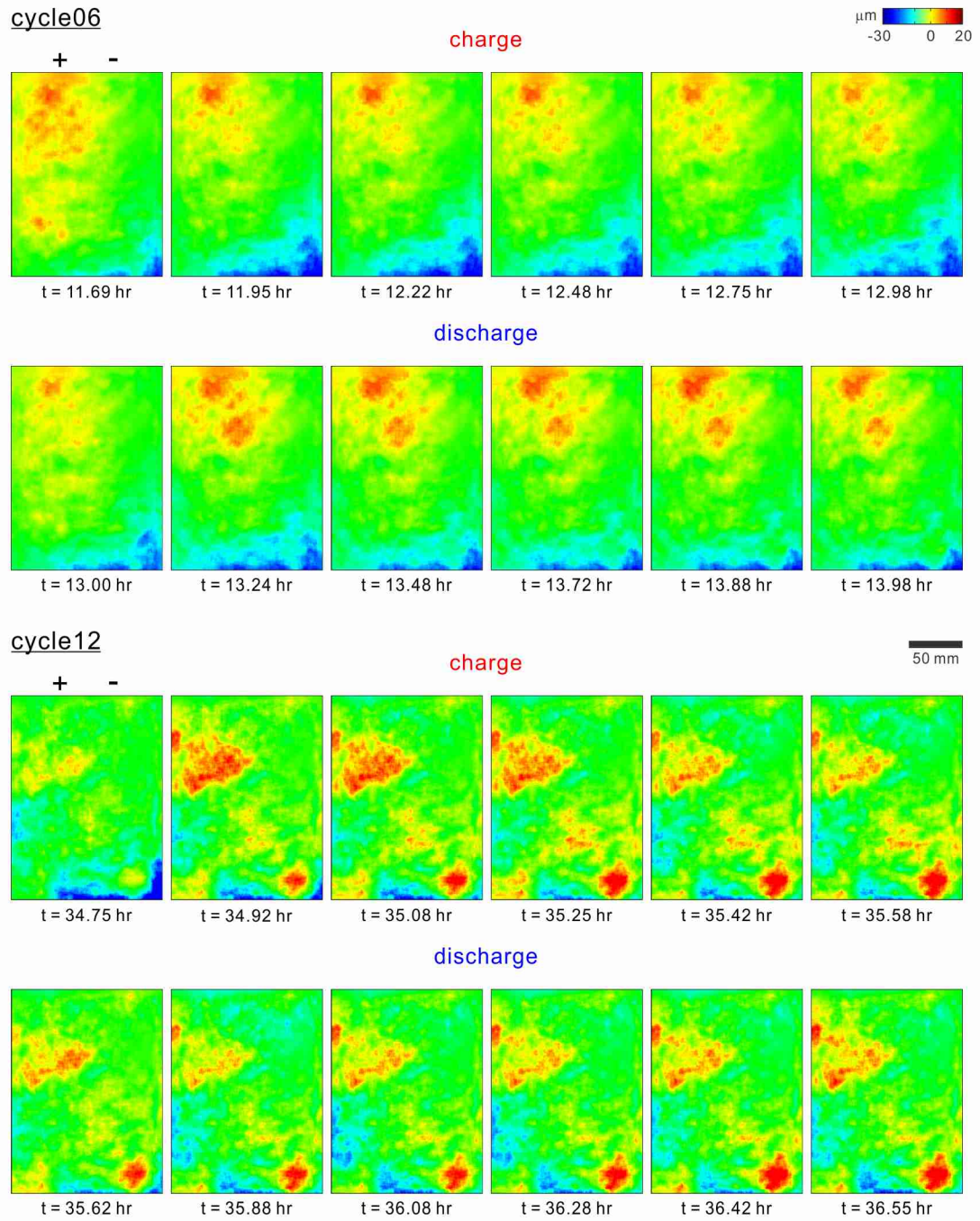
Figure 4.4 The contours of the accumulative thickness variation reference to a fresh, free standing cell at the 6th and 12th charge-discharge cycles.

The swell-shrink polarization developed near the end of the cycle sweeps over the whole area. Although the cell tries to swell and shrink to its original thickness, it cannot fully recover. It can be easily distinguished that the thickness variation of a battery cell is highly inhomogeneous shown in these figures (Figure 4.3 and Figure 4.4).

This non-uniform phenomenon is also presented by the area-average thickness along with extreme values shown as error bars (Figure 4.5). The area-average thickness changes within 6 μm to -3 μm per cycle, 0.35% of the original anode thickness (1700 μm). The total cell thickness increase was approximately 10 μm, when the cell was fully charged. It is known that the cell level volume change is due to the different volume expansion between anodes (graphite ~ 10%) and cathodes (mixture of spinel (~ 0%) and layered oxides (~ 4%)) during Li insertion (Lee *et al.*, 2003; X. Wang *et al.*, 2007). The average cell thickness increases during charging and decreases during discharging, as expected. However, the thickness variation spans ± 25 μm with respect to the average thickness, which is four to eight times of the average value and 1.47% of the original cell thickness. Hence, the local deformation across the cell surface is highly non-uniform and the average thickness is not sufficient to fully represent battery behaviors.

Similar non-uniformity of the electrode expansion was measured from *in situ* neutron images taken during cycling of pouch cells with lithium iron phosphate positive and graphite negative electrodes (Siegel *et al.*, 2013). In Siegel's experiment, the electrode expanded on the top of the cross-section area and slightly shrank at the bottom. This deformation trend is consistent to the displacement contour of cycle six in Figure 4.4. Comparable to 0.35% expansion measured in our experiment, the 0.5% expansion of the battery layers was found to attribute to lithium intercalation in the negative (graphite)
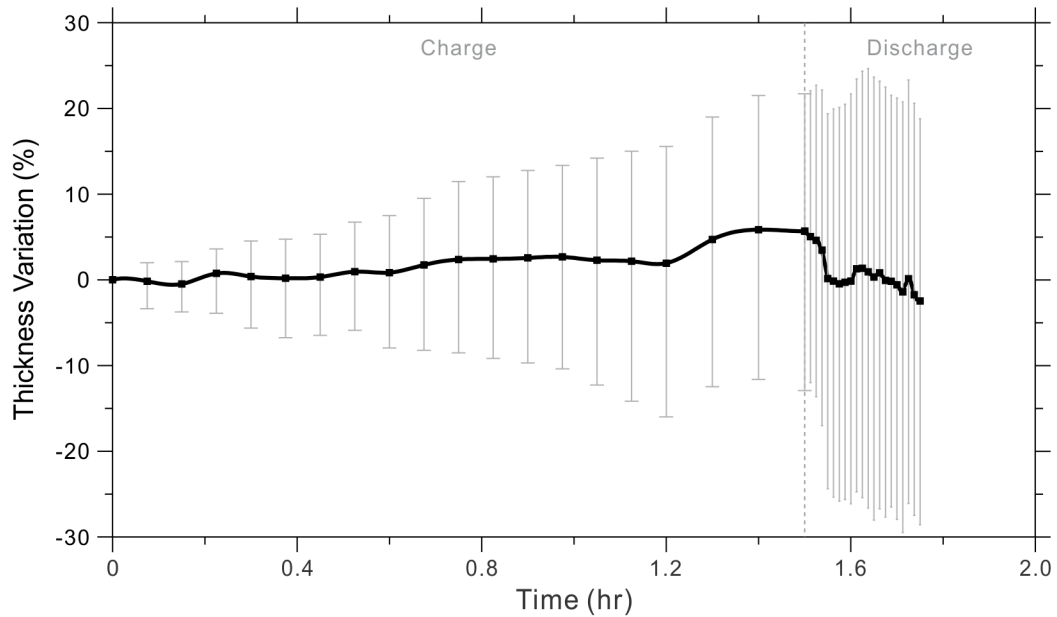
Figure 4.5 The area-average thickness variation with extreme values for the first charge-discharge cycle (charged in 1C rate and discharge in 2C rate).

electrode, which followed the staging of lithium in the graphite material (Dahn, 1991; Takami *et al.*, 1995). Besides, the negative value (~ -0.2) of the total percentage expansion was shown at the end of discharge cycle (at C/5 rate) in Siegel's experiment. Similar shrinkage deformation is observed in Figure 4.2. The thermal distribution of a similar pouch Li-ion battery cell was measured with a discharge rate of 3C by Seong Kim *et al.* (2011) and Yi *et al.* (2013). The temperature distribution was also found non-uniform across the surface of the cell. However, the maximum value always happened near the positive tabs. This is not always true for the thickness variation measured via the ESPI system. Therefore, the thickness variation observed in this thesis is mostly composed of the out-of-plane strain caused by electrochemical processes.

In summary, cell thickness shows large variation across the cell surface area. Peculiar motions of swell-shrink polarization in thickness variations have been observed during a series of C-D cycles. The local deformation across the cell surface is non-uniform and temporally non-monotonic. Hence, the average thickness is insufficient to represent the characteristics of the large format pouch cells used in PHEV. Due to its fast movement of the expansion-shrinkage region during cycling, thickness variation is believed to be caused by gas generation and migration inside the cell. The maximum shrinkage which tends to happen at the edge of the cell could result from the gas moving away from the electrodes to the pockets. Note that similar argument was addressed by Siegel *et al.* (2013). However, it was hard to discern the differences between the electrode deformation and the displacement caused by formation of gasses, since the gas pocket in Siegel's experiment was not large enough for neutron imaging detection. Besides, the thickness variation measured from neutron images was averaged along one of in-plane directions. Therefore, it is hard to distinguish the motion of the gases migration during C-D charges in Siegel's experiment.

4.3   In Situ Stress Variation of Confined Li-Ion Battery Cells via Amplified Pressure Distribution Sensor (APDS)

Since the large non-uniform cell deformation measured from previous section is caused by the gas generation and migration, the gas bubbles inside the cell may lead to loss of contact between particles to particles and particles to current collectors, which then induce earlier failure of the cell. To prevent this bad contact, the cells are constrained during cycling and the stress variations are measured in this section.

4.3.1 Experimental setup

As described in the previous section, the gas generated during C-D cycles can migrate freely in the unconstrained battery cell. The bubble could block the contact between electrode particles and lead to degradation of the cell. Applying mechanical constrains to a battery cell (especially a pouch cell) can help squeeze the gas bubbles to the side of the cell and provide better contact of the electrodes. Further, it can greatly enlongate the cycle life of a Li-ion cell. For example, a few psi compression can increase the cycle life of a battery from hundreds of cycles to thousands of cycles.

To understand the battery mechanism, *in situ* stress distributions of confined LG battery cells were measured via a high-resolution pressure pad. The cell was confined by two 9.6 mm thick aluminum plates via Instron 4502 universal material testing machine. The schematic of the experimental setup is shown in Figure 4.6. Silicone layers were utilized between the cell and the bottom aluminum plate and both sides of the pressure pad for providing better contact. There are 128×128 pressure array sensors with 0.1 inch spatial resolution inside the pad. Through this pressure pad, XSensor IX500.128.128.10, the localized pressure from 2 − 200 psi can be detected with 0.1 psi resolution. Because the pressure resolution and feasible range of the pad are not sufficient to the experiment under lower constrained pressures, an innovative pressure amplifier, named "amplified pressure distribution sensor (APDS)", was invented as illustrated in Figure 4.6(b). The amplifier was made of a cast acrylic plastic cubic (0.5 inch side width) glued with a stainless steel flat head screw. By using this amplifier as an adapter, the contact area changes rapidly from the cross-section of the cubic (0.25 inch square) to the area of the
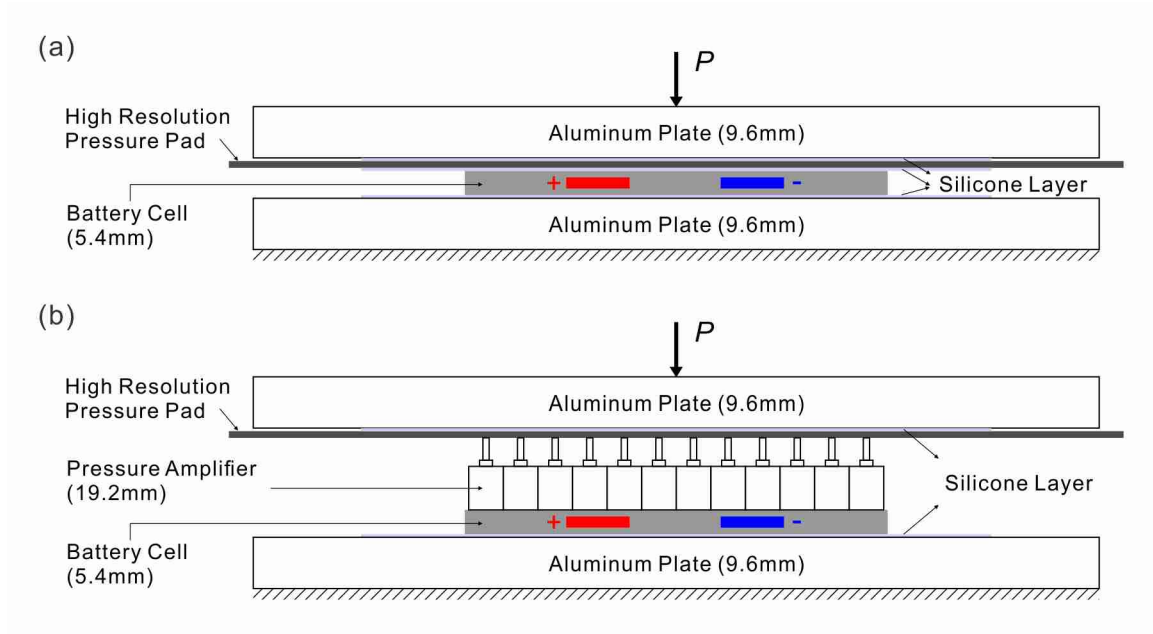
Figure 4.6 The experimental setups for *in situ* stress distribution measurements: (a) under higher constrained pressures. (b) under lower constrained pressures.

Cell SN	Past Test History	Nominal Capacity	Average Thickness
JB08120031 *(a) New Cell*	constant 1C rate at room temperature	15.0 Ah	5.52 mm
JB08110773 *(b) 93.8%*	constant 1C rate at room temperature	14.3 Ah	5.54 mm
JB08110773 *(c) 91.5%*	constant 1C rate at room temperature	13.9 Ah	——– *
HJ16110778 *(d) 82.7%*	DST type of cycling at 30 °C	12.4 Ah	5.75 mm
HJ18110642 *(e) 11.3%*	constant rate (1C/2C type) cycling at 50-55 °C	1.7 Ah	6.95 mm

Table 4.1 A list of the cells tested in the confinement experiment. (*The cell (c) is continuously prestressed and measured after cell (b).)

screw (inch square, sensing as one grid point in the pad), which increases the pressure 25 times. Therefore, the amplifier enlarges the pressure range of the pad lower to 0.08 psi with 4×10^{-3} psi resolution. The APDS was tested and assured to have 99.84% accuracy.

During the *in situ* measurement, the stress distribution was recorded every one minute. The cells were all charged and discharged in 1C rate as described in Appendix A. The five cells, listed in Table 4.1, under different stages were tested and recorded. The experimental results are discussed in the next sub-section.

4.3.2 Confinement-pressure variations during charge and discharge cycles

The contours of the stress distribution for the cell (a) listed in Table 4.1 is shown in Figure 4.7. The cell, under -13 psi prestressed compression, was charged and discharged in constant 1C rate followed the protocol described in Appendix A. During C-D cycles, the pressure distribution kept its spatial pattern and did not evolve with lithium intercalation or deintercalation. Unlike the quick motion of the cell swelling observed in a free cell thickness variation measurement, only the amplitude of the pressure distribution varies during cycling. This observation shows that the constraint on the surface of the cell successfully suppresses non-uniformity of the stress distribution induced by lithium insertion and removal. Therefore, the area-average of pressure distributions is sufficient to represent the cell mechanism.

The area-average stress variations for a brand-new cell (cell (a) in Table 4.1) under high prestressed pressures, i.e., $10 - 40$ psi, are illustrated in Figure 4.8(a). These pressure variations are composed of two distinct characteristics: one is coherent with the C-D cycles and the other is gradually increasing regime. The former shows that the area-
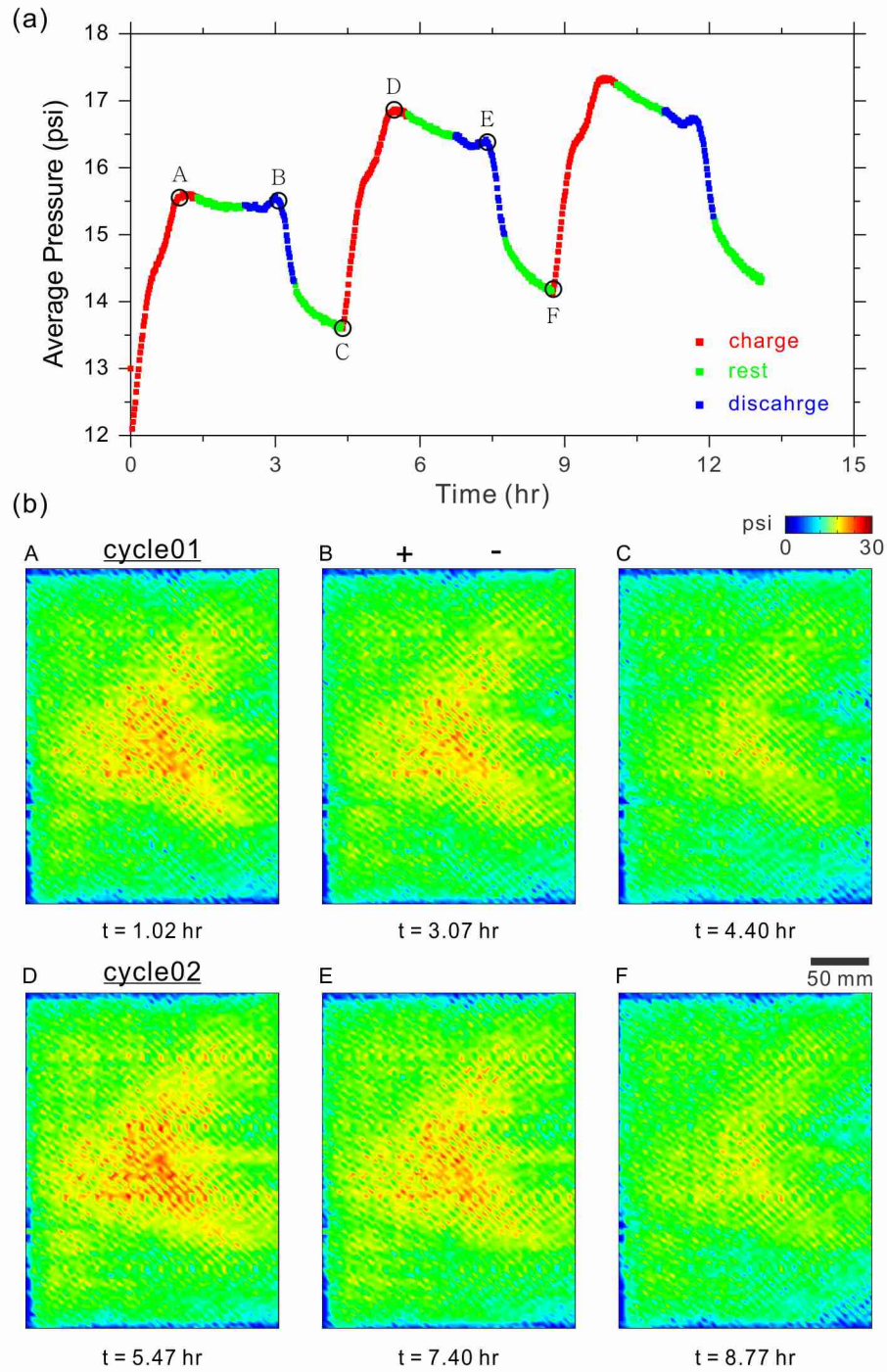
Figure 4.7 (a) The history and (b) the contours of area-average stress distributions during C-D cycles under the displacement constraint with -13 psi prestressed pressure.
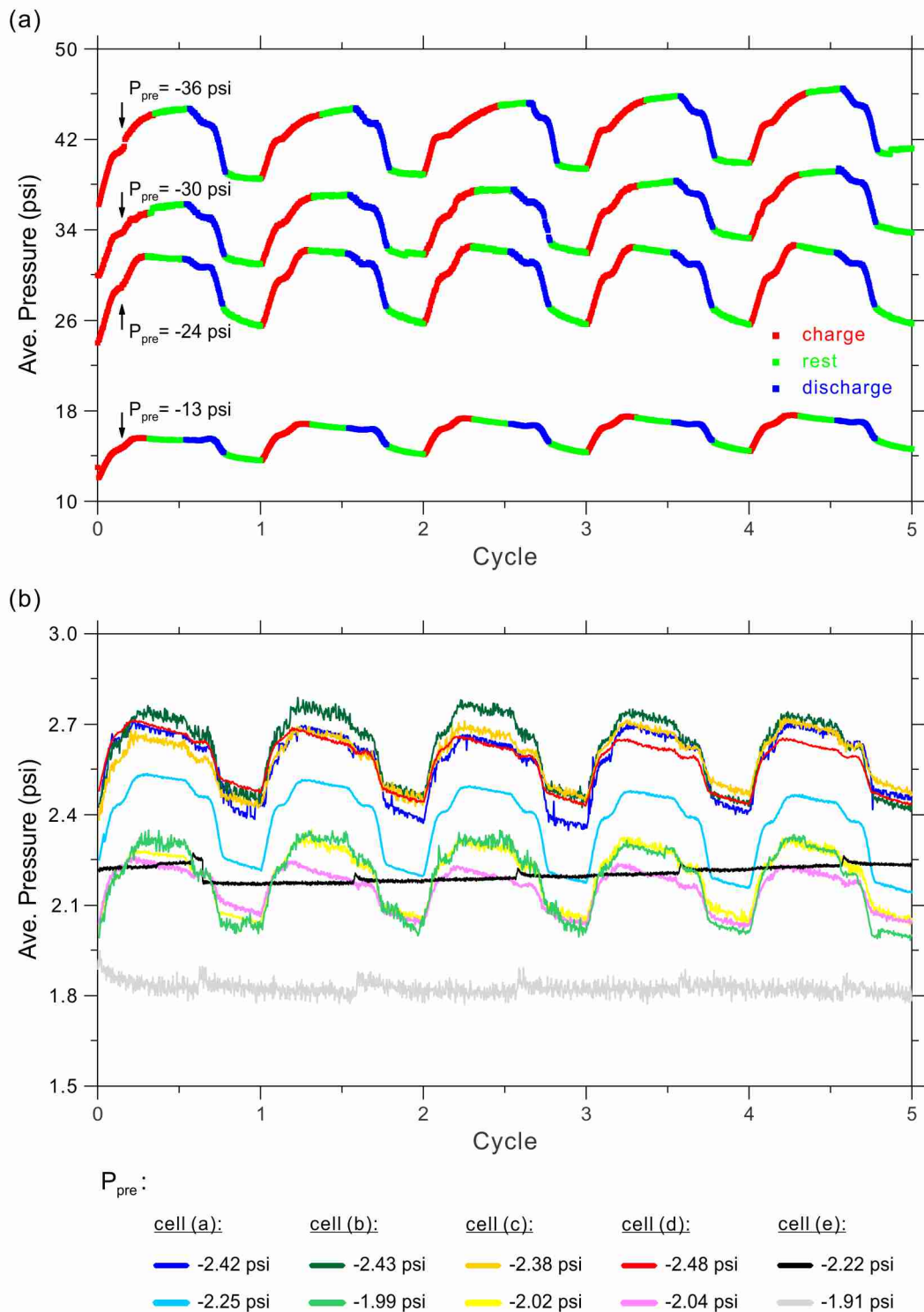
Figure 4.8 (a) The area-average stress variation for a brand-new cell (cell (a) in Table 4.1) under high prestressed pressures during C-D cycles. (b) The area-average stress for one new cell (cell (a)) and four aged cells (cell (b) − (e) listed in Table 4.1) under low constrained pressures.

average pressure has periodic behavior. The stress of the cell increases during charging periods and decreases during discharging cycles. This reversible feature is considered to be attributed to the electrode deformation due to intercalation and deintercalation of Li ions. Note that the amplitude of the coherent variation enlarges with the increase of the prestressed compression. The other attribute is irreversible accumulative stress. The area-average pressure increases or decreases gradually during C-D cycles. This characteristic indicates that the existing or new forming gas bubbles inside the surface are trapped by the rising contact area. Here, the gases generated during the cycling are considered to be squeezed at the solid interfaces.

In situ stress distribution measurement was further performed for the same new cell and four aged cells (cell (b) − (e) listed in Table 4.1) under low constrained pressure, i.e., 2 − 3 psi. Figure 4.8(b) shows the average pressure variations in low prestressed tests. The bluish curves represent the average pressure for the new cell. The greenish curves are for the cell (b) with 93.8% capacity. The yellowish curves and reddish curves represent cell (c) and (d) respectively. The cell (e) with only 11.3% capacity remain is delineated in the grayish curves. The reversible and irreversible characteristics of the average stress can also be clearly observed for the cell (a) − (d) under low prestressed pressures. However, the amplitude of the stress distribution for the new cell (a) is larger than that for the aged cells, e.g. comparing cell (a) under 2.42 psi prestressed pressure with cell (d) under 2.48 psi prestressed pressure. It is because the bubble-gases inside the aged cells decrease the amplitude of the reversible stress. Moreover, the reversible regime can hardly be distinguished for the aged cell (e), since the stress introduced from Li-ion intercalation and deintercalation is relative small due to its low capacity.

4.4 Micromechanical Internal State Model of the Li-Ion Battery Cell

From the experimental results, the cell deformation was found to be caused not only by lithium-ion intercalation and de-intercalation, but also by bubble-gas generation and evolution. Therefore, to better understand the mechanical behavior of the battery cell, a micro-mechanical internal state model is developed.

The model is composed of the electrode deformation caused by lithiation and delithiation, the pressure variations generated from bubble-gases accumulation, and the stresses introduced by the contact mechanism between internal solid interfaces. Supported by experimental results, it shows that the evolution of bubble-gases plays a significant role and cannot be neglected in battery mechanism, especially for a large format pouch cell. By constructing a porous media mechanics model, the cell local strain and pressure experimental results can be explained.

4.4.1 Formation of the model

In this micro-mechanical internal state model, the battery cell is simplified into three idealized phases: effective solid electrodes (α phase), the bubble-gases phase (β phase), and effective soft materials (γ phase), e.g. separators and binders. The schematic figure of the model is shown in the Figure 4.9. Electrolytes and bubble-gases are assumed to be trapped in effective soft materials. Since the electrolyte is a liquid-based material, it does not contribute to cell stresses. On the other hand, the bubble-gases influence the stress of cells with pressure P_g^A. The contribution of eigen-displacement δ_{eigen}^A caused by lithium intercalation and de-intercalation is considered in the electrode only. To simulate the experimental setup, the microstate system, system A in Figure 4.9, is fixed in vertical
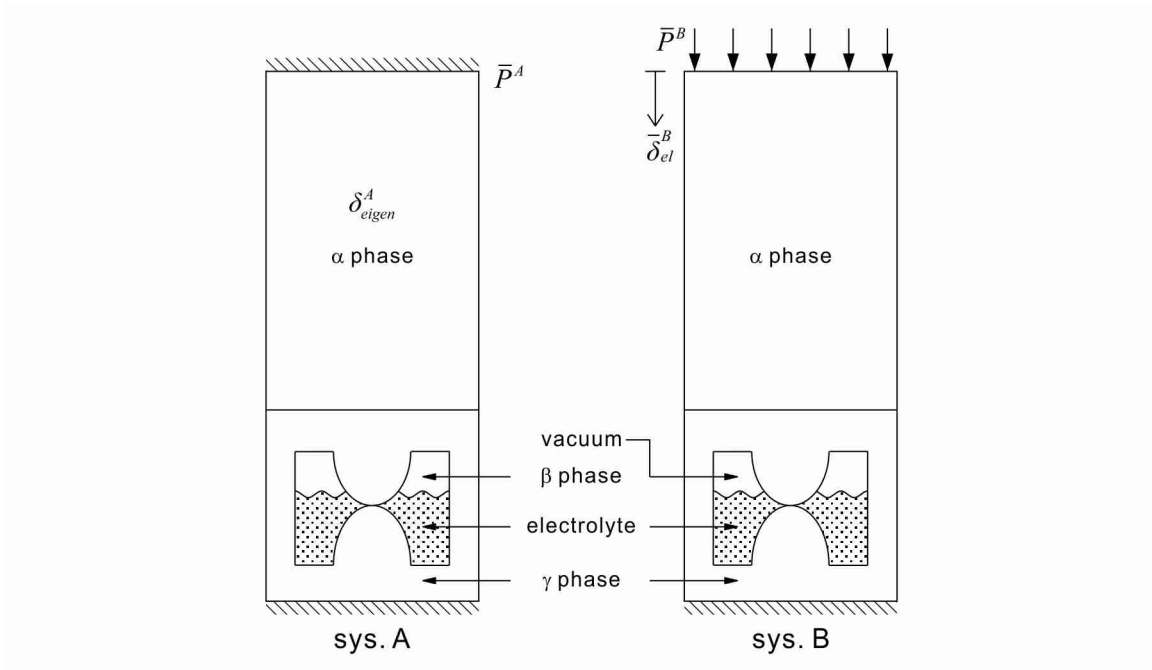
Figure 4.9 The schematic of the mechanical internal state model.

direction ($\bar{\delta}^A = 0$) with an average prestressed stress $\bar{P}^A$ on the top of the surface. Note that the system follows periodic boundary conditions (PBC) in the horizontal direction. The contact mechanism is modeled inside the effective soft material, since the contact pressure induced by the interfaces made of soft materials is more significant comparing with that between stiffer materials, e.g. electrodes.

Because the displacement in electrodes is composed of two compatible parts: the elastic displacement δ_{el} and the eigen-displacement δ_{eigen}. To decompose δ_{eigen} from the system, the auxiliary field system B is created and set to have the same elastic solid as system A but without the eigen-displacement, i.e., $\delta_{eigen}^B = 0$. The other difference between the auxiliary field and the real field is that the top surface of the auxiliary field is free to deform ($\bar{\delta}^B$ in the displacement, while applied pressure $\bar{P}^B$). Instead of having

gases in the effective soft material of system B, the cavity is vacant and the contact surfaces are allowed to interpenetrate each other.

Use the reciprocal theorem to relate the two elastic solids,

$$\int_V \left(\boldsymbol{\sigma}^A : \mathbf{u}_{el}^B \otimes \nabla \right) dV = \int_V \left(\boldsymbol{\sigma}^B : \mathbf{u}_{el}^A \otimes \nabla \right) dV , \tag{4.9}$$

where $\boldsymbol{\sigma}$ is the stress state and $\mathbf{u}_{el} \otimes \nabla$ is the gradient of the elastic displacement field. Note that in the whole derivation, the superscript represents the quantity is in which system (system A or B) and the bar symbol represents the variable is on the surface; e.g. $\bar{P}^A$ is the applied pressure on the surface in system A.

According to divergence theorem,

$$\int_V \left(\boldsymbol{\sigma}^A : \mathbf{u}^B \otimes \nabla \right) dV = \int_V \left\{ \nabla \cdot \left(\boldsymbol{\sigma}^A \cdot \mathbf{u}^B \right) - \left(\nabla \cdot \boldsymbol{\sigma}^A \right) \cdot \mathbf{u}^B \right\} dV = \int_{\partial V} \mathbf{t}^A \cdot \mathbf{u}^B \, dS , \tag{4.10}$$

where $\mathbf{t}$ is the surface traction and $\nabla \cdot \boldsymbol{\sigma}^A = 0$ is based on the balance of linear momentum in a static problem in the absence of body forces. Note that there is no eigen-displacement in system B. Hence, $\mathbf{u}^B = \mathbf{u}_{el}^B + \mathbf{u}_{eigen}^B = \mathbf{u}_{el}^B$. Therefore,

$$\int_V \left(\boldsymbol{\sigma}^A : \mathbf{u}_{el}^B \otimes \nabla \right) dV = \int_{\partial V} \mathbf{t}^A \cdot \mathbf{u}^B \, dS . \tag{4.11}$$

Similarly,

$$\int_V \left[\boldsymbol{\sigma}^B : \left(\mathbf{u}_{el}^A + \mathbf{u}_{eigen}^A \right) \otimes \nabla \right] dV = \int_{\partial V} \mathbf{t}^B \cdot \mathbf{u}^A \, dS . \tag{4.12}$$

Subtracting equation (4.12) from (4.11) and organizing with equation (4.9) gives

$$\int_{V_e + V_s} \left(-\boldsymbol{\sigma}^B : \mathbf{u}_{eigen}^A \otimes \nabla \right) dV = \int_{\partial V_e + \partial V_s} \left(\mathbf{t}^A \cdot \mathbf{u}^B \right) dS - \int_{\partial V_e + \partial V_s} \left(\mathbf{t}^B \cdot \mathbf{u}^A \right) dS , \tag{4.13}$$

where ∂V_e is the surface domain of the effective electrode and ∂V_s is that of the effective soft material.

Since the eigen-displacement δ^A_{eigen} is only contributed from the electrode, the left hand side of equation (4.13) can be expressed by

$$\int_{V_e+V_s}\left(-\boldsymbol{\sigma}^B:\mathbf{u}^A_{eigen}\otimes\nabla\right)dV = \varepsilon^A_{eigen}\cdot\overline{P}^B A_e h_e = A_e\overline{P}^B\delta^A_{eigen}. \qquad (4.14)$$

where ε^A_{eigen} is eigen-strain in system A; h_e and A_e are the thickness, and cross-section area of the electrode respectively.

The right hand side of equation (4.13) is the integration of traction dot the corresponding displacement in the other system along the surface. Because of the periodic boundary conditions in the horizontal direction, the integrant along the left side of the surface cancels with that along the right side of the surface. This relation holds for the electrode and soft material regions in both systems. Besides, the stresses and displacements at the interface between the electrodes and soft materials are continuous in both systems, so the integrants along the interface equal zero. Since both systems are fixed in the bottom, the integrants along bottom surfaces are also vanished.

As the result, the second term of the right hand side of equation (4.13) becomes

$$\int_{\partial V_e+\partial V_s}\left(\mathbf{t}^B\cdot\mathbf{u}^A\right)dS = \overline{P}^B\overline{\delta}^A + \int_{\partial V_{s\_g}}\left(P^B_g\cdot\mathbf{u}^A\right)dS + \int_{\partial V_{s\_inner}}\left(\mathbf{t}^B\cdot\mathbf{u}^A\right)dS = 0. \quad (4.15)$$

While the system is fixed at the top ($\overline{\delta}^A = 0$) and the cavity inside the system B is vacant ($P^B_g = 0$). Considering the counter surfaces are allowed to interpenetrate each other in the system B, the traction in the system B across the contact area in A is zero. The first term of the right hand side of equation (4.13) is derived as

$$\int_{\partial V_e+\partial V_s}\left(\mathbf{t}^A\cdot\mathbf{u}^B\right)dS = \overline{P}^A\overline{\delta}^B_{el}A_e - P^A_g\int_{\partial V^B_{s\_inner}}u^B_n\,dS + \int_{\partial V^A_c}\left\{P^A_c\left(\overline{\delta}_{pre},P^A_g\right)\right\}[\![u^B_c]\!]\,dS, \quad (4.16)$$

where u_n^B is the displacement in the normal direction of the inner surface of the cavity

$(\partial V_{s\_inner}^B)$ in the effective soft material of system B. $P_c^A\left(\bar{\sigma}_{pre}, P_g^A\right)$ is contact pressure

along the contact surface ∂V_c^A in system A. It is a function of prestressed pressure $\bar{\sigma}_{pre}$

and gas pressure P_g^A in system A. $\llbracket u_c^B \rrbracket$ is the displacement jump in the system B across

the contact area in the system A. The elastic displacement of the top surface in system B

is denoted as $\bar{\delta}_{el}^B$. Substitute equation (4.14), (4.15), and (4.16) into equation (4.13). Then,

it yields

$$\bar{P}^A \bar{\delta}_{el}^B A_e = A_e \bar{P}^B \delta_{eigen}^A + P_g^A \Delta V_{cavity}^B - \int_{\partial V_c^A} \left\{ P_c^A\left(\bar{\delta}_{pre}, P_g^A\right) \right\} \llbracket u_c^B \rrbracket \, dS. \qquad (4.17)$$

Note that $\Delta V_{cavity}^B = \int_{\partial V_{s\_inner}^B} u_n^B \, dS$ is the change of cavity volume in system B and $\bar{\delta}_{pre}$ is

prestressed displacement which gives $\bar{\sigma}_{pre}$.

Here, introducing the linear relationships in the system B,

$$\bar{\delta}_{el}^B = \alpha \bar{P}^B, \quad \Delta V_{cavity}^B = \beta \bar{P}^B, \quad \llbracket u_c^B \rrbracket = \gamma \bar{P}^B. \qquad (4.18)$$

where the factor α is the modulus indicates the deformation due to applying an unit

pressure on the top surface of the system B. Similarly, while applying an unit pressure to

the system, the factor β represents the change of the cavity volume, and the factor γ

shows the displacement jump in the system B across the contact area. Replacing $\bar{\delta}_{el}^B$,

ΔV_{cavity}^B, and $\llbracket u_c^B \rrbracket$ in equation (4.17), finally, the average pressure (surface traction) $\bar{P}^A$

on the top of the surface can be expressed as

$$\bar{P}^A = \frac{\delta_{eigen}^A}{\alpha} + \frac{\beta}{\alpha A_e} P_g^A - \frac{\gamma}{\alpha A_e} \int_{\partial V_c^A} \left\{ P_c^A\left(\bar{\delta}_{pre}, P_g^A\right) \right\} \, dS. \qquad (4.19)$$

4.4.2 Finite element analysis of the model

Since the eigen-displacement δ_{eigen}^A caused by Li-ion intercalation and deintercalation is decomposed from the gas and contact pressures in equation (4.19), a linear elastic solid with the latter two pressures is introduced and analyzed by finite element method via the software ABAQUS. To obtain the average pressure (surface traction) $\overline{P}^A$ on the top of the surface, the simulation model can be simplified as illustrated in Figure 4.10(a). The dimensions of the electrodes and separators are set to be the same as the information provided in Appendix A. Note that the effective contact radius $R_s = 10 \ \mu m$ is determined by the typical radius of natural graphite (Zaghib *et al.*, 2001) and in accordance with the porosity of the separator (Arora & Zhang, 2004), i.e., $V_{cavity}/(w \times h_s) \approx 40\%$. The boundary and loading conditions are consistent with those described in previous sub-section 4.4.1. In the auxiliary field (system B), the undeformed model is free at the top and the cavity between separators is vacant. The contact surface in system B is allowed to inter-penetrate each other freely. It represents a dummy cell as an intermediate step. On the other hand, in the real field (system A), the same undeformed solid is first deformed from the original configuration due to initial prestressed displacement and then fixed at the top. The stress contour σ_{22} of the deformed solid with -36 psi prestressed pressure is shown in Figure 4.10(b). Note that the cavity in system A is filled with gas and electrolytes. According to PBCs in the horizontal direction in both systems, the figures in transparent colors represent the models and stress fields of adjacent units.

Via this process, the amount of gases generated during the C−D cycles can be estimated. In the simulation, the dimensions and the material properties of the model are shown in Figure 4.10. The thickness of the electrode and the thickness of the separator,
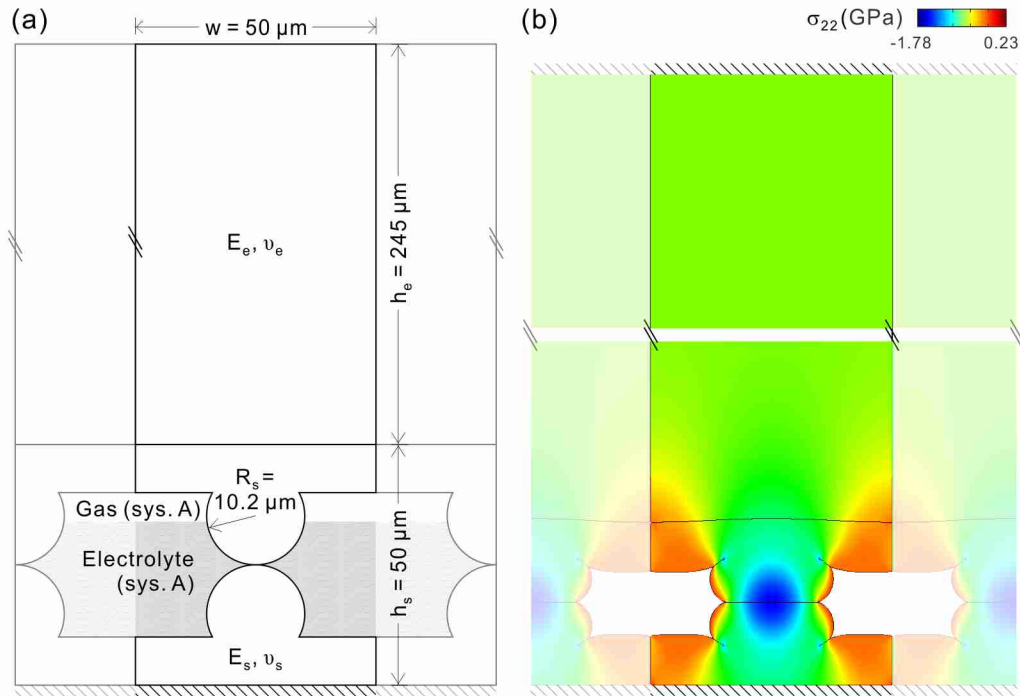
Figure 4.10 (a) The schematic of finite element models. In the auxiliary field (sys. B), the undeformed model is free at the top and the cavity between separators is vacant. In the real field (sys. A), the solid is deformed from the undefromed configuration due to initial prestressed and then fixed at the top. The cavity is filled with gas and electrolyte. (b) The stress contour σ_{22} of the deformed solid with -36 psi prestressed pressure.

h_e = 245 μm and h_s = 50 μm, are equal to the dimensions of the cell illustrated in Appendix A. The width of the model, w = 50 μm as the characteristic length, is set to be the same as h_s. By changing the characteristic length, the frequency of the contact area can be controlled. The effective Young's modulus and poison ratio for the electrodes are E_e = 15.73 GPa and υ_e = 0.25. For the separators, these two material properties are E_s = 2.50 GPa and υ_s = 0.40 respectively. Both electrodes and separators are meshed by 4-node bilinear plane strain quadrilateral elements with reduced integration, i.e., CPE4R in ABAQUS.

4.4.3 Verification of the internal state model with experimental data

A micromechanical internal state model of battery cells is developed to capture both state of charge (SOC) dependence and gases evolution-induced cell pressures with respect to the prestressed pressure. The simulation results and experimental data of the area-average pressure for cell (a) in Table 4.1 under three different prestressed pressures (-36 psi, -24 psi, and -13 psi) are illustrated in Figure 4.11(a). As shown in the figure, the modeling results could capture the dependence of the overall confinement pressure variation. Distinguish the numerical results with contact pressure (dotted line with circle markers) from those excluding contact mechanism (dotted line with start markers). The model indicates that the contribution of the internal solid interfacial contacts to the confinement pressure variations is not negligible. Besides, the difference between the simulation results and *in situ* cell pressure measurement is mainly attributed to gas generation. Since the modeling results are slightly smaller in the 1st cycle but greater in the 5th cycle, the gas generation rate should not only linearly increases (current assumption; Appendix B), but also exponentially decays with cycling times. The other discrepancy happens while the cell is during discharge cycles. It seems that state of charge (SOC) curve cannot fully capture cell pressure especially during discharge periods.

The simulation results and experimental data of the normalized area-average stress under low constrained pressures for cell (a) − (d) are shown in Figure 4.11(b). The integrated mechanical-electrochemical model can capture both Li-ion intercalation and deintercalation behaviors and gas evolution induced cell pressures for different stages of the cells. Consistent with the experimental data, the modeling results show the amplitude
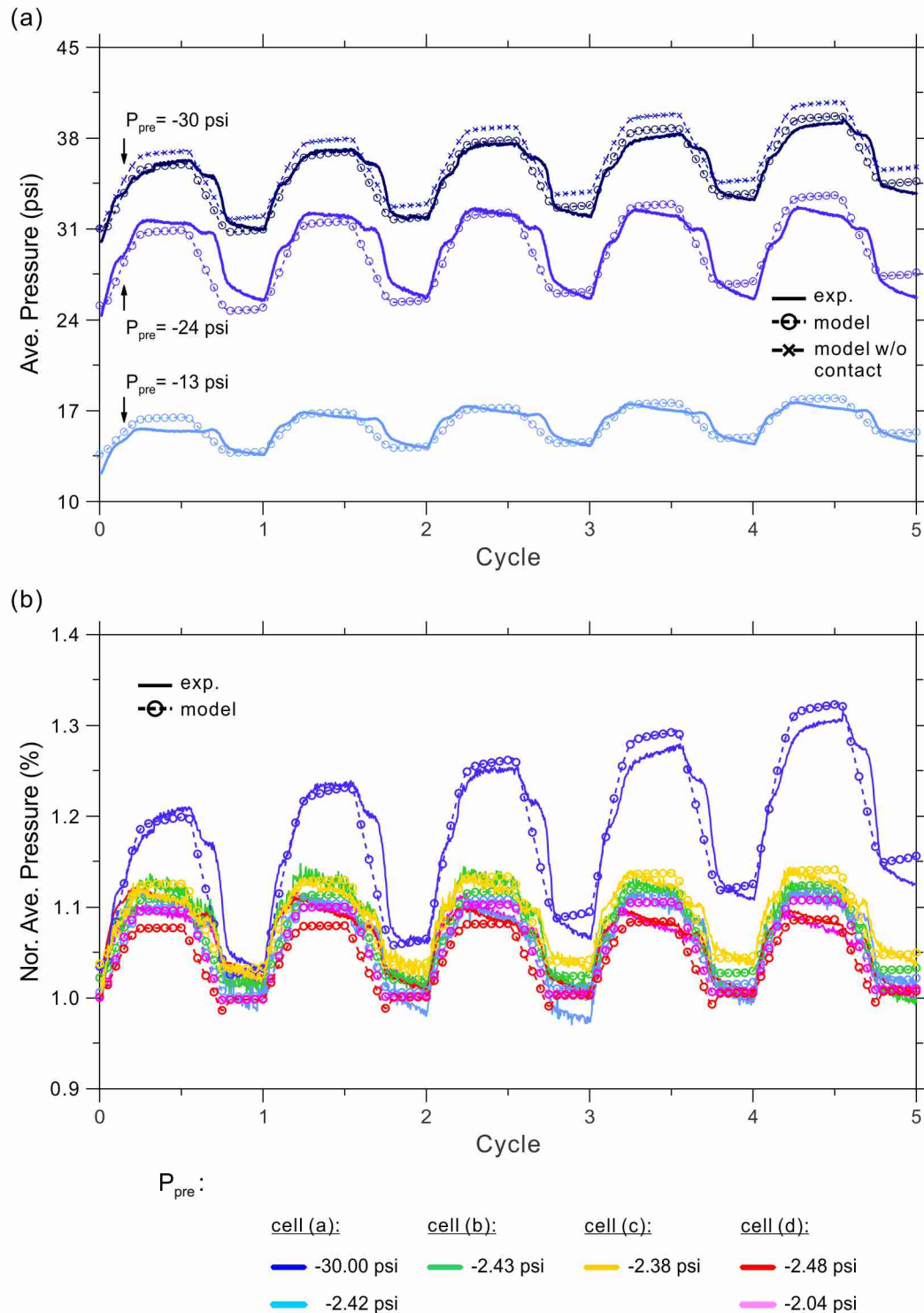
Figure 4.11 The simulation results and experimental data of the area-average pressure under (a) high prestressed pressures. (b) low initial prestressed pressures for cell (a) − (d) in Table 4.1. Note that the modeling results without the contact pressure term under prestressed pressure -30psi is shown in (a) for comparison.
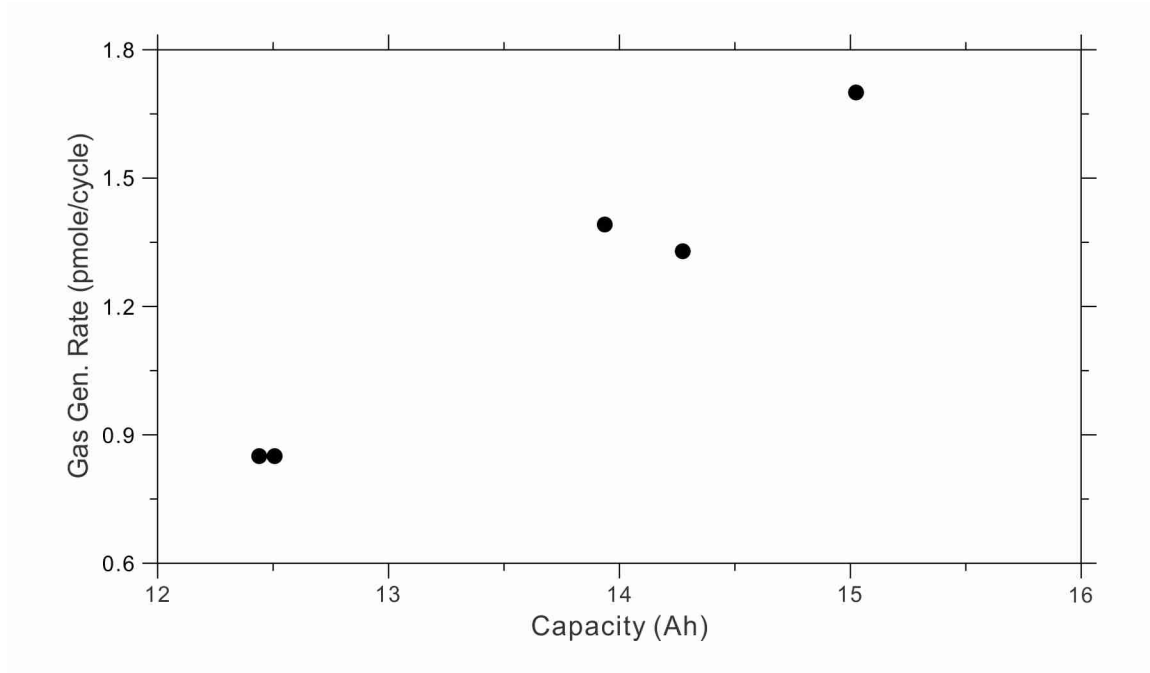
Figure 4.12 The gas generation rates estimated from internal state model for cell (a) − (d) under low initial prestressed pressures.

of the reversible part of the stress is smaller for the aged cell (cell (d)) than that for the new cell (cell (a)). It is because the gases inside the aged cells decrease the stress amplitude of the reversible stress and also the stress introduced from lithiation is relative deficient due to its lower capacity.

The coefficient of the gas generation rate is estimated from the internal state model. The coefficients for cell (a) − (d) under approximate -2 psi low initial prestressed pressures are linearly dependence of the cell capacity as shown in Figure 4.12. This is because only few portions of the electrodes in the aged cell are still active and participate the lithiation and delithiation cycles.

The average capacities for the new cell (a) and two aged cells, cell (d) − (e), are tested under different prestressed pressures. As shown in Figure 4.13, the average
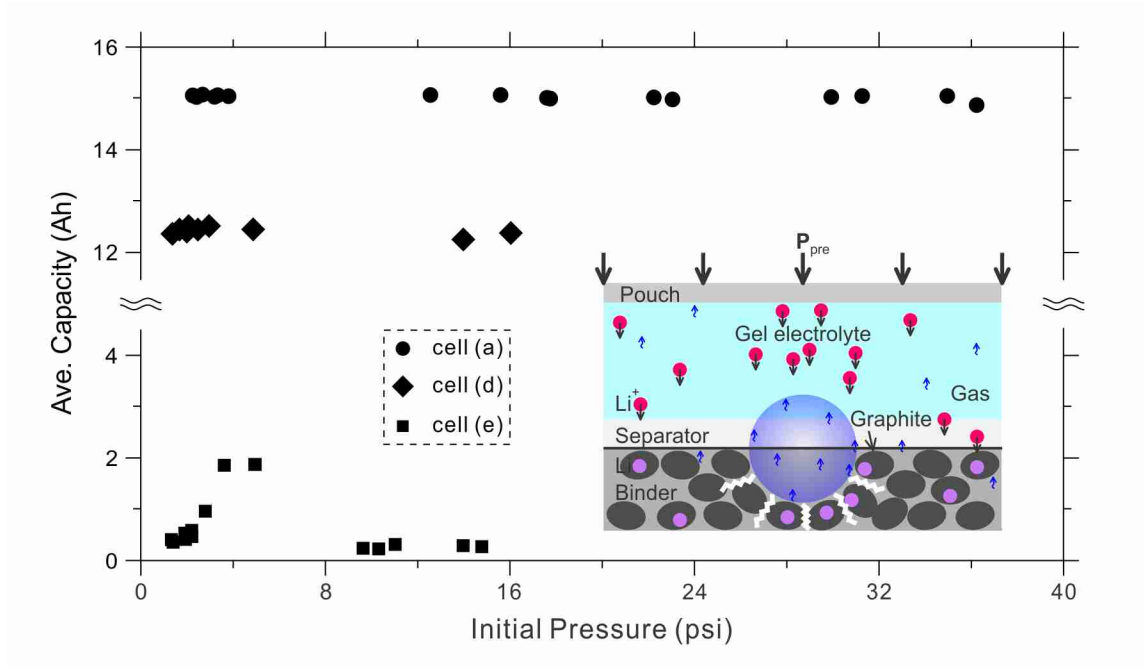
Figure 4.13 Average capacities for the cells (a), (d), and (e) under different initial prestressed pressures. Inset: A schematic of interface bubble-gas generation (IB-GG) by confinement control.

capacities for the new cell (a) and aged cell (d) almost remain constant while the applied prestressed pressure increases. On the contrary, the average capacity for the aged cell (e) increases significantly while the applied prestressed pressure is $4 - 5$ psi. It is because the contact area of the electrodes increases with increasing cell compression. Also, the low prestressed pressure can help bubble-gases to dissolve into electrolytes instead of migrating inside the cell as a gas state. Similar densification of the cell components was found in the compressive tests of representative volume element specimens by Lai *et al.* (2014). However, higher confined pressure, i.e., bigger than 10 psi, may trap the bubble-gases inside the cell and further decrease the contact area of the electrodes. Besides, as shown in the schematic (inset in Figure 4.13), the high prestressed pressure applied on the cell increases the internal pressure and forms more micro-cracks. This increases new

surfaces of the electrode and results in more SEI formation and gas generation. Finally, this process leads to early degradation of the battery cell. Here, applying high pressures to the cell is similar to indenting the cell with gases and may lead to onset of short circuits (Sahraei *et al.*, 2014). Moreover, it may induce separator creep and expedite the aging mechanism of the cell while applying high pressures to the cell (Peabody & Arnold, 2011).

Cell mechanical constraints (cell compression) can impact cell performance and life. Particles which swell during cycling become disconnected without compression applied on the surface of the cells. This deformation induced bad contact leads to increasing internal resistance and decreasing cell capacity. Maintaining a compressive force on the electrodes can provide a uniform contact of all components and prevent the delamination of the active material from the current collector. By constructing a porous media mechanics model, the cell local strain and pressure experimental results can be explained. Further, the gas generation rate can be predicted during the battery degradation process.

4.5 Concluding Remarks

Deformation of a free standing LG Li-ion battery cell measured with ESPI has revealed that the thickness variation caused by C-D cycling is highly non-uniform. Due to its fast swell-shrink polarization movement of the expansion-shrinkage region during cycling, the thickness variation is believed to be caused by gas generation and migration inside the cell. Besides, the stress variations of displacement-constrained Li-ion battery cells were measured *in situ* by employing a high resolution APDS. Under the fixed displacement

constrained conditions, the battery cell pressure arises from the electrode deformation caused by Li ion intercalation and from the gas generation and migration. These two measurements are particularly useful for characterizing the cyclic performance of battery cells, understanding of which must be bridged to that of microstructural behavior to improve structural design of battery packing.

Therefore, a micromechanical internal state model of battery cells has been made and simulated. It captures both SOC dependence and gas evolution-induced cell pressure. It shows the contact mechanics has contribution to the cell stress especially for the larger prestressed pressure. Also, the result indicates that the gas plays an important role in the battery mechanism. Applied prestressed pressure can increase the electrode contact area. Therefore, the battery life is efficiently elongated. The current model can be used as a unit constitutive model to analyze gas migration/leakage in the battery and its effects on micro-cracking and degradation of electrodes.

Appendix A: The LG Pouch Li-Ion Battery Cells

In this chapter, *in situ* deformation and stress measurements are performed on large format pouch LIB cells from LG Chem. There are 10 to 20 mini cells inside each pouch. Each mini cell contains two layers of cathodes, two layers of electrodes, two current collectors and two separators. The nominal thickness and dimension of each component are illustrated in Figure 4.14(a). The anode is coated graphite and the cathode material is a mixture of spinel $LiMnO_2$ and layered $Li(Ni_{1/3}Mn_{1/3}Co_{1/3})O_2$. Between the electrodes, it has a proprietary specialized separator made of polyvinylidene fluoride (PVDF) that prevents short circuit and filled with a plasticized electrolyte (the proprietary electrolyte composing of organic carbonate). The cell was vacuumed out the gas generated in the initial cycle and sealed in the pouch which is composed of aluminum layers, polypropylene polymers, and nylon.

Nominal capacity of cells is 15 Ah. The cells were charged and discharged in 1C rate at room temperature. The typical charge and discharge protocol used in the following experiments is shown in Figure 4.14(b). A cell is charged at constant current 15 A up to 4.15 V, and then holds its voltage at 4.15 V until its current drops to 750 mA. After the cell is reaching 100% state of charge, let the cell rest for 1 hour before discharge it in constant current 15 A. A complete cycle is defined as one charge cycle, one discharge cycle, and two periods of resting (after charge cycle and discharge cycle). The gases generated after 2,655 cycles were composed of 40.1 ml CH_4, 4.4 ml C_2H_6, 2.8 ml N_2, 1.8 ml H_2, 1.4 ml CO, 0.6 ml CO_2, 0.4 ml O_2 and other small amounts of gases (i.e., C_2H_4, C_3H_8, and C_3H_6). Note that this test was made by GM R&D center and the cell was cycled without any prestressed pressure applied.
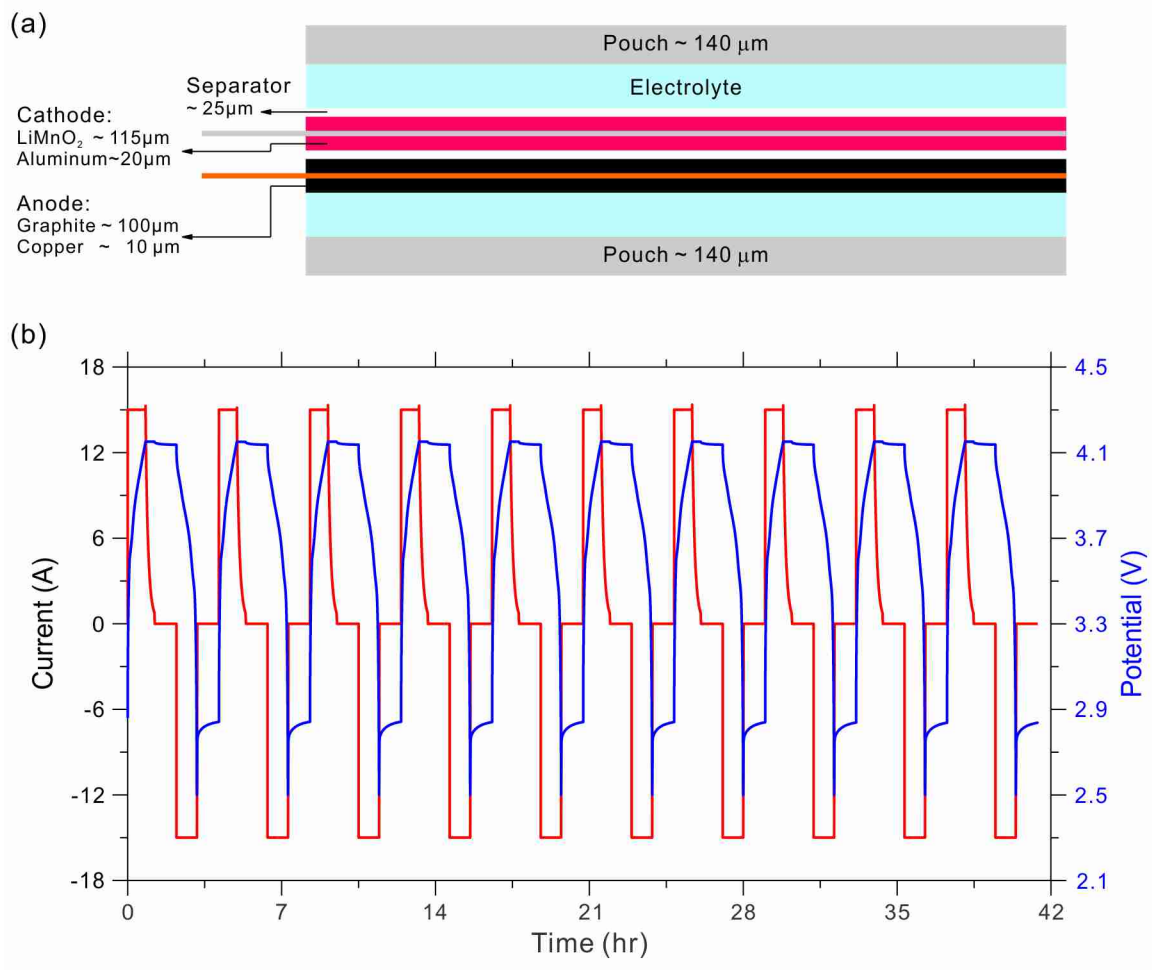
Figure 4.14 (a) A schematic of the dimensions and components of a LG 1.4 pouch Li-ion battery cell. One mini-cell composes of one anode, cathode, corresponding current collector sheets, and two separators. (b) The typical charge and discharge protocol used in the experiment for a LG pouch battery cell.

Appendix B: The Details of Finite Element Model

The flow chart of estimating the confinement pressure is delineated in Figure 4.15. Two

time-independent elastic constants, α and β, in equation (4.18), are first analyzed in

system B from ABAQUS via applying displacement $\bar{\delta}_{el}^{B}$ on the top surface. Then,
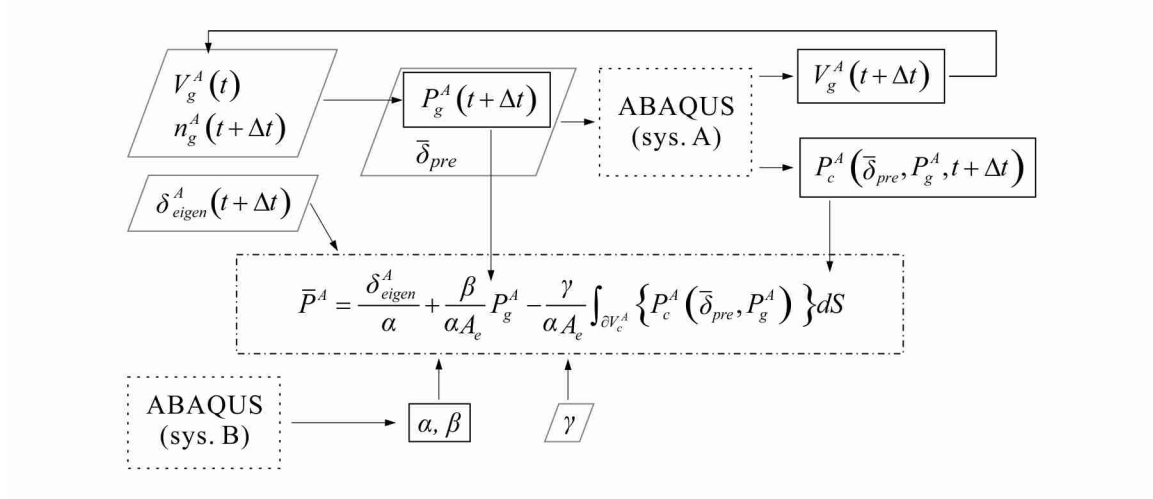
Figure 4.15 The flow chart of analyzing the confinement pressure at time $(t + \Delta t)$.

compute the cell pressure $\bar{P}^B$ and cavity volume ΔV_{cavity}^B, based on cell geometry and effective moduli. The third constant γ is a given relationship of penetration depth under contact pressure of a typical polymer, i.e., 6 MPa/μm for PMMA (Xia, 2008).

In system A, as shown in the flow chart Figure 4.15, the prestressed displacement $\bar{\delta}_{pre}$ and gas pressure P_g^A are input parameters to calculate the contact pressure P_c^A along the effective contact area. The model is first deformed from the original configuration due to initial prestressed displacement. Note that the initial prestressed displacement applied on the top of the surface $\bar{\delta}_{pre}$ is determined by measured strain multiplied by the thickness of the whole simulation model. The gas pressure is further applied to the inner surface of the cavity while the top surface of the model is fixed. Assume that the pressure generated in the battery cell is ideal gas. Therefore, the gas pressure can be determined from

$$P_g^A(t) = \frac{n_g^A(t) RT}{V_g^A(t)}, \tag{4.20}$$

where R is ideal gas constant, T temperature, V_g^A the volume to store the gas, and n_g^A the amount of the gas. For each time step, the deformed cavity volume V_g^A can be calculated via finite element analysis. The mole of the gas is estimated as linearly generated during the cycles, i.e.,

$$n_g^A(t) = n_0\, t, \tag{4.21}$$

in which n_0 is the coefficient representing the gas generation rate.

The eigen-displacement δ_{eigen}^A caused by lithium ion intercalation and deintercalation is determined by

$$\delta_{eigen}(t) = \delta_0 \times func\left(\frac{t}{\tau}\right), \tag{4.22}$$

where the function of eigen-displacement $func(t/\tau)$ is related to the state of charge (SOC) versus cycle and the coefficient δ_0 represents the amplitude of the eigen-displacement and the compliance characteristics of the pressure sensor.

Finally, combine the eigen-displacement δ_{eigen}^A, gas pressure P_g^A, contact pressure P_c^A along the effective contact area with three constants α, β, γ from system B. The average pressure (surface traction) $\bar{P}^A$ on the top of the surface can be computed. The gas generation rate is varied and determined through minimizing the error norm between the simulation results and the experimental data. Via this process, the amount of gas generated during the charge and discharge cycles can be estimated.

Chapter 5.

CONCLUSIONS AND FUTURE WORKS

5.1 Concluding Remarks

The multi-scale collective behavior characteristics of hierarchical interfaces in lithium-ion batteries (LIBs) during cycling has been measured via three different experiments and analyzed by simulation models. Two interfacial mechanisms were studied: one is interfacial sliding mechanism between the lithiated Si thin film electrode and the Cu current collector; the other is contact mechanism of internal interfaces in large format pouch cells. Significant efforts have been devoted towards performing delicate experiments and detail analyses to understand the cell behaviors. The major conclusions are summarized as follows.

In order to estimate the interfacial properties at a-SiLi$_x$//Cu interfaces during lithiation and delithiation cycles, a new apparatus, "Self-Adjusting Liquid Linnik Interferometer (SALLI)", has been invented. SALLI with naturally self-compensated ability can *in situ* measure the electrode deformation with 8 μm resolution in lateral direction and with 1 nm resolution in out-of-plane direction. These experimental results indicate the occurrence of the low friction due to Li segregation at the a-SiLi$_x$//Cu interface. Moreover, both lateral expansion of a Si electrode edge and the vertical

thickness variations were monitored during cycling. Our result clearly demonstrates Li segregation at the a-SiLi$_x$//Cu interface initially which leads to remarkable shrinkage (up to 200 μm in stage B) of the Si film in the first cycle. It appears to be driven by relaxation of residual tensile stress generated during the manufacturing process of the film. Then, the film starts to expand caused by massive bulk intercalation (stage C). This is followed by contraction of the film during delithiation (stage D). The latter two motions (stage C and D) are reversible in the following cycles.

A mechanical model system, plate bending distribution sensor (PBDS), which incorporates substrate bending and interfacial sliding in its calibration has been developed. By bridging the deformation estimated from the model and those measured from SALLI experiment, the interfacial properties between the electrode film and current collector were extracted quantitatively. Through this technique, the evolution of the zone size of interfacial sliding is detected and the critical energy release rate is estimated as 0.075 J/m^2 for a receding shear crack front and 0.34 J/m^2 for a growing shear crack front at the edge of the sliding zone. Note that the latter depends on the phase of the loading and the state of intercalation. These measurements show that the concentrated shear strength is 59.9 – 64.0 MPa during lithiation cycles, and 29.9 – 30.5 MPa during delithiation processes. A remarkable discovery is that the sliding resistance of the actively segregating lithium between a-SiLi$_x$//Cu interface is measured only 1.15 kPa. It is ten thousand times smaller than the flow stress of an inactive Li segregation layer estimated by DFT calculation (Stournara *et al.*, 2013). This is believed to be due to electro-chemically active lithium-ion segregation process that allows slip processes of hopping through a series of meta-stable atomic configurations. Similar lubrication

phenomena with flow stresses of the same order have been observed in charged polymers (Raviv *et al.*, 2003) and an ionic-liquid layered confined between mica surfaces (Perkin *et al.*, 2010).

Two sets of *in situ* experimental tests have been performed and a mechanical model has been developed to explain the internal contact mechanism and its relationship with interface bubble-gas evolution. Through these experiments and the model, the degradation mechanisms of the large format pouch cells are elaborated. Thickness variation of a free standing LG Li-ion battery cell was first measured by ESPI. The local deformation across the cell surface is non-uniform and temporally non-monotonic. Hence, it is insufficient to use an average thickness to represent characteristics of the volume changes for the large format pouch cells used in PHEV. Peculiar fast motions of swell-shrink polarization in thickness variations have been observed during a series of C-D cycles. It has shown that this deformation is caused by gas generation and migration inside the cell.

Second, *in situ* confinement-pressure variations across the whole surface area of constrained battery cells were performed using a high resolution pressure sensor pad. The pressure variations are composed of two distinct characteristics: one is coherent with the C-D cycles and the other is gradually increasing regime. The former reversible feature is considered to be attributed to the electrode deformations due to insertion and removal of Li. The latter characteristic indicates that the existing or new forming gas inside the surface is trapped by the rising contact area.

An integrated mechanical-electrochemical model has been develop to capture both SOC dependence and gas evolution-induced cell pressure for the new and aged cells.

The result indicates that the gas plays an important role in the battery mechanism. It has shown that applying mechanical constraints (cell compression) can impact battery performance and life. Maintaining a compressive force on the electrodes can provide a uniform contact of all components and prevent the delamination of the active material from the current collector.

It is hoped that the work carried out in this thesis can contribute to the optimal design of new battery technology and maximize the Li capacity and cycle life of LIBs.

5.2   Future Works

It is believe that electro-chemically active lithium-ion segregation process causes the remarkably low interfacial shear strength (ISS) measured in this thesis. The intrinsic voids or grain boundaries in the Cu current collector provide short tunnels to let lithium-ions transfer easily and rapidly to the interface. This tunneling effect causes the interface wetting at the early stage (i.e., stage B in the experiment) in the first cycle and induces interfacial sliding easily. To further understand the electro-chemically active process, several approaches can be considered in the future.

In experimental aspects, control deposition rates and conditions to study the influence of the density and distribution of voids or grain boundaries in the Cu. Cutting samples via focused ion beam (FIB) and imaging their interfaces through TEM at different lithiation stages can provide useful information of the interface wetting phenomena. Besides, the time-of-flight secondary ion mass spectrometer (TOF-SIMS) measurement can provide the depth profiles for Li/Si ratio and Cu^+ ions at the interface. On simulation sides, a layer or few layers of charged ions should be included in future

DFT calculations to further understand the slip processes of hopping through a series of meta-stable atomic configurations. A more detailed viscoelastic shear resistance model should be considered, since currently ISS is sliding rate and time dependent. Moreover, the ISS in the region (few μm) close to the slip front can be much higher than that far away from the slip front. Therefore, the model should also be spatial dependent.

The current micromechanical internal state model can be used as a unit constitutive model to analyze bubble-gas migration/leakage in the battery and its effects on micro-cracking and degradation of electrodes. The local pressure can be simulated by adding the spatial variables into the model. By this way, the stress variations over the whole surface of the battery can be properly calculated. This model can be expended as a constitutive equation to bridge understandings in PHEV Li-ion battery performances under different constrained pressure.

REFERENCES

Ali, M. Y., Lai, W.-J., & Pan, J. (2013). Computational Models for Simulations of Lithium-Ion Battery Cells under Constrained Compression Tests. *J. Power Sources,* **242**(0), 325-340.

Argon, A. S., Gupta, V., Landis, H. S., & Cornie, J. A. (1989). Intrinsic Toughness of Interfaces between SiC Coatings and Substrates of Si or C Fibre. *J Mater Sci,* **24**(4), 1207-1218.

Arora, P., Doyle, M., & White, R. E. (1999). Mathematical Modeling of the Lithium Deposition Overcharge Reaction in Lithium-Ion Batteries Using Carbon-Based Negative Electrodes. *J. Electrochem. Soc.,* **146**(10), 3543-3553.

Arora, P., & Zhang, Z. (2004). Battery Separators. *Chem. Rev.,* **104**(10), 4419-4462.

Aurbach, D. (2000). Review of Selected Electrode–Solution Interactions which Determine the Performance of Li and Li Ion Batteries. *J. Power Sources,* **89**(2), 206-218.

Aurbach, D., Chusid, O., Weissman, I., & Dan, P. (1996). $LiC(SO_2CF_3)_3$, a New Salt for Li Battery Systems. A Comparative Study of Li and Non-Active Metal Electrodes in Its Ethereal Solutions Using In Situ FTIR Spectroscopy. *Electrochim. Acta,* **41**(5), 747-760.

Aurbach, D., & Cohen, Y. (1996). The Application of Atomic Force Microscopy for the Study of Li Deposition Processes. *J. Electrochem. Soc.,* **143**(11), 3525-3532.

Balasubramanian, M., Sun, X., Yang, X. Q., & Mcbreen, J. (2001). In Situ X-Ray Diffraction and X-Ray Absorption Studies of High-Rate Lithium-Ion Batteries. *J. Power Sources,* **92**(1–2), 1-8.

Balken, Jesses, Morozovska, A. N., Eliseeve, Chung, D. W., Kimy, et al. (2010). Nanoscale Mapping of Ion Diffusion in a Lithium-Ion Battery Cathode. *Nature Nanotechnology,* **5**(10), 749-754.

Basu, S. (1981). Rechargeable Battery: Google Patents.

Beaulieu, L. Y., Eberman, K. W., Turner, R. L., Krause, L. J., & Dahn, J. R. (2001). Colossal Reversible Volume Changes in Lithium Alloys. *Electrochem. Solid-State Lett.,* **4**(9), A137-A140.

Becker, C. R., Strawhecker, K. E., Mcallister, Q. P., & Lundgren, C. A. (2013). In Situ Atomic Force Microscopy of Lithiation and Delithiation of Silicon Nanostructures for Lithium Ion Batteries. *ACS Nano*.

Boukamp, B. A., Lesh, G. C., & Huggins, R. A. (1981). All-Solid Lithium Electrodes with Mixed-Conductor Matrix. *J. Electrochem. Soc.,* **128**(4), 725-729.

Bourderau, S., Brousse, T., & Schleich, D. M. (1999). Amorphous Silicon as a Possible Anode Material for Li-Ion Batteries. *J. Power Sources,* **81–82**(0), 233-236.

Broussely, M., Biensan, P., Bonhomme, F., Blanchard, P., Herreyre, S., Nechev, K., et al. (2005). Main Aging Mechanisms in Li Ion Batteries. *J. Power Sources,* **146**(1–2), 90-96.

Bruce, P. G., Scrosati, B., & Tarascon, J.-M. (2008). Nanomaterials for Rechargeable Lithium Batteries. *Angew. Chem. Int. Ed.,* **47**(16), 2930-2946.

Burt, D. P., Wilson, N. R., Janus, U., Macpherson, J. V., & Unwin, P. R. (2008). In-Situ Atomic Force Microscopy (AFM) Imaging: Influence of AFM Probe Geometry on Diffusion to Microscopic Surfaces. *Langmuir,* **24**(22), 12867-12876.

Chan, C. K., Peng, H., Liu, G., Mcilwrath, K., Zhang, X. F., Huggins, R. A., et al. (2008). High-Performance Lithium Battery Anodes Using Silicon Nanowires. *Nature Nanotechnology,* **3**(1), 31-35.

Chan, C. K., Ruffo, R., Hong, S. S., Huggins, R. A., & Cui, Y. (2009). Structural and Electrochemical Study of the Reaction of Lithium with Silicon Nanowires. *J. Power Sources,* **189**(1), 34-39.

Chen, D., Indris, S., Schulz, M., Gamer, B., & Mönig, R. (2011). In Situ Scanning Electron Microscopy on Lithium-Ion Battery Electrodes Using an Ionic Liquid. *J. Power Sources,* **196**(15), 6382-6387.

Dahn, J. R. (1991). Phase diagram of Li_xC_6. *Physical Review B,* **44**(17), 9170-9177.

Dedryvère, R., Gireaud, L., Grugeon, S., Laruelle, S., Tarascon, J. M., & Gonbeau, D. (2005). Characterization of Lithium Alkyl Carbonates by X-ray Photoelectron Spectroscopy: Experimental and Theoretical Study. *J. Phys. Chem. B,* **109**(33), 15868-15875.

Domi, Y., Ochida, M., Tsubouchi, S., Nakagawa, H., Yamanaka, T., Doi, T., et al. (2011). In Situ AFM Study of Surface Film Formation on the Edge Plane of HOPG for Lithium-Ion Batteries. *Journal of Physical Chemistry C,* **115**(51), 25484-25489.

Dubois, A., & Boccara, A. C. (2008). USA Patent No.

Etacheri, V., Marom, R., Elazari, R., Salitra, G., & Aurbach, D. (2011). Challenges in the Development of Advanced Li-Ion Batteries: a Review. *Energy Environ. Sci.,* **4**(9), 3243-3262.

Freund, L. B., & Suresh, S. (2003). *Thin Film Materials: Stress, Defect Formation and Surface Evolution*: Cambridge University Press.

Gille, G., & Rau, B. (1984). Buckling Instability and Adhesion of Carbon Layers. *Thin Solid Films,* **120**(2), 109-121.

Goers, D., Holzapfel, M., Scheifele, W., Lehmann, E., Vontobel, P., & Novák, P. (2004). In Situ Neutron Radiography of Lithium-Ion Batteries: The Gas Evolution on Graphite Electrodes during the Charging. *J. Power Sources,* **130**(1–2), 221-226.

Gomadam, P. M., Weidner, J. W., Dougal, R. A., & White, R. E. (2002). Mathematical Modeling of Lithium-Ion and Nickel Battery Systems. *J. Power Sources,* **110**(2), 267-284.

Graetz, J., Ahn, C. C., Yazami, R., & Fultz, B. (2003). Highly Reversible Lithium Storage in Nanostructured Silicon. *Electrochem. Solid-State Lett.,* **6**(9), A194-A197.

Guo, Z. P., Milin, E., Wang, J. Z., Chen, J., & Liu, H. K. (2005). Silicon/Disordered Carbon Nanocomposites for Lithium-Ion Battery Anodes. *J. Electrochem. Soc.,* **152**(11), A2211-A2216.

Haftbaradaran, H., & Gao, H. (2012). Ratcheting of Silicon Island Electrodes on Substrate due to Cyclic Intercalation. *Appl. Phys. Lett.,* **100**(12), 121907-121904.

Haftbaradaran, H., Xiao, X., Gao, H., Soni, S. K., & Sheldon, B. W. (2012). Modified Stoney Equation for Patterned Thin Film Electrodes on Substrates in the Presence of Interfacial Sliding. *J. Appl. Mech.,* **79**(3), 031018-031018.

Huang, J. Y., Zhong, L., Wang, C. M., Sullivan, J. P., Xu, W., Zhang, L. Q., et al. (2010). In Situ Observation of the Electrochemical Lithiation of a Single SnO_2 Nanowire Electrode. *Science,* **330**(6010), 1515-1520.

Jeong, S.-K., Inaba, M., Abe, T., & Ogumi, Z. (2001). Surface Film Formation on Graphite Negative Electrode in Lithium-Ion Batteries: AFM Study in an Ethylene Carbonate-Based Solution. *J. Electrochem. Soc.,* **148**(9), A989-A993.

Ji, L., Lin, Z., Alcoutlabi, M., & Zhang, X. (2011). Recent Developments in Nanostructured Anode Materials for Rechargeable Lithium-Ion Batteries. *Energy Environ. Sci.,* **4**(8), 2682-2699.

Kasavajjula, U., Wang, C., & Appleby, A. J. (2007). Nano- and Bulk-Silicon-Based Insertion Anodes for Lithium-Ion Secondary Cells. *J. Power Sources,* **163**(2), 1003-1039.

Kim, S.-P., Duin, A. C. T. V., & Shenoy, V. B. (2011). Effect of Electrolytes on the Structure and Evolution of the Solid Electrolyte Interphase (SEI) in Li-Ion Batteries: A Molecular Dynamics Study. *J. Power Sources,* **196**(20), 8590-8597.

Kostecki, R., Lei, J., Mclarnon, F., Shim, J., & Striebel, K. (2006). Diagnostic Evaluation of Detrimental Phenomena in High-Power Lithium-Ion Batteries. *J. Electrochem. Soc.,* **153**(4), A669-A672.

Lai, W.-J., Ali, M. Y., & Pan, J. (2014). Mechanical Behavior of Representative Volume Elements of Lithium-Ion Battery Cells under Compressive Loading Conditions. *J. Power Sources,* **245**(0), 609-623.

Lee, J. H., Lee, H. M., & Ahn, S. (2003). Battery Dimensional Changes Occurring during Charge/Discharge Cycles—Thin Rectangular Lithium Ion and Polymer Cells. *J. Power Sources,* **119–121**(0), 833-837.

Lehmann, P. (2010). Vertical Scanning White-Light Interference Microscopy on Curved Microstructures. *Opt. Lett.,* **35**(11), 1768-1770.

Linnik, W. P. (1933). Ein Apparat Für Mikroskopisch-Interferometrische Untersuchungen Reflektierender Objekte (Mikrointerferometer). *C. R. Dokl. Acad. Sci. Urss,* **1**.

Liu, X. H., & Huang, J. Y. (2011). In Situ TEM Electrochemistry of Anode Materials in Lithium Ion Batteries. *Energy Environ. Sci.,* **4**(10), 3844-3860.

Liu, X. H., Zheng, H., Zhong, L., Huang, S., Karki, K., Zhang, L. Q., et al. (2011). Anisotropic Swelling and Fracture of Silicon Nanowires during Lithiation. *Nano Lett.,* **11**(8), 3312-3318.

Liu, X. H., Zhong, L., Huang, S., Mao, S. X., Zhu, T., & Huang, J. Y. (2012). Size-Dependent Fracture of Silicon Nanoparticles During Lithiation. *ACS Nano,* **6**(2), 1522-1531.

Lyulko, O. V., Randers-Pehrson, G., & Brenner, D. J. (2010). *Immersion Mirau Interferometry for Label-Free Live Cell Imaging in an Epi-Illumination Geometry.* Paper presented at the Proc. SPIE

Magasinski, A., Dixon, P., Hertzberg, B., Kvit, A., Ayala, J., & Yushin, G. (2010). High-Performance Lithium-Ion Anodes Using a Hierarchical Bottom-Up Approach. *Nature Material,* **9**(4), 353-358.

Malacara, D. (2007). *Optical Shop Testing*: Wiley.

Maranchi, J. P., Hepp, A. F., Evans, A. G., Nuhfer, N. T., & Kumta, P. N. (2006). Interfacial Properties of the a-Si ／ Cu :Active–Inactive Thin-Film Anode System for Lithium-Ion Batteries. *J. Electrochem. Soc.,* **153**(6), A1246-A1253.

Maranchi, J. P., Hepp, A. F., & Kumta, P. N. (2003). High Capacity, Reversible Silicon Thin-Film Anodes for Lithium-Ion Batteries. *Electrochem. Solid-State Lett.,* **6**(9), A198-A201.

Mcarthur, M. A., Trussler, S., & Dahn, J. R. (2012). In Situ Investigations of SEI Layer Growth on Electrode Materials for Lithium-Ion Batteries Using Spectroscopic Ellipsometry. *J. Electrochem. Soc.,* **159**(3), A198-A207.

Mcdowell, M. T., Lee, S. W., Harris, J. T., Korgel, B. A., Wang, C., Nix, W. D., et al. (2013). In Situ TEM of Two-Phase Lithiation of Amorphous Silicon Nanospheres. *Nano Lett.,* **13**(2), 758-764.

Michelson, A. A., & Morley, E. W. (1887). On the Relative Motion of the Earth and the Luminiferous Ether. *Am. J. Sci.,* **Series 3 Vol. 34**(203), 333-345.

Mirau, A. H. (1952).

Nagaura, T., & Tozawa, K. (1990). Lithium Ion Rechargeable Battery. *Prog. Batteries Solar Cells,* **9**, 209.

Niehues, J., Lehmann, P., & Xie, W. (2012). Low Coherent Linnik Interferometer Optimized for Use in Nano-Measuring Machines. *Meas. Sci. Technol.,* **23**(12), 125002.

Novák, P., Panitz, J. C., Joho, F., Lanz, M., Imhof, R., & Coluccia, M. (2000). Advanced In Situ Methods for the Characterization of Practical Electrodes in Lithium-Ion Batteries. *J. Power Sources,* **90**(1), 52-58.

Obrovac, M. N., & Christensen, L. (2004). Structural Changes in Silicon Anodes during Lithium Insertion/Extraction. *Electrochem. Solid-State Lett.,* **7**(5), A93-A96.

Ohara, S., Suzuki, J., Sekine, K., & Takamura, T. (2004). A Thin Film Silicon Anode for Li-Ion Batteries Having a Very Large Specific Capacity and Long Cycle Life. *J. Power Sources,* **136**(2), 303-306.

Orsini, F., Du Pasquier, A., Beaudoin, B., Tarascon, J. M., Trentin, M., Langenhuizen, N., et al. (1998). In Situ Scanning Electron Microscopy (SEM) Observation of Interfaces within Plastic Lithium Batteries. *J. Power Sources,* **76**(1), 19-29.

Peabody, C., & Arnold, C. B. (2011). The Role of Mechanically Induced Separator Creep in Lithium-Ion Battery Capacity Fade. *J. Power Sources,* **196**(19), 8147-8153.

Perkin, S., Albrecht, T., & Klein, J. (2010). Layering and Shear Properties of an Ionic Liquid, 1-Ethyl-3-Methylimidazolium Ethylsulfate, Confined to Nano-Films between Mica Surfaces. *PCCP,* **12**(6), 1243-1247.

Poizot, P., Laruelle, S., Grugeon, S., Dupont, L., & Tarascon, J. M. (2000). Nano-Sized Transition-Metal Oxides as Negative-Electrode Materials for Lithium-Ion Batteries. *Nature,* **407**(6803), 496-499.

Ponnappan, R., & Ravigururajan, T. S. (2004). Contact Thermal Resistance of Li-Ion Cell Electrode Stack. *J. Power Sources,* **129**(1), 7-13.

Raviv, U., Giasson, S., Kampf, N., Gohy, J.-F., Jerome, R., & Klein, J. (2003). Lubrication by Charged Polymers. *Nature,* **425**(6954), 163-165.

Reed, J., Troke, J. J., Schmit, J., Han, S., Teitell, M. A., & Gimzewski, J. K. (2008). Live Cell Interferometry Reveals Cellular Dynamism During Force Propagation. *ACS Nano,* **2**(5), 841-846.

Rubino, R. S., Gan, H., & Takeuchi, E. S. (2001). A Study of Capacity Fade in Cylindrical and Prismatic Lithium-Ion Batteries. *J. Electrochem. Soc.,* **148**(9), A1029-A1033.

Ryu, I., Choi, J. W., Cui, Y., & Nix, W. D. (2011). Size-Dependent Fracture of Si Nanowire Battery Anodes. *Journal of the Mechanics and Physics of Solids,* **59**(9), 1717-1730.

Sahraei, E., Campbell, J., & Wierzbicki, T. (2012). Modeling and Short Circuit Detection of 18650 Li-Ion Cells under Mechanical Abuse Conditions. *J. Power Sources,* **220**(0), 360-372.

Sahraei, E., Meier, J., & Wierzbicki, T. (2014). Characterizing and Modeling Mechanical Properties and Onset of Short Circuit for Three Types of Lithium-Ion Pouch Cells. *J. Power Sources,* **247**(0), 503-516.

Schalkwijk, W., & Scrosati, B. (2002). Advances in Lithium Ion Batteries Introduction. In W. Schalkwijk & B. Scrosati (Eds.), *Advances in Lithium-Ion Batteries* (pp. 1-5): Springer US.

Schwider, J. (1999). *Partially Coherent Illumination in Interferometry for Optical Testing*.

Seong Kim, U., Yi, J., Shin, C. B., Han, T., & Park, S. (2011). Modeling the Dependence of the Discharge Behavior of a Lithium-Ion Battery on the Environmental Temperature. *J. Electrochem. Soc.,* **158**(5), A611-A618.

Sethuraman, V. A., Chon, M. J., Shimshak, M., Srinivasan, V., & Guduru, P. R. (2010a). In Situ Measurements of Stress Evolution in Silicon Thin Films during Electrochemical Lithiation and Delithiation. *J. Power Sources,* **195**(15), 5062-5066.

Sethuraman, V. A., Srinivasan, V., Bower, A. F., & Guduru, P. R. (2010b). In Situ Measurements of Stress-Potential Coupling in Lithiated Silicon. *J. Electrochem. Soc.,* **157**(11), A1253-A1261.

Shenoy, V. B., Johari, P., & Qi, Y. (2010). Elastic Softening of Amorphous and Crystalline Li–Si Phases with Increasing Li Concentration: A First-Principles Study. *J. Power Sources,* **195**(19), 6825-6830.

Shi, S., Lu, P., Liu, Z., Qi, Y., Hector, L. G., Li, H., et al. (2012). Direct Calculation of Li-Ion Transport in the Solid Electrolyte Interphase. *J. Am. Chem. Soc.,* **134**(37), 15476-15487.

Siegel, J. B., Stefanopoulou, A. G., Hagans, P., Ding, Y., & Gorsich, D. (2013). Expansion of Lithium Ion Pouch Cell Batteries: Observations from Neutron Imaging. *J. Electrochem. Soc.,* **160**(8), A1031-A1038.

Soni, S. K., Sheldon, B. W., Xiao, X., Verbrugge, M. W., Dongjoon, A., H., H., et al. (2011). Stress Mitigation during the Lithiation of Patterned Amorphous Si Islands. *J. Electrochem. Soc.,* **159**(1), A38-A43.

Sri Devi Kumari, T., Jeyakumar, D., & Prem Kumar, T. (2013). Nano Silicon Carbide: A New Lithium-Insertion Anode Material on the Horizon. *RSC Advances,* **3**(35), 15028-15034.

Steele, B. C. H., & Armand, M. B. (1973). *Fast Ion Transport in Solids: Solid State Batteries and Devices*. North Holland Pub. Co.: Amsterdam.

Stournara, M. E., Xiao, X., Qi, Y., Johari, P., Lu, P., Sheldon, B. W., et al. (2013). Li Segregation Induces Structure and Strength Changes at the Amorphous Si/Cu Interface. *Nano Lett.,* **13**(10), 4759-4768.

Sun, C.-F., Karki, K., Jia, Z., Liao, H., Zhang, Y., Li, T., et al. (2013). A Beaded-String Silicon Anode. *ACS Nano,* **7**(3), 2717-2724.

Takami, N., Satoh, A., Hara, M., & Ohsaki, T. (1995). Structural and Kinetic Characterization of Lithium Intercalation into Carbon Anodes for Secondary Lithium Batteries. *J. Electrochem. Soc.,* **142**(2), 371-379.

Takamura, T., Ohara, S., Uehara, M., Suzuki, J., & Sekine, K. (2004). A Thin Film Silicon Anode for Li-Ion Batteries Having a Very Large Specific Capacity and Long Cycle Life. *J. Power Sources,* **129**(1), 96-100.

Tarascon, J. M., & Armand, M. (2001). Issues and Challenges Facing Rechargeable Lithium Batteries. *Nature,* **414**(6861), 359-367.

Thackeray, M. M., David, W. I. F., Bruce, P. G., & Goodenough, J. B. (1983). Lithium Insertion into Manganese Spinels. *Mater. Res. Bull.,* **18**(4), 461-472.

Tokranov, A., Sheldon, B. W., Li, C., Minne, S., & Xiao, X. (2014). In Situ Atomic Force Microscopy Study of Initial Solid Electrolyte Interphase Formation on Silicon Electrodes for Li-Ion Batteries. *ACS Applied Materials & Interfaces.*

Verma, P., Maire, P., & Novák, P. (2010). A Review of the Features and Analyses of the Solid Electrolyte Interphase in Li-Ion Batteries. *Electrochim. Acta,* **55**(22), 6332-6341.

Vetter, J., Novák, P., Wagner, M. R., Veit, C., Möller, K. C., Besenhard, J. O., et al. (2005). Ageing Mechanisms in Lithium-Ion Batteries. *J. Power Sources,* **147**(1–2), 269-281.

Wakihara, M. (2001). Recent Developments in Lithium Ion Batteries. *Mater. Sci. Eng., R,* **33**(4), 109-134.

Wang, J. W., He, Y., Fan, F., Liu, X. H., Xia, S., Liu, Y., et al. (2013). Two-Phase Electrochemical Lithiation in Amorphous Silicon. *Nano Lett.,* **13**(2), 709-715.

Wang, J. W., Liu, X. H., Zhao, K., Palmer, A., Patten, E., Burton, D., et al. (2012). Sandwich-Lithiation and Longitudinal Crack in Amorphous Silicon Coated on Carbon Nanofibers. *ACS Nano,* **6**(10), 9158-9167.

Wang, X., Sone, Y., Segami, G., Naito, H., Yamada, C., & Kibe, K. (2007). Understanding Volume Change in Lithium-Ion Cells during Charging and Discharging Using In Situ Measurements. *J. Electrochem. Soc.,* **154**(1), A14-A21.

Whittingham, M. S. (1976). Electrical Energy Storage and Intercalation Chemistry. *Science,* **192**(4244), 1126-1127.

Whittingham, M. S. (2004). Lithium Batteries and Cathode Materials. *Chem. Rev.,* **104**(10), 4271-4302.

Xia, S. (2008). *Micromechanics of Solid-Surface Contact Suspension and Its Role in Friction.* Brown University.

Xiao, X., Liu, P., Verbrugge, M. W., Haftbaradaran, H., & Gao, H. (2011). Improved Cycling Stability of Silicon Thin Film Electrodes Through Patterning for High Energy Density Lithium Batteries. *J. Power Sources,* **196**(3), 1409-1416.

Xu, S., Zhang, Y., Cho, J., Lee, J., Huang, X., Jia, L., et al. (2013). Stretchable Batteries with Self-Similar Serpentine Interconnects and Integrated Wireless Recharging Systems. *Nature Communication,* **4**, 1543.

Yao, Y., Mcdowell, M. T., Ryu, I., Wu, H., Liu, N., Hu, L., et al. (2011). Interconnected Silicon Hollow Nanospheres for Lithium-Ion Battery Anodes with Long Cycle Life. *Nano Lett.,* **11**(7), 2949-2954.

Yi, J., Kim, U. S., Shin, C. B., Han, T., & Park, S. (2013). Modeling the Temperature Dependence of the Discharge Behavior of a Lithium-Ion Battery in Low Environmental Temperature. *J. Power Sources,* **244**(0), 143-148.

Yu, H. H., He, M. Y., & Hutchinson, J. W. (2001). Edge Effects in Thin Film Delamination. *Acta Mater.,* **49**(1), 93-107.

Zaghib, K., Brochu, F., Guerfi, A., & Kinoshita, K. (2001). Effect of Particle Size on Lithium Intercalation Rates in Natural Graphite. *J. Power Sources,* **103**(1), 140-146.

Zhang, L. Q., Liu, X. H., Liu, Y., Huang, S., Zhu, T., Gui, L., et al. (2011). Controlling the Lithiation-Induced Strain and Charging Rate in Nanowire Electrodes by Coating. *ACS Nano,* **5**(6), 4800-4809.

Zhang, W.-J. (2011). A Review of the Electrochemical Performance of Alloy Anodes for Lithium-Ion Batteries. *J. Power Sources,* **196**(1), 13-24.

Zheng, H., Jiang, K., Abe, T., & Ogumi, Z. (2006). Electrochemical Intercalation of Lithium into a Natural Graphite Anode in Quaternary Ammonium-Based Ionic Liquid Electrolytes. *Carbon,* **44**(2), 203-210.